Development and Implementation of In-line Characterization Methods for Roll-to-Roll Production of Thin-Film Solar Modules

Shantiswaroop Mishra

MSc Sustainable Energy Technology

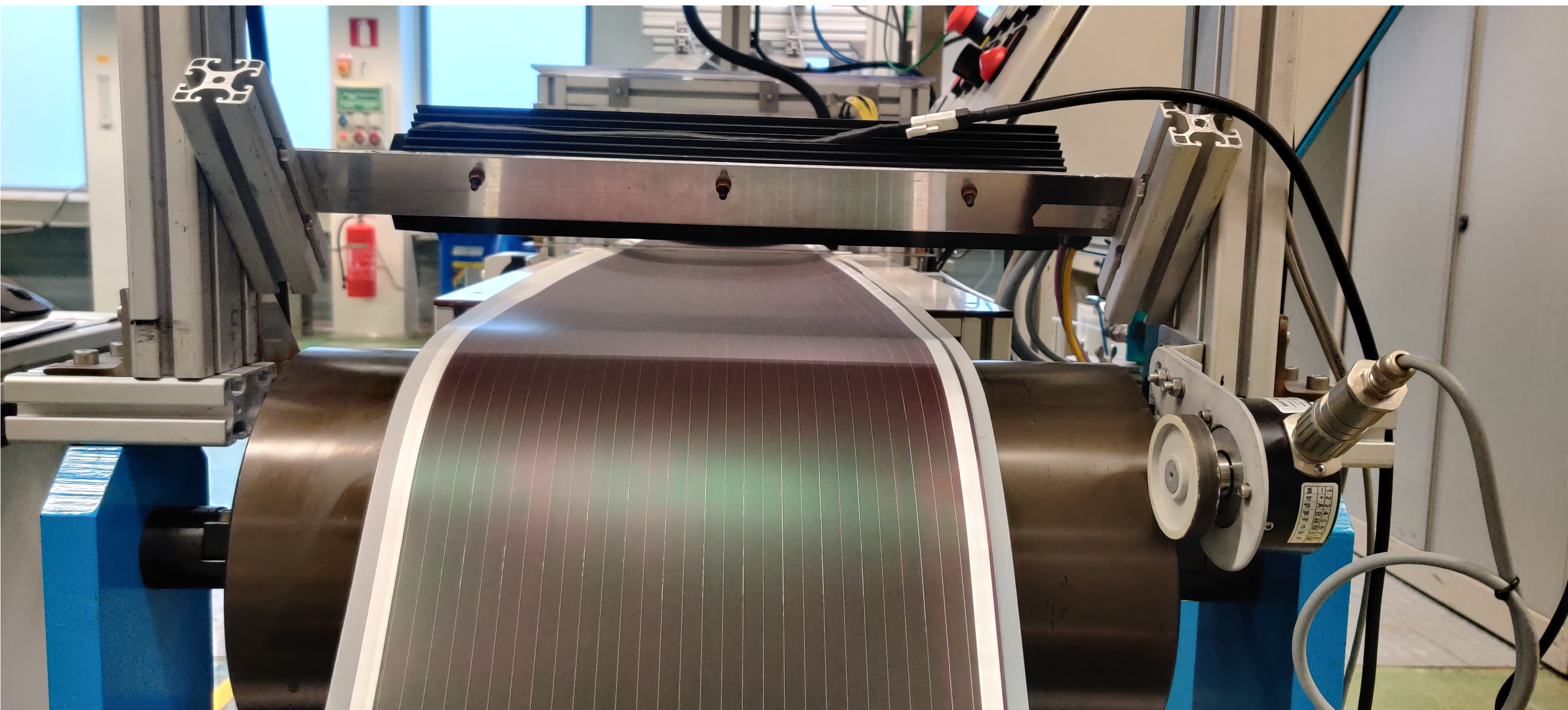

TU Delft

Development and Implementation of In-line Characterization Methods for Roll-to-Roll Production of Thin-Film Solar Modules

by

Shantiswaroop Mishra

to obtain the degree of Master of Science
at Delft University of Technology,
to be defended publicly on Wednesday July 19, 2023 at 09:00 AM.

Student number:	5280095	
Project duration:	November 1, 2022 – July 19, 2023	
Thesis committee:	Prof. dr. ir. A.H.M. Smets,	TU Delft, supervisor
	Dr. ir. M. Vogt,	Assistant Professor, TU Delft
	Ir. A. Ranneh,	Supervisor, HyET Solar B.V.
	Dr. P. P. Rodriguez,	TU Delft, Co-supervisor
	Dr. A. Lekic,	Assistant Professor, SMIEEE TU Delft

This thesis is confidential and cannot be made public until July 11, 2025.

An electronic version of this thesis is available at `http://repository.tudelft.nl/`.

TU Delft

Preface

Dear Reader,

This report is written to present the research carried out at HyET Solar, as a part of my masters' thesis. For the purpose of this study, I developed a model to extract important electrical parameters of a layer in solar cell and calibrate a novel device fabricated at HyET. The completion of this report marks the end of my incredible Masters' journey with the Delft University of Technology and HyET Solar.

While writing the report I assumed the reader to have sufficient knowledge of thin-film solar cell technology and basic electrical engineering. A basic introduction to the thin-film solar module production process at HyET is provided to help understand the overview of this technology.

Readers that are particularly interested in learning the model developed and implemented to characterize one layer of a cell, with the help of a light source, will find these in Chapter 3. Readers who are more interested in understanding the electrical sheet resistance measurement done on an aluminum substrate can go through Chapter 4. Lastly, readers who are more inclined towards the electrical and control engineering side, can find it in Chapter 5.

Shantiswaroop Mishra
Delft, 19 July 2023

Acknowledgements

First and foremost, I would like to thank Lord Shree Jagannath for bestowing me with everything I have possessed and achieved so far. I would also like to thank my late grandfather whose profound love and valuable teachings made me what I am today.

I extend my warm regards to Rahul Papriwal, without his guidance and support I would not have made it so far away from my family and country. He has always been present to help me, guide me and correct me during the entire duration of my thesis at HyET Solar. I would like to thank Professor Arno Smets and Gianluca Limodio for providing me with an opportunity to do my thesis at HyET. It was one of the most interesting and learning experiences I have ever had until now.

A big thank you and my heartfelt respect to Dr. Edward Hamers, the Chief Technology Officer of HyET Solar. Despite his very very busy schedule in a day, he always was there for me to resolve my doubts and at the same time teach me valuable life lessons. I re-found my hidden interest in physics and mathematics only because of you. Thank you for being there to catch me when I failed multiple times during my thesis.

My special thanks to Amr Ranneh, who tolerated my ”phone calls at any given time” thing. We have bonded over resolving the tantrums of the APCVD machine diagnostics. Mohammed El Makkaoui and Jimmy Melskens, thank you for sharing your in-depth knowledge on solar cell technology and guiding me at every step of my thesis. My special thank you to Paula Perez Rodriguez, for providing me with valuable comments and feedback to enhance the quality of my report.

My friends in Delft, Ankush, Arav, Devansh, Gaurav, Janki, Kishan, Pratyush, Ritik and Shloka. You all have been my light in dark times. The parties, trips and the ranting sessions with you have been the fuel to the completion of my thesis. Thank you guys for existing and tolerating me (almost) every weekend at your place. A heartfelt thank you to the best group one can ever ask for, ”SET Karenge Milke”. Devansh, Gaurav and Shloka, I can never forget the group ”life” discussions and random Foosball plans with you guys. My so to say, elder brother, Utkarsh, who has made my life here at Arnhem bearable and so fun.

To end with my most loved and important persons in my life, my parents, my little brother, and my girlfriend, Omisha. Nothing would have been even nearly possible without you guys in my life. Those positive pushes from Omisha when my models and methods failed saying ”How can your model be a failure?” has motivated me so much more than, an ”It’s okay”. Mom and Dad, thank you so much for forgetting your pain and loneliness back home and standing like a pillar with me each and every time. My little brother, who has been my best friend more than a brother, thank you for listening to my worries and pacifying me.

Summary

The ever rising utilisation of fossil fuels as the dominant energy source has led to heightened carbon dioxide emissions around the world. Consequently, there are serious negative implications on the living organisms in the planet, besides depletion and shortage of fossil fuels globally. Therefore, an urgency arises to harness the power from alternative renewable energy sources. Among natural resources such as wind, hydro, nuclear, solar energy has an enormous potential, as the Sun emits adequate amounts of energy, per second, to satisfy the energy demand of entire human race for over two hours. The rising awareness of the society has led to a rapid growth in the generation of solar energy which stands currently at 1040 Terra-Watt hours. Photovoltaic panels are one of the commonly employed technologies to convert this energy into electricity. HyET Solar, in Arnhem, is one of the firms that produces flexible, lightweight and low cost photovoltaic modules, based on the thin-film technology, in a roll-to-roll production process.

This report aims to establish the importance of having quality control methods in and on the production machines for assessing the quality of material deposited. There are a total of seven main processes at HyET, among which the project focuses on the two most important steps. First, the front transparent conductive oxide (TCO) layer deposition and second, the deposition of silicon layers. The research study involved developing and implementing models to characterize the deposited TCO, for its quality and calibrating a novel device to assess the quality of the deposited silicon layers.

To fully characterize the deposited TCO layer in terms of its quality, three important parameters need to be determined. These include layer thickness, free carrier concentration, and their mobility inside the layer. Among these parameters, the current in-line diagnostics at HyET had the capability of obtaining only the layer thickness; while to obtain information on the latter two properties, samples were sent to a third party. This increased the learning cycles and feedback rates to qualify the deposited layer. This motivated to develop a model that could extract the electrical parameters in-line, optically. Two models were subsequently proposed, first, an empirical approach was put forth, and second, a model based on Drude model was proposed. The latter was chosen to be implemented in-line, owing to its simplicity and ease of integration with the software.

Additionally, there exists another crucial parameter known as the sheet resistance (R_{sq}) of the TCO layer. It is an important parameter as it provides information about the lateral transport of charge carriers in the front contact of a solar cell. This property is measured at HyET using a tool that works on the principle of Ohm's law and exploiting the natural formation of an oxide layer of aluminum. This tool has been enhanced for its accuracy and robustness using a different route than its previous measurement scheme. The results from this tool have been discussed and correlated with standard Hall effect measurements and from optical measurements.

To assess the quality of the silicon layers deposited on top of the TCO layer, a non-contacting capacitive device was fabricated at HyET. The device has the capability of measuring the opto-electrical properties (short-circuit current density, open-circuit voltage, fill factor, etc,.) of a solar cell, capacitively, without any physical contact. Two methods were devised to calibrate the device, for measuring the developed capacitance (C_p) between the device and the deposited silicon layer. Moreover, the response of this device's circuit to C_p and change in frequency are illustrated through Bode plots.

From this research, it was concluded that the Drude model fitting generates sensible results for charge carrier concentration and mobility of electrons inside the TCO layer. The correlation of former seems to be stronger than the latter, with Hall effect measurement data. The thicknesses measured optically are also compared to the scanning electron microscopy (SEM) results, where the optical thickness values seem to be overestimated with respect to the SEM data. The electrical sheet resistance values obtained from the tool at HyET correlated rather better with the Hall effect measurements than those obtained from optical measurements. It was also demonstrated that the non-contacting capacitive device can be calibrated by applying an AC voltage and measuring the output response of the device via the transfer function. The circuit behaved as a band-pass filter, implying an application of AC voltage within a specific frequency region.

Contents

1 Introduction **1**
1.1 Solar energy–The future . . . 1
1.2 An overview of HyET Solar . . . 2
1.2.1 About the company . . . 2
1.2.2 Production process . . . 3
1.3 Thesis objective and outline . . . 4

2 In-line diagnostics **5**
2.1 Introduction and necessity . . . 5
2.2 APCVD and its related diagnostics . . . 6
2.2.1 Atmospheric pressure chemical vapor deposition . . . 6
2.2.2 Diagnostic hardware systems . . . 7
2.3 Diagnostic device for the PECVD process . . . 9
2.3.1 Plasma-enhanced vapor chemical deposition . . . 9
2.3.2 The non-contacting capacitive device –PIN probe . . . 10

3 In-line opto-electrical characterization of FTO **13**
3.1 Background and motivation . . . 13
3.2 Optical thickness determination model . . . 14
3.2.1 Introduction . . . 14
3.2.2 Modelling methodology . . . 14
3.2.3 Summary of the methodology . . . 19
3.3 Proposed models for utilizing the NIR spectrum . . . 20
3.3.1 Model A: An Empirical Approach . . . 20
3.3.2 Model B: Drude Model Fitting . . . 33
3.4 Results and Discussion . . . 37
3.4.1 Measurement setup . . . 37
3.4.2 Results from the in-line diagnostics . . . 38

4 Upgradation of the electrical sheet resistance measurement device **49**
4.1 Background and motivation . . . 49
4.2 The concept of Wonder measurement . . . 49
4.3 Measurement Setup–Past vs Present . . . 51
4.3.1 Measurement setup–V1 . . . 51
4.3.2 Measurement setup–V2 . . . 53
4.4 Results and Discussions . . . 57

5 Calibration of the PECVD diagnostic device **61**
5.1 Background and motivation . . . 61
5.2 Understanding the probe circuit . . . 61
5.3 Method A: Top Capacitor Approach . . . 62
5.3.1 Experimental methodology . . . 63
5.3.2 Results and discussions . . . 65
5.4 Method B: n-layer voltage application method . . . 66
5.4.1 Experimental methodology . . . 67
5.4.2 Results and discussions . . . 68

6 Conclusions and Recommendations **75**
6.1 Conclusion . . . 75
6.2 Recommendations for future work . . . 77

List of Figures

1.1 The share of electricity generated from solar energy in the world over the last decade, as a percent of the global electricity produced [1] 2
1.2 A typical flexible thin-film solar module produced at HyET [5] 2
1.3 The tandem solar cell structure as processed at HyET [6] 3

2.1 A schematic diagram of an APCVD system [10] 6
2.2 A basic schematic diagram of a spectrometer [13] 8
2.3 The two spectrometers inside the cabinet, featuring the UV-VIS and NIR spectrometers at the bottom and top respectively 8
2.4 The device for measuring the electrical sheet resistance on-line–"WONDER" 9
2.5 A simple diagrammatic representation of the PECVD process [14] 10
2.6 A simple diagrammatic representation of the PIN probe measurement mechanism . . . 10
2.7 An electrical replacement scheme of the capacitive measurement method 11
2.8 A top view of the fabricated non-contacting capacitive probe 12

3.1 Three different spectra used for obtaining the reflectance spectrum 14
3.2 The reflectance spectrum as obtained according to the equation 3.1 15
3.3 An example of Gaussian function in 1-D with mean of 0 and σ=1 according to the equation 3.2 [17] 15
3.4 Representation of FWHM and HWHM parameters [19] 16
3.5 The measured reflectance spectrum of the deposited FTO in the UV-VIS region 18
3.6 The step-by-step process flow diagram of the "Optical Thickness" determination model developed at HyET 19
3.7 The location of the "Black Wavelength" and "Slope" in the NIR reflectance spectrum of an Al + FTO sample 22
3.8 The black wavelength positions as recorded for different variations of plasma energy and thickness at 0.15 eV of damping energy 23
3.9 The relation between plasma energy and black wavelength for different thicknesses at an E_d of 0.15 eV 23
3.10 The relationship between the parameters of the obtained power equation and thickness of FTO 24
3.11 Positions of black wavelength with varying damping energies, showing a maximum of 10 nm shift with 50% increase in E_d 25
3.12 The slope values as recorded for different variations of damping energy and thickness at 0.8 eV of plasma energy 26
3.13 The relation between damping energy and slope for different thicknesses at an E_{pl} of 0.8 eV 26
3.14 The relation between slope, E_d and thickness of FTO deposited 27
3.15 The dependency of first set of coefficients (b_1 & b_2) on the plasma energy 28
3.16 The dependency of second set of coefficients (b_3 & b_4) on the plasma energy 29
3.17 The errors (in %) of prediction for "N" (in blue) and "μ" (in orange) in Set A samples . . . 31
3.18 The errors (in %) of prediction for "N" (in blue) and "μ" (in orange) for Set C samples . . 32
3.19 Result of the fitting done for the simulated (blue) and the measured (orange) reflectance (R) values 34
3.20 Incident light on the FTO and its reflection from the Aluminum/FTO interface 35
3.21 Result of the Drude model fitting done for the simulated (red) and the measured (white) reflectance values 36
3.22 The measurement setup in-line at the APCVD machine at HyET 37
3.23 A 3D view of the measurement setup 38

3.24 The reflectance spectra of different experimental settings carried out at HyET 39
3.25 The thickness profile across full foil width for settings 1 to 4 41
3.26 The thickness profile across full foil width for settings 5 to 8 41
3.27 The thickness profile across full foil width for settings 9 to 11 42
3.28 Comparison between the thickness obtained in-line and from offline measurements (the vertical error bars are not visible due to very less error spreads) 42
3.29 Two different values of thickness for a sample of setting 4, showing a difference of > 100 nm owing to the roughness and curved nature of the Al/FTO sample 44
3.30 The NIR reflectance spectra of different experimental settings carried out at HyET . . . 45
3.31 Comparison between the charge carrier concentrations obtained in-line (optically) and from offline measurements (electrically) (some of the vertical and horizontal error bars are not visible due to very less error spreads) 47
3.32 Comparison between the mobilities obtained in-line (optically) and from offline measurements (electrically) (some of the vertical and horizontal error bars are not visible due to very less error spreads) 47
3.33 Comparison between the sheet resistances obtained in-line (optically) and from offline measurements (electrically) (some of the vertical and horizontal error bars are not visible due to very small error spreads) 48

4.1 The flow of current through the Aluminum/TCO stack with a resistive inter (oxide) layer for different ratios of sheet resistance and resistance of the oxide layer [35] 50
4.2 Schematic diagram of WONDER measurement setup V1 ([35]) 51
4.3 The principle of recording the potential differences across the measurement pins with respect to the ground (GND) pin 52
4.4 Fit result of an aluminum with FTO sample placed under the probes [35] 52
4.5 Removal of five pins from the existing 19-pin WONDER tool where the removed pins are highlighted inside the red rectangle 53
4.6 The implementation of differential mode of measurement in the measurement setup . . 54
4.7 The measurement scheme of the second version of WONDER with paired pins forming channels (black dashed lines) and power supply from the DAQ on one side while being connected to ground of the DAQ on the other side 55
4.8 The channel health calibration sample as prepared for checking the measurement health of channels 0-5 55
4.9 The WONDER device pressed against the channel health calibration sample to measure the voltage drops across each channel 56
4.10 The results from the test performed on the channel health calibration sample 57
4.11 The Fit and Results cluster of the software program when a good measurement is made on the deposited FTO layer 58
4.12 A comparison between the sheet resistances obtained optically from the NIR characterization of FTO and the electrical sheet resistances obtained from the in house measurement device for 8 different settings of FTO 59
4.13 A comparison between the sheet resistances obtained from the Hall effect measurements and the electrical sheet resistances obtained from the in house measurement device for 8 different settings of FTO 59

5.1 The interim circuit design of the probe consisting of two operational amplifiers and four feedback components 62
5.2 The proposed ASAHI glass plate design, to be placed inside the probe 63
5.3 Modified glass plate for application of external AC voltage from the DAQ 63
5.4 The scenario after the glass plate was introduced inside the probe 64
5.5 The experimental setup designed for the offline testing of Method A 64
5.6 The behaviour of gain of the system as a function of frequency, for five distance variations of the metal plate from the probe area 65
5.7 The probe circuit after the inclusion of two capacitances forming a voltage divider circuit 66
5.8 The scenario after the glass plate was introduced inside the probe 67

5.9 The behaviour of gain of the system as a function of frequency, for distance variations between 0.4 and 4 mm . . . 68
5.10 The relationship between the gain of the circuit and distance between the metal plate & receiving element of the probe . . . 69
5.11 The probe circuit formed in the testing of method B . . . 70
5.12 The Bode diagram showing the correlation between the theoretical (solid line) and experimental frequency response (dash-dot line) of the system . . . 71
5.13 The Bode diagram of the probe circuit from low frequency to high frequency region, with two vertical dashed lines (in red) depicting the low and high cut-off frequencies of the system . . . 72

List of Tables

3.1 The parameters of the Drude-Tauc-Lorentz Model as obtained from the model 22
3.2 The results and comparison for Set A samples with their error percentages 30
3.3 The results and comparison for Set C samples with their error percentages 31
3.4 The results of analysis for Set A samples 35
3.5 The results of wavelength positions for Set A samples at which absorption of light was $< 1\%$ 36
3.6 The thicknesses as obtained from the optical thickness model for 11 settings using the reflectance spectra of the aluminum/FTO stack 40
3.7 The opto-electrical parameters as obtained from the Drude model fitting for 11 settings using the NIR reflectance spectra of the aluminum/FTO stack 46

4.1 The sheet resistances as obtained from the electrical sheet resistance measurement device for 11 settings of the aluminum/FTO stack 58

1
Introduction

This chapter provides an insight into the evolution of solar energy over the course of time and its future, in the first section. It is followed by an introduction of the company where this project was done and their production process of thin-film flexible solar modules. The final section presents the objectives carried out in this thesis project and the flow of content.

1.1. Solar energy–The future

The availability of energy has transformed the course of humanity over the last few centuries. New sources of energy have been unlocked – first fossil fuels, followed by a diversification to solar, hydropower and various other renewable technologies. However, since the dawn of the industrial revolution, the energy mix of most countries across the world has been dominated by fossil fuels. This dependency on fossil fuels for more than 200 years has not only led to some depletion of the total available resources but also has had several negative implications on human health. The need of the hour therefore is to reduce carbon dioxide emissions and air pollution levels as rapidly as possible. To achieve this, the future energy mix of the world must comprise of renewable energy technologies to a maximum extent. The key role of renewables will be the decarbonization of our existing energy infrastructure in the coming decades.

One such form of renewable energy is the energy produced by the nuclear fission reactions in the Sun—solar energy. The Sun emits about $3.8 * 10^{26}$ Watts of energy on to the surface of the Earth each second, which is enough to satisfy the energy demand of the entire human race for over two hours. Thus, photovoltaics along with other solar energy conversion technologies will play a crucial role in transcending this enormous amount of energy into electricity and other forms of usable energy. As per the article by Ritchie et.al., the total amount solar energy generated in the world estimates to 1040.50 TWh, from an installed capacity of 843.09 GW [1]. The share of electricity generation from solar energy has increased exponentially, from around 0.2 percent of global electricity production in 2010 to about 3.7 percent in 2021 [1], as observed from the chart in figure 1.1. This significant increase in the utilization of solar energy can be attributed to its affordability, ease of installation and integration with grid, compactness, and wide scale availability.

There exist different technologies for converting the available sunlight into electricity. Electricity can be generated directly from Sun's energy via photovoltaic technology or indirectly via concentrated solar power (CSP) technique [2]. Among the two available energy conversion technologies, it was observed that photovoltaic solar modules have a key role in the expansion of solar energy and its penetration into the energy market, thanks to its flexibility in terms of design and materials required [3]. Currently, there are three kinds of photovoltaic technologies that dominate the world: mono-crystalline silicon, poly-crystalline silicon, and thin film. Inside the domain of thin-film technologies, there is ongoing research on different materials such as perovskites and organic solar cells, that can lead to highly efficient solar cells. Crystalline silicon, including both mono and poly, is the most popular technology having a market share of about 95 percent in 2021 [4]. The share of thin film technology is expected to grow in the future

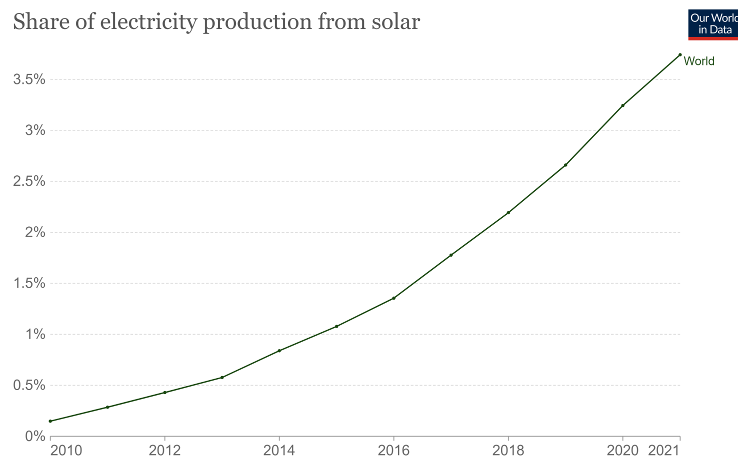

Figure 1.1: The share of electricity generated from solar energy in the world over the last decade, as a percent of the global electricity produced [1]

owing to its ease of installation, flexibility and lightweight among others. HyET Solar specializes in producing thin-film silicon solar modules, involving both single junction (amorphous silicon) and tandem (amorphous/nanocrystalline silicon) devices.

1.2. An overview of HyET Solar

1.2.1. About the company

HyET Solar, formerly known as Helianthos, is located in Arnhem, and was founded in the year 2012 post the acquisition of the firm by a private investor. Helianthos started as a spin-off from Akzo Nobel, co-partnered with Shell from 2001 to 2006. In the year 2006, it was taken over by Nuon (a part of Vattenfall). Apart from the physical and chemical R & D laboratories, it also consists of a small-scale production plant for the roll-to-roll production of thin film single junction amorphous silicon and amorphous/nano-crystalline tandem solar modules. At present, the industry is busy in expanding and up-scaling its production capacity to 40 MWp/year from its current capacity.

The company produces modules which are unique in terms of their flexibility and lightweight design, as depicted in figure 1.2. Due to these features, it is able to stand out against the commonly implemented crystalline silicon modules which are bulky, made up of glass and cannot fully cover most of the roof area due to their rigid construction. The product has a high potential for mass commercialization and easy implementation, thanks to its uniqueness in physical characteristics, provided it satisfies the performance milestones consistently. To ensure a continuous improvement in the performance and reliability of its product, HyET dedicates a major share of its resources towards their R & D segment. A series of quality inspection tests are conducted over the samples that are directly taken from the production line, to continuously monitor areas of malfunctioning, reduced performances, and including the overall physical and internal quality of the modules.

Figure 1.2: A typical flexible thin-film solar module produced at HyET [5]

1.2.2. Production process

The production of thin-film flexible solar modules at HyET Solar is done in a roll-to-roll (R2R) manufacturing processes, comprising of a series of complex steps involving deposition of all layers in house. At HyET, aluminum is used as a temporary carrier instead of glass on which further deposition processes of subsequent layers are done. The utilization of aluminum has several advantages both in terms of material and process conditions. Aluminum is an abundant and low-cost material available in the market which also allows the final product to be flexible. In terms of processing, the temporary aluminum foil ensures process homogeneity and provides the advantage of scaling up the R2R production process. Apart from this, it supports the usage of high process temperatures which assist in the production of high-quality transparent conductive oxide (TCO) and photo-active silicon layers, depicted in figure 1.3.

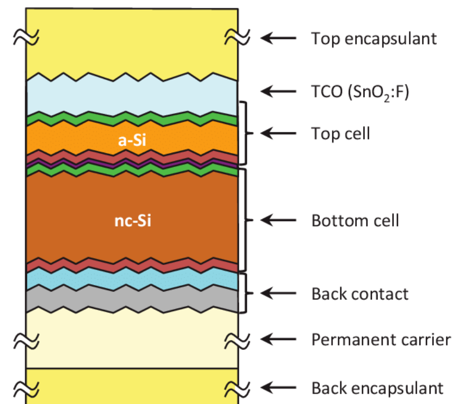

Figure 1.3: The tandem solar cell structure as processed at HyET [6]

The following text discusses the various steps in the R2R production process briefly, as given by E.Hamers et.al.,[6]:

1. ***Texturing of aluminum foil:*** At present, the aluminum foil used for production is 350 mm wide. In this step, crater-like structures are created in the foil so as to enhance the light scattering. These structures are made by a wet chemical etching procedure where diluted sodium hydroxide (NaOH) is used to etch the foil, thereby creating crater-like microstructures. Post etching, the foil is cleaned in an acidic bath of phosphoric acid (H_3PO_4) to remove any residues that would have resulted from etching of the foil.

2. ***Front TCO deposition:*** HyET stack uses fluorine doped tin oxide (SnO_2:F) as its TCO layer, which has proven to be highly stable against the corrosion that occurs from moisture and acid attack. SnO_2:F is deposited using atmospheric pressure chemical vapor deposition (APCVD) on the textured Al foil at 500 degrees Celsius. The standard thickness of this layer is 750 nm.

3. ***Silicon layer deposition:*** This process is carried out via plasma enhanced chemical vapor deposition (PECVD), as a single pass or multiple pass depending on the structure of the stack being deposited. The layers are deposited in a superstrate configuration at a radio frequency of 13.56 MHz and 200 degrees Celsius temperature. In the PECVD machine, different Si layers like p-doped, intrinsic, and n-doped are continuously deposited in different chambers. For developing a tandem structure in the machine, a two-pass method is adopted where the top cell is deposited in the first pass and bottom cell in the second.

4. ***Monolithic series interconnection:*** In this step, laser scribing is used to define the cell boundaries constituting a module. Different types of scribes are done to break different layers from adjacent cells. The first scribe is made through the SnO_2:F and hydrogenated amorphous silicon (a-Si:H) layers which is then filled with an ink, known as lift-off, to separate adjacent cells electrically. The second scribe then only penetrates the a-Si:H layer and connects the n and p-doped layers of the adjacent cells forming a series interconnect.

5. ***Back contact deposition:*** The typical back contact material used here is Al-doped zinc oxide (AZO) or only aluminum. The AZO is sputtered via radio frequency sputtering while aluminum is sputtered on the stack through DC sputtering. The standard thicknesses deposited for AZO and Al are 70 nm and 300 nm, respectively. This back contact also fills the scribes as discussed earlier in the previous step. The lift-off ink as mentioned previously is removed using a specific technique which helps in breaking the back contact from the adjacent cell.

6. ***Permanent carrier:*** To provide rigidity to the final product, the stack with the back contact is laminated on a permanent carrier foil. To ensure that the mechanical stresses are transferred onto a polymer material, an encapsulation layer is used from the back.

7. ***Removal of Aluminum substrate:*** The next step involves the etching of the temporary Al foil thereby exposing the active region of the front TCO. Here, a wet chemical etching procedure is used.

8. ***Encapsulation:*** In this final main step of processes, the modules are cut and encapsulated from the front side so as to prevent attack from any moisture or chemicals. Lastly, electrical connectors are added to finish the product.

1.3. Thesis objective and outline

To ensure that the R2R production processes produce quality material throughout all the machines in line, the diagnostics concerning each crucial process must be optimized. Better analysis of the material being produced or made will not only help in making good quality material out of the machines but also enhance the efficiency of the yield. The main objective of this thesis therefore is to establish appropriate diagnostics that will help to improve the processing of thin-film amorphous silicon modules at HyET Solar. The main research questions of this study are formulated as follows:

1. *Using the reflection spectrum of the deposited FTO, how can the information regarding the layer thickness and its electrical properties be extracted?*: This will provide insights into the thickness, charge carrier concentration, mobility, and the sheet resistance of the FTO optically.

2. *How to enhance the robustness of the current offline sheet resistance tool?*: To make the current setup more robust to future measurements of the aluminum and FTO stack and easy to troubleshoot.

3. *How to calibrate the PECVD diagnostic tool such as to obtain reliable data from the device?*: To elucidate the importance of calibration prior to performing measurements and getting data out of the device that can be trusted.

The report will guide the reader through understanding the steps and methodology undertaken in order to answer the formulated research questions. To begin with, Chapter 2 deals with the importance of in-line diagnostics in the roll-to-roll production process and provides insight into the APCVD and PECVD processes along with their respective diagnostics. The diagnostics relate to the spectrometers in the APCVD machine and the non-contacting probe in the PECVD machine. Chapter 3 discusses the methodology adopted to model the near-infrared part of the spectrum to help estimate the charge carrier concentration and mobility of the deposited FTO and thereby also in estimating its optical sheet resistance. Furthermore, Chapter 4 covers information about the existing mechanism and theory behind the offline sheet resistance tool at HyET and the upgrades/modifications done to make it more robust. It also discusses the correlation between the optical and the electrical sheet resistance obtained. Chapter 5 delves into the method of calibrating the non-contacting probe that is employed for estimating the opto-electrical properties of the deposited silicon layers of thin-film modules, so that the data obtained out of the device are reliable. Finally, Chapter 6 provides the important conclusions of the research work done and some recommendations on future research directions on further optimizing the diagnostics.

2

In-line diagnostics

In this chapter, the first section introduces the role and necessity of having in and on-line diagnostics in a R2R production facility. The following section discusses the APCVD process briefly along with the diagnostic tools employed in the machine for information retrieval. The final section describes the PECVD process and its diagnostic tool for opto-electrical characterization of the solar cells.

2.1. Introduction and necessity

Efficient extraction of the Sun's gigantic amount of energy requires photovoltaic materials and devices that are capable of efficiently converting this energy into electricity. The most commonly employed photovoltaic materials are semiconductors that convert this light energy into electrical energy via absorption of sunlight in the bulk of the material to produce mobile charge carriers (electrons and holes), which in turn produce electrical current or voltage. An ideal and successful device of such kind must possess high absorption efficiency ranging from the blue part to the infra-red part of the solar spectrum and also provide high mobility for the photo-generated carriers. In order to achieve this in a thin film photovoltaic device, continuous monitoring of the various deposited layers in the roll-to-roll manufacturing process becomes highly important. In the different production steps as discussed in the previous chapter, it is crucial that each process ranging from the cleaning of the incoming aluminum substrate to the finishing of the final product, is appropriately diagnosed for their quality. Consequently, a need exists for precise quality control during the R2R manufacturing of the thin-film photovoltaic devices [7].

The most critical steps in such a production process are the web-based deposition processes, that occur at a high speed. In these steps, deposition of layers of thin film to form a device occurs onto a moving web of the substrate material, in this case, aluminum. The web is fed from a source roll into a deposition chamber and is collected by a take-up roll after the deposition of desired layers. In the past, quality control methods were based on evaluating the performance of the device (or an individual layer) after the deposition process had occurred. Typical post-deposition quality control methods involved removing a part of the take-up roll, sampling it in appropriate size, and then examining them under appropriate characterization devices offline. Although the post-processing, contacting quality control devices and methods are fully capable of providing the relevant information that are needed in evaluating the performance and properties of the various layers of a thin film photovoltaic device, they suffer from an important disadvantage in terms of slower information feedback rates. Web processing times are typically in the order of a day and post-processing characterization takes another few days to extract information. Thereby, quality control information is available only after several days from the deposition process. The long feedback times implies that any problem which occurs during the deposition process goes undetected and remains unknown for days and also that the material processed during these days, subsequent to the onset of the problem, might be potentially defective. Once the information that comes after a few days indicates that there was a problem during deposition, more production time is lost in relating the problem to process variables and to producing new material to verify that the problem has been appropriately resolved. The production of a substantial amount of defective product and the loss of valuable production time are expensive and negatively affect the eco-

nomic feasibility of photovoltaic materials and devices [7][8].

This is where the need for an immediate in-line quality control method arises, which can provide assessment of the layers during the manufacturing process itself. For a quality control diagnostic device or process to be desirable, it should not only provide a high information feedback rate but also permit on-line correction and optimization of the manufacturing process [9]. The commonly utilized offline quality control methods or devices are limited primarily by the need to form physical electrical contacts to the photovoltaic device or material under consideration. Since this nature of evaluation is quite complex and challenging to employ on-line in a continuous manufacturing process, it is required for an inline diagnostic device or process to be as non-contacting in nature as possible, with respect to the device layers (or the device) being evaluated. Keeping these salient features of an inline diagnostic tool, different processes and designs are proposed in this report thereof. The following sections will throw light upon the processes and their respective machines in and on which the diagnostics were established.

2.2. APCVD and its related diagnostics

2.2.1. Atmospheric pressure chemical vapor deposition

Atmospheric Pressure Chemical Vapor Deposition (APCVD) has emerged as a prominent technique in the field of materials science and semiconductor manufacturing. This method facilitates the deposition of thin films onto substrates under atmospheric pressure, eliminating the need for costly and complex vacuum systems employed in traditional CVD methods. The widespread adoption of APCVD can be attributed to its inherent advantages, including simplicity, scalability, and cost-effectiveness, which are particularly advantageous for large-scale production processes.

In the APCVD process, depicted in figure 2.1, a precursor gas is introduced into a reaction chamber alongside a carrier gas, typically nitrogen or hydrogen. The substrate is then carefully heated to a temperature optimized for the decomposition of the precursor gas, leading to the deposition of a thin film on its surface. The atmospheric pressure conditions in APCVD enable higher reactant gas concentrations, resulting in significantly faster deposition rates compared to low-pressure CVD techniques. However, it is important to note that the increased pressure levels may compromise the control over film thickness and uniformity, emphasizing the criticality of process optimization for achieving the desired film properties. A notable application of APCVD lies in the deposition of silicon dioxide (SiO_2) films, widely employed as insulating layers in semiconductor devices. APCVD offers the distinct advantage of producing high-quality SiO_2 films with excellent electrical properties and remarkable step coverage, rendering it suitable for diverse integrated circuit manufacturing processes. Moreover, APCVD finds utility in the deposition of other materials, such as metal oxides and nitrides, thereby catering to the demands of functional coatings and protective layers in a broad range of industries, spanning from microelectronics to solar cell production [10].

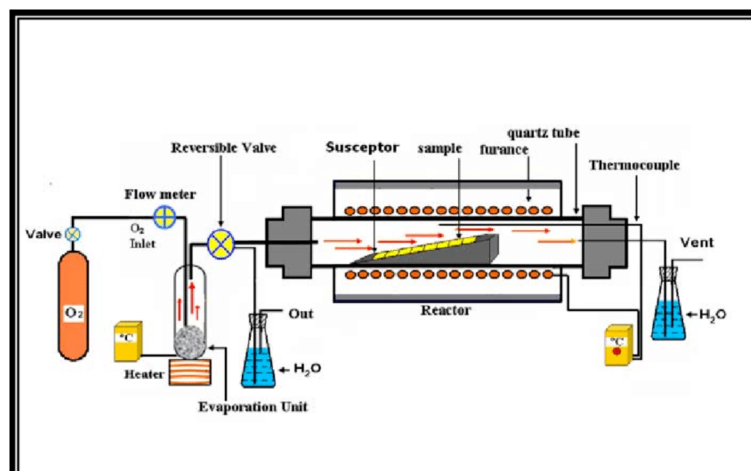

Figure 2.1: A schematic diagram of an APCVD system [10]

This process of deposition stands as a versatile and robust technique for the deposition of thin films under atmospheric pressure conditions. Its simplicity, scalability, and cost-effectiveness have positioned it as a favored choice in semiconductor manufacturing and materials science. Although APCVD may exhibit slightly diminished control compared to low-pressure CVD methods, its remarkable advantages in terms of deposition rate and suitability for large-scale production make it an attractive option for applications requiring high-quality thin film coatings.

2.2.2. Diagnostic hardware systems

Optical spectrometers

Spectrometers have a key role in providing information about the quality of the layers deposited in a thin film manufacturing industry. While the end application of thin films can vary widely, the need for accurate control over the thickness of each layer and other relevant properties during each epitaxial growth process remains consistent. One of the challenges associated with thin films is that they are very thin, typically ranging between 1 nm to 100 microns. This level of precise thickness measurement can be done using a spectrometer. Currently there are three most employed techniques to quantify the surface thickness: stylist profilometry, ellipsometry and spectral reflectance (spectrometry). While profilometry techniques are highly capable of sub-nanometer measurements, their contact nature with surface is a drawback due to longer measurement times and the risk of damaging the top surface of the layer being measured. On the other hand, ellipsometry and spectral reflectance both employ a non-contacting nature of technique, scanning large areas of the surface with little to no sample preparation. Ellipsometry is useful but is eliminated for using in-line as it is typically larger in size and more expensive, due to the fact that it requires off-axis measurement angles and multiple polarizations. Therefore, spectral reflectance becomes a favorable choice which is a polarization-independent technique done at normal incidence, thereby largely reducing the cost and complexity of the system as a whole [11]. Now, before getting to know about the spectrometers that are used at HyET for extracting relevant information for quality control, it is worthwhile to have an idea of what a spectrometer is and its working principle.

An optical spectrometer is an instrument which is used to measure the irradiance or polarization of light over a given range of wavelength through the electromagnetic spectrum. This principle of measurement is known as optical spectroscopy [12]. Using this method, the absorption of light by a particular material can be estimated through the reflection and transmission measurements performed by the spectrometer. The practical application of spectroscopy to obtain quantifiable results that can be assessed is known as spectrometry. It can be defined as a process of quantifying the amount of energy absorbed by matter and the amount of light it creates in the process. Each substance either transmits or absorbs some light. The frequency or wavelength at which the substance does this helps identify the type of substance it is. A spectrometer generally consists of an entrance slit, collimator, a dispersive element such as a grating or prism, focusing optics, and a detector [12], as depicted in figure 2.2. The working principle is based on optical physics. Light from the source passes through the entrance slit which diverges the beam on to a collimating mirror, making the beam collimated. These reflected rays are then directed towards a diffraction grating, which acts as a dispersive element that splits the incoming light into its constituent wavelengths. Once the light encounters the diffraction grating, each wavelength is reflected off at different angle. This process makes the beam divergent again, therefore the rays are made to collide with a second mirror which focuses and directs the light towards the detector. The detector then captures the incoming light spectra and measures the intensity of light as a function of wavelength, which are then digitized in the software to generate a graph [13]. Modern day spectrometers also include optical fibers to transport light from the sample to the optical bench of the spectrometer. The spectrometers used for measurement purposes at HyET fall into this type of optical spectrometers with included fiber optics for probing the light of interested wavelength range onto the deposited layers.

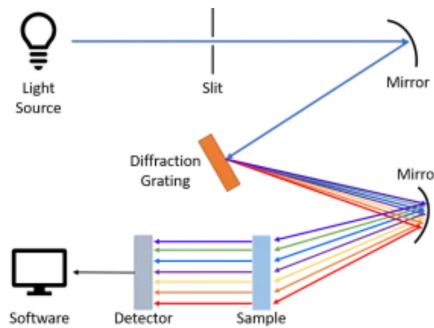

Figure 2.2: A basic schematic diagram of a spectrometer [13]

There are two kinds of spectrometers that are currently employed in house from Avantes group, as presented in figure 2.3:

1. **Multi-Channel UV-VIS spectrometer:** This type of spectrometer allows us to combine different types of channels as required in one enclosure. In this spectrometer, the spectral range from 350-1100 nm is integrated over two different channels. One of the channels is used for measuring the thickness of the thin film layers at a fixed position (typically at the center of the module) and the second one is used for probing across the width of the entire foil, to get an idea of thickness profile over the breadth. Two separate optical fibers transport light from the spectrometers, the source of which is a halogen lamp, to shine it onto the top surface of the foil after it exits the machine. In this way, calibration of the instrument becomes easier as the integration times and averaging can be set for each of the channels, making it an ideal choice for process control and plasma measurements applications.

2. **NIR spectrometer:** This is a single channel spectrometer which accommodates the near infrared part of the spectrum from 1000-2500 nm. The light source from this spectrometer is coupled with the optical fiber of the variable UV-VIS channel of the aforementioned spectrometer via another optical fiber which is capable of accommodating two different spectra of light. The purpose of this instrument is for extracting the electrical properties, like the charge carrier concentration (n), mobility (μ) and the optical sheet resistance (R_{sq}) of the deposited FTO layer across the full width of the foil. It has the capability to measure the reflectance spectrum with a resolution of 2.6 nm and allows less than 1 percent of stray light into it.

Figure 2.3: The two spectrometers inside the cabinet, featuring the UV-VIS and NIR spectrometers at the bottom and top respectively

The sheet resistance tool–WONDER

The acronym "WONDER" stands for Wonderful Non-Destructive Electrical Resistance measurement device. This is a tool which was developed in house for measuring the sheet resistance of the deposited FTO on aluminum foil. Figure 2.4 depicts the top and bottom views of the WONDER tool which is placed at the machine for measuring the electrical sheet resistance of the deposited FTO near the winder (where the roll is wound after exiting from the web). It is a rectangular shaped bracket with one handle on the top for pressing the probe against the surface of the roll. The bottom edges of the probe bracket are designed in such a way that there can be a good grip when placed on a curved surface, like the roller on which the roll traverses. In the center, one can observe the pins area which consists of 14 pins, with 7 on either side of the area. Here, the two extreme pins are for supply and return of current from and back to the source. The remaining 12 pins in between measure the voltage drop between the current probes, and generate a resistance due to the flowing current, the details about which will later be discussed in Chapter 4.

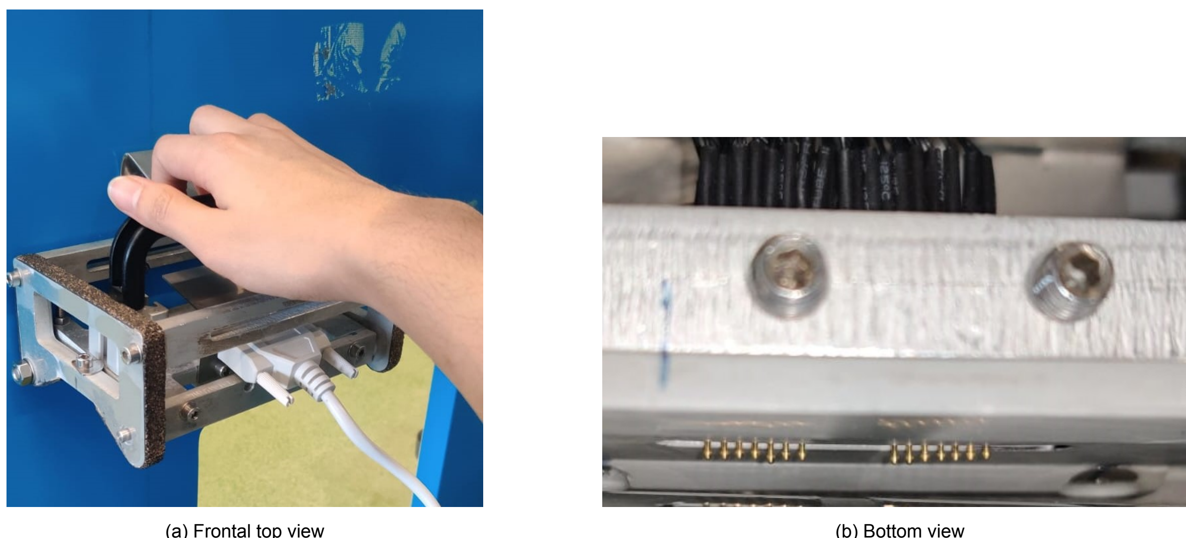

(a) Frontal top view

(b) Bottom view

Figure 2.4: The device for measuring the electrical sheet resistance on-line–"WONDER"

2.3. Diagnostic device for the PECVD process

2.3.1. Plasma-enhanced vapor chemical deposition

The plasma-enhanced chemical vapor deposition method is the most common technique that is employed for the growth of thin-film silicon materials, like amorphous silicon and nanocrystalline silicon. This process is also suitable for the deposition of different alloys of silicon, such as silicon carbide or silicon oxide. The layers being deposited can be intrinsic, n- or p-doped, depending on the requirements. PECVD process allows the deposition of thin films at lower operating temperatures, below 200 degrees Celsius. The films which are made using this method are desired to have properties like high quality, appropriate adhesion, desired coverage of textured surfaces and uniformity over the required area. The deposition process is pictorially represented in figure 2.5. In this process, a mixture of various gases such as silane (SiH_4), methane (CH_4), hydrogen (H_2), and carbon dioxide (CO_2) are introduced in an ultra-high vacuum (UHV) reaction chamber, depending upon the material desired to be produced, which are then converted into glow discharge (plasma). This conversion is controlled by an oscillating electric field between two conductive electrodes via a radio frequency (RF) signal of 13.56 MHz or a low-band very high frequency (VHF) of 50-80 MHz. This plasma, which is created is responsible for the generation of reactive radicals, neutral atoms, ions, molecules, and electrons. The maintenance of low temperature of the substrate is ensured by the composition of these reactive and high energy particles, which are the result of collisions that occur in the gas phase reactions. In other words, these atomic and molecular particles interact with the substrate under consideration, which when compared to the plasma has a lower potential, that allows the formation of the thin-film layer since only neutral or positively charged particles can diffuse towards the substrate. The main factors that affect the quality

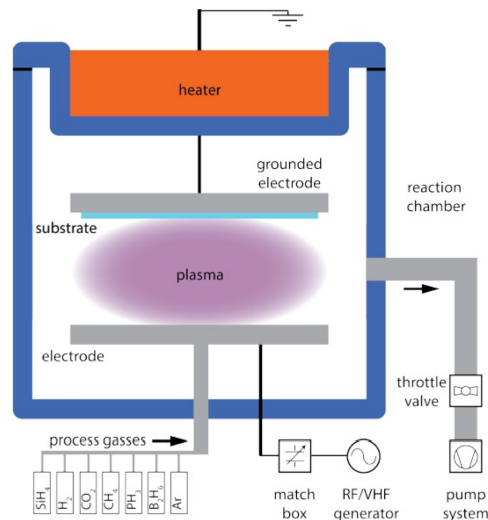

Figure 2.5: A simple diagrammatic representation of the PECVD process [14]

of the deposited layer are as follows [15]:

1. Pressure and temperature in the reaction chamber,
2. Gas flow rates of the different process gases, and
3. Power coupled into the plasma by the RF or VHF generator

2.3.2. The non-contacting capacitive device –PIN probe

The name “PIN” probe is symbolic to the fact that the device is capable of probing into the intrinsic, p-, and n-doped layers of the deposited cell stack and generating information about the opto-electrical properties of the deposited layers, the mechanism of which is illustrated in figure 2.6. It is essentially a non-contacting device which is used for the diagnostic evaluation of photovoltaic and semiconductor devices and materials. This device has the capability of sensing the developed electric field in the device or material capacitively, to generate an electric signal corresponding to the sensed field. From this generated signal, different parameters related to the properties, performance, and operational characteristics of the photovoltaic device under evaluation can be readily derived. The non-contacting nature of this diagnostic tool makes it an appropriate choice for on-line monitoring, evaluation, and quality control of continuous manufacturing processes of photovoltaic and semiconductor devices and materials. This implies that the measurement of performance parameters is done remotely and without a physical connection between the diagnostic device and the material under evaluation.

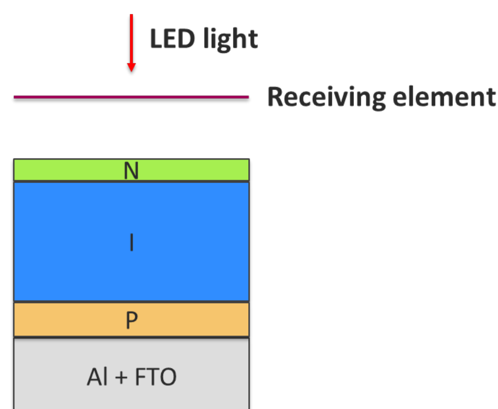

Figure 2.6: A simple diagrammatic representation of the PIN probe measurement mechanism

The working mechanism of this device is as follows. It combines a pulsed light source for excitation of the photovoltaic device being evaluated and a circuit for detecting the induced electrical effects of the device due to this pulsed light. The motive of using this pulsed light source is to excite an electron from the valence band to the conduction band of a semiconductor layer of the device. Ergo, the pulsed light acts as a source of photons which are incident on the material with an energy at or above the bandgap energy of at least one layer of the device stack. Subsequently, the excitation of electrons from valence to conduction band leads to the formation of two types of mobile charge carriers: positively charged holes in the valence band and negatively charged electrons in the conduction band. Due to this fact, the electrons and holes are spatially separated from each other, which in turn leads to the creation of an electric field inside the photovoltaic device. This induced electric field then produces a voltage that characterizes the performance and operational characteristic of the layer(s). The detection of this electric field or voltage is made possible via a sensing circuit that is located inside the device and not in physical contact with the material being evaluated. It consists of a receiving element that responds to the induced electric field due to the p/i/n stack by developing a charge, voltage, current or other electrical effect that correlates to or is proportional to the electrical field, as depicted in figure 2.7. In this figure C_{stack} represents the capacitance of the PIN stack, C_p denotes the capacitance between the n-layer of the solar cell and the receiving element and V_p is the voltage that is generated due to the effective capacitance (C_{stack} & C_p). The response of this receiving element can then be utilized to evaluate the properties of the photovoltaic material [16]. At HyET, the receiving element of the sensing circuit is a transparent conducting oxide (FTO) on a thin glass plate.

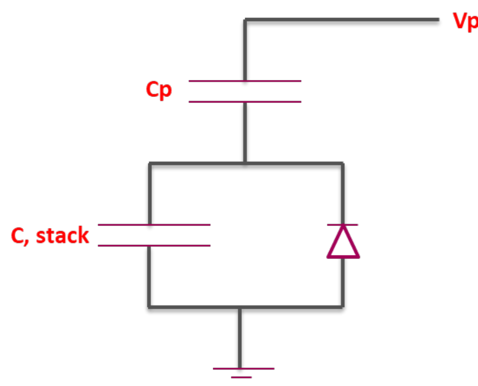

Figure 2.7: An electrical replacement scheme of the capacitive measurement method

The spatial gap between the photovoltaic device and the conductive glass plate possesses a dielectric capacitance that is characteristic of the material present between them (e.g., air) and its thickness. As a result, the dielectric material present in the gap and the two enclosed surfaces, one from the photovoltaic layer and other from the conductive glass plate, form a capacitor. The standard theories of dielectric capacitors suggest that a voltage or current can be induced on the conducting material (here the receiving element) whenever the voltage difference between two conductors (photovoltaic material and the receiving element) varies in time. Here, the time varying electric field and voltage in the photovoltaic device is developed due to the pulsing of the light source. And the magnitude of the electric signal (voltage or current) induced in the conducting glass plate depends on the magnitude and time variation of the experiences, composition, and thickness of the dielectric between the spatial gap of separation. Moreover, the electric field experienced by the receiving element depends upon the intensity, duration, and repetition rate (period) of the light pulse and the intrinsic electrical properties of the photovoltaic material. Therefore, the resulting electric signal can be understood as a characteristic of the photovoltaic material under consideration [7][9]. The probe is placed within a very close proximity of the semiconductor device or cell stack so as to ensure that the electrical effects from it due to the flashed light are correctly picked up by the sensing circuit.

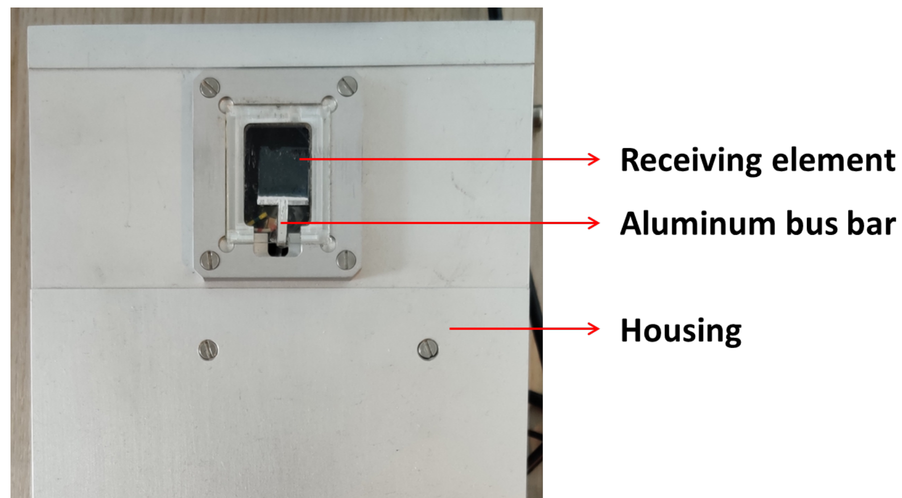

Figure 2.8: A top view of the fabricated non-contacting capacitive probe

Figure 2.8 illustrates the in-house fabricated device at HyET to measure the opto-electrical properties of deposited silicon layers. In the top view of this device, it can be observed that the receiving element is stuck onto a transparent glass plate. Light of a specific wavelength is passed through this glass plate on to the silicon layers and the consequent electric field develops a voltage on the layer that is directly under the device. This developed voltage is then capacitively picked up by the conducting receiving element and sent to the internal circuit via the aluminum bus bar to produce an output voltage, characteristic of the photovoltaic device. The entire sensor area is mounted on a sturdy metal housing. The calibration and behaviour of this device is explained in detail in Chapter 5.

3

In-line opto-electrical characterization of FTO

This chapter deals with the methods that are used to characterize the deposited FTO in the APCVD machine at HyET. The first section provides the background and motivation for implementing the near infrared characterization method in-line, followed by the explanation of the optical thickness determination model in the second section. The third section discusses the two models that were proposed for extracting information about the electrical properties of the layer from the infra-red part of the reflection spectrum. Finally, the implementation of the methods collectively in-line is discussed in the fourth section along with some results from the FTO deposition runs that were carried out.

3.1. Background and motivation

To get an idea of the quality of FTO deposited in the APCVD process at HyET, the optical thickness method was solely employed. This method utilizes the ultraviolet and visible part of the reflection spectrum from the FTO to estimate its optical thickness, which is then converted into actual thickness by dividing by the refractive index of the layer, which shall be explained in detail in the following section. But only obtaining the optical thickness of the material as a part of quality control was not sufficient to fully categorize the deposited material as “good” or “bad”.

Therefore, it was deemed necessary also to extract vital information which is also contained in the near infrared part of the spectrum. The motivation behind implementing this characterization method in-line in the APCVD machine was the possibility of extracting the electrical properties, optically from the reflection spectra of the deposited FTO in the NIR region. The electrical properties include concentration of charge carriers in the material, their mobility inside the layer and the resistance offered by the material. This additional improvement in the quality control procedure at HyET will provide a wholesome characterization of the material being deposited. At the same time, it will reduce the dependency on offline QA/QC methods of determining the electrical properties of the FTO, which will save about 2-3 days of post-processing time. Hence, the information relevant for improving the quality of the material will become available instantaneously while the deposition process is ongoing. In the sections that follow, the reader shall go through two different models that were proposed to extract the aforementioned parameters.

3.2. Optical thickness determination model

3.2.1. Introduction

For obtaining the thickness of the different layers in the thin-film solar cells/modules, a general way of measuring it is to perform a scanning electron microscopy (SEM) analysis cross sectionally on one part of the deposited material on the substrate. This method of thickness determination is very accurate and results in a small error. However, implementation of such a method in the roll-to-roll deposition processes of thin-film solar modules is in fact very complex and not feasible. It is mainly due the requirement of a vacuum for the SEM analyis. Apart from this fundamental problem, the enormous amount of space and the appropriate placing conditions are also contributory aspects which do not permit the deployment of this method in-line during the deposition process. Considering these conditions, an alternative method of determining the thickness of the deposited material arises which can be easily implemented in terms of hardware and in the software as well.

The method that meets these criteria is called the “optical thickness (OT) method”, as the thickness of the deposited FTO is determined optically, developed by **Edward Hamers at HyET**. The methodology adopted in developing the model is described in detail here, which was **transferred in a oral communication** from E.Hamers. This method uses the UV-VIS spectrometer to guide the light of that region onto the top surface of the FTO layer exiting the machine, through an optical fiber. The light that is shined thus generates a reflectance spectrum which is a characteristic material property of the layer under evaluation. The software in which the model is built, then collects this spectrum and generates the optical thickness values along the length and breadth of the foil on which the FTO is deposited, the methodology of which is mentioned in detail in the following section. This obtained optical thickness is then converted into the actual thickness by dividing by the (assumed) refractive index of the material, here FTO. The reliability and error margins of the thickness obtained through this method are compared to some cross-sectional SEM values later in this chapter.

3.2.2. Modelling methodology

Before describing the methodology used to obtain the optical thickness, it is important to know how the measured data are generated. Light from both the spectrometers is probed on to the surface of the deposited FTO on the aluminum substrate via the optical fibers. A reflectance spectrum, characteristic of the material under evaluation, is then generated as depicted in figure 3.2, where the red part of the spectrum indicates the UV-VIS region and the green part is the NIR region. Hereafter in this section the spectrum of interest is the UV-VIS part of the spectrum (red), while the modelling of NIR spectrum (green) will be discussed in the next section. To obtain the reflectance spectrum, a series of steps are undertaken. A raw spectrum as shown in figure 3.1a is generated when the light probes the sample under consideration. Figure 3.1b indicates the dark spectrum of the spectrometer considering no sample in front of it, so as to sense the amount of noise present in the source. The lamp spectrum is the characteristic spectrum of the light source of the spectrometers, shown in figure 3.1c. After the

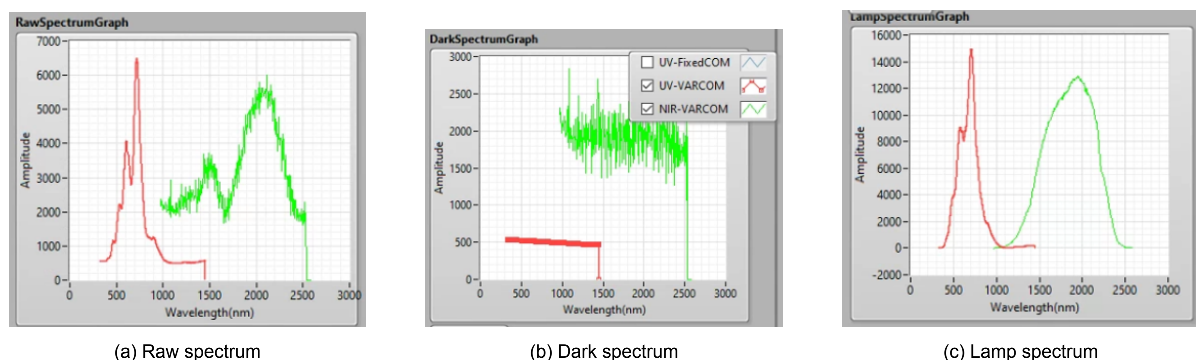

(a) Raw spectrum (b) Dark spectrum (c) Lamp spectrum

Figure 3.1: Three different spectra used for obtaining the reflectance spectrum

three spectra are obtained, the difference between the raw (r(λ)) and dark spectrum (d(λ)) is divided by the difference of the lamp (l(λ)) and dark spectrum (d(λ)) to generate the reflectance spectrum (R(λ)).

Mathematically, the relation can be expressed as,

$$R(\lambda) = \frac{r(\lambda) - d(\lambda)}{l(\lambda) - d(\lambda)} \tag{3.1}$$

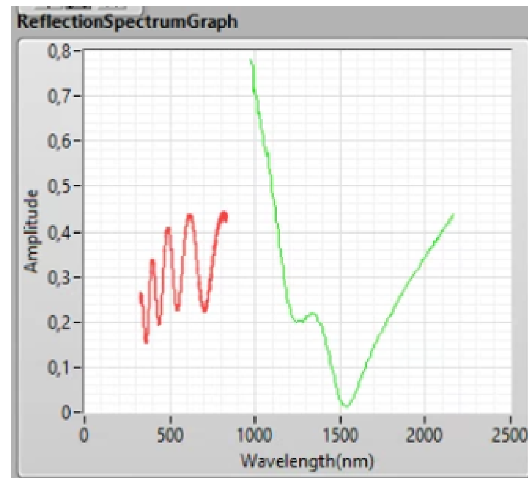

Figure 3.2: The reflectance spectrum as obtained according to the equation 3.1

The determination of optical thickness of the deposited FTO from this measured reflectance spectrum is achieved through a coagulation of several steps, which are described as follows:

1. The measured data (reflectance spectrum of the UV-VIS region presented in figure 3.5) are taken as an input, on which a Gaussian smoothing filter is applied. An example of 1-D Gaussian distribution is depicted in figure 3.3. The Gaussian distribution function in one dimension is mathematically expressed as,

$$G(x) = \frac{1}{\sqrt{2\pi}\sigma} \exp(-\frac{x^2}{2\sigma^2}) \tag{3.2}$$

where σ is the standard deviation of the function. The two main reasons for applying this filter

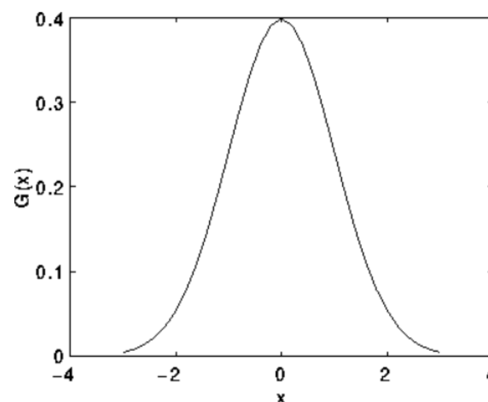

Figure 3.3: An example of Gaussian function in 1-D with mean of 0 and σ=1 according to the equation 3.2 [17]

are, first, to smoothen out the measured spectrum by removing the unwanted noise present in the data that can lead to inaccurate results and, second, a Gaussian curve never reaches zero as it extends from -(∞) to +(∞) which ensures that no data point in the measured spectrum is left out. The full width half maximum of the applied Gaussian is defined to be 10 pixels. The full width half maximum (FWHM) is a parameter that is commonly used to describe the width of a ”bump” on the curve or a function. It is given by the distance between points on the curve at which

the function reaches half of its maximum value [18]. The half width half maximum is half of the full width half maximum, which is also equal to the standard deviation of the Gaussian function (σ). Figure 3.4 illustrates both the parameters for a 1-D Gaussian. The FWHM for a Gaussian

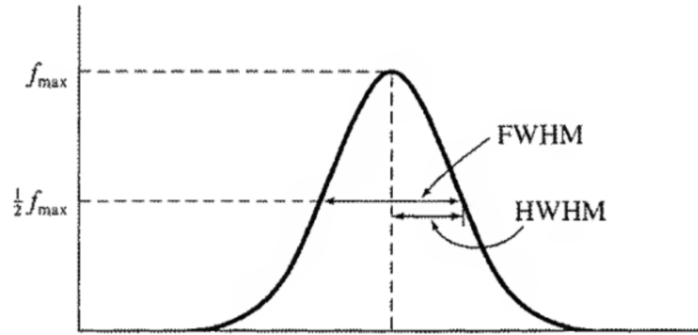

Figure 3.4: Representation of FWHM and HWHM parameters [19]

distribution function is related to its standard deviation by,

$$FWHM = 2\sqrt{2 \ln 2}\sigma \tag{3.3}$$

Substituting the defined value of FWHM as 10 pixels in the equation 3.3, we obtain σ = 4.25. Then an averaging is done based on this value of σ, which ranges from -3σ to +3σ, because in practice the function is effectively zero beyond these limits.

2. After the averaging step, a straightforward convolution is performed on the obtained data on the Gaussian filter. The type of convolution which is performed here is discrete, using the fact that the Gaussian function in 2-D is separable. Therefore, the convolution can be implemented by first convolving the data along the rows and then along the columns [20]. Once the direct convolution is implemented, the slope of the function needs to be determined. This is done by defining a kernel, which is a 3x1 matrix of [-1 0 1], when multiplied with the resulting data points generates their absolute values. These absolute values of each data point are then added up to give one value for that particular group of points, which is a representation of the value of the median data point. Here, as the kernel defined has three elements, one group has a size of three data points.For instance, consider a Gaussian in the range of -3σ to +3σ which generates arbitrary points of different amplitudes (values in the y-axis).

   Now, let us consider a total of 12 points, out of which 6 points have an amplitude of 5 and the other 6 points show an amplitude of 7. When multiplied by the kernel matrix, three points will be taken at once (here, first, second and the third point) and the resulting matrix of the values then becomes [-5 0 5], which when summed up gives 0 as the value of median point (say, MP1). Similarly, when we take the next set of three points (second, third and fourth), they will also generate a final median value of 0 (say, MP2) as they have the same amplitude. This will continue repeating itself until the 5th point (MP4). But when the kernel reaches the transition region of amplitude from 5 to 7, the net value is no more 0. This is because at the 6th point, the resulting matrix considers the fifth, sixth and the seventh point which results in a matrix of [-5 0 7]. Therefore, the final median value becomes 2 (MP5). This will also be the case for MP6.

   From MP7 onwards again the median values start repeating themselves at 0, as the amplitudes remain fixed at 7. This will continue until the second last point of amplitude 7 is reached after which there is either an increase or decrease in the amplitudes. This set of median values have a particularly defined symmetric matrix (about zeroth point) which is defined as, [-1 -2 -2 -1 0 1 2 2 1]. Following the method as mentioned, the MP1...MPn can be represented in the form of a block wave from which the slope of the measured spectrum can be estimated. Therefore, this method is also known as the ”slope detector” method.

3. The resulting dataset of the slope values within the matrix range, as specified above, is then converted and returned within the boundaries (upper and lower limit) of the UV-VIS region of the

measured reflectance spectrum. The range of interest in this case is taken from 400 nm (λ_i) to 950 nm (λ_f). This step is done by converting the x-axis of the obtained slope graph to a more visualizable scale by a formula, which can be expressed as,

$$X_{eff} = \frac{\frac{1000}{\lambda_i} - \frac{1000}{\lambda_f}}{N_T} \tag{3.4}$$

where, X_{eff} is the new effective value of the x-axis and N_T is the total number of datapoints in the slope detector graph. The reason for dividing the lower and upper limits of the wavelength range is due to the fact that the UV-VIS region can be considered to end at 1000 nm. This conversion ensures that the points in the x-axis are spaced equidistantly with each other with a spacing of 0.01 electron-Volts ($\frac{1}{100}^{th}$ of an eV). Now, the new resulting slope spectrum is graph consisting of the positive and negative slopes, as illustrated in figure 3.5a, (amplitudes in the y-axis) versus the new wavelength spectrum scale according to the formula in equation 3.4. This information retrieved is then converted into a block wave according to the sign (-ve and +ve amplitudes) of the slope values.

4. After obtaining the block sign wave from the previous step, an auto-correlation step is implemented on this slope spectrum, first without any normalization. The auto-correlation function provides information about the hills and valleys across the surface of a spectrum or signal [21]. The auto-correlation $R_{xx}(t)$ of a function x(t) is defined as [22],

$$R_{xx}(t) = x(t) \otimes x(t) = \int_{-\infty}^{\infty} x^{\bullet}(\tau)x(t+\tau)\,d\tau \tag{3.5}$$

where the symbol $\otimes$ denotes the correlation and τ indicates the integration step.
This auto-correlation function is implemented in a discrete manner. And for the discrete implementation of the function in equation 3.5, let Y represent a sequence that can have negative index values and let N be the number of elements in the input sequence X. Here, it is assumed that the indexed elements of X that lie outside its range are equal to zero, as shown in the following relationship,

$$x_j = 0, \forall j < 0, j \geq N \tag{3.6}$$

Then the auto-correlation function obtains the elements of Y using the following formula:

$$Y_j = \sum_{k=0}^{N-1} x_k^{\bullet} \cdot x_{j+k}\ , \tag{3.7}$$

for *j = -(N-1),-(N-2),...,-1,0,1,(N-2),(N-1)*
The elements of the output sequence $\mathbf{R}_{xx}$ are related to the elements in the sequence Y by,

$$R_{xx_i} = Y_{i-(N-1)} \tag{3.8}$$

for *i = 0, 1, 2,...., 2(N-1)*
After this auto-correlation is done, a direct convolution with Gaussian smoothing is repeated again on the resulting spectrum with the same parameter values of FWHM and σ as mentioned before in the first point. Normalization is then performed on this spectrum in which each obtained element of the sequence is divided by the element having the maximum value. This step then generates a symmetrical function about the y-axis, of which only the positive half is considered for further processing of the data.

5. The symmetric function obtained thereof is passed through a peak detection function in the program which finds the locations and amplitudes of the peaks and valleys in the signal, an example of which is depicted in figure 3.5b. The width of the peak detection function is defined to be 8 pixels. The significance of this width is that the function tries to fit a parabola considering the number of points equal to the defined width of the function, which for this case, is eight. Thus based on this fitting it determines the locations and amplitudes of the resulting minima or maxima

among these 8 points. Following this a check function is employed which ensures that the absolute value of the amplitude is larger than 5% confidence level of the auto-correlation function. This confidence level (C.L.) is given by,

$$C.L. = \frac{2}{\sqrt{2n}} \tag{3.9}$$

where *n* is the number of data points in the positive half of the symmetric function taken into consideration previously.

The locations of the maxima and minima are then numbered as a function of their order. Order is defined as the numbers assigned to the peaks (maxima) and valleys (minima). For a maxima a whole number is assigned while for a minima a scale of half is used. For example, 0.5 is assigned if there is a minima and 1 is assigned if there is a maxima. These orders are then returned as function of $\frac{1000}{\lambda}$ (nm^{-1}) and are arranged in appropriate (ascending) manner.

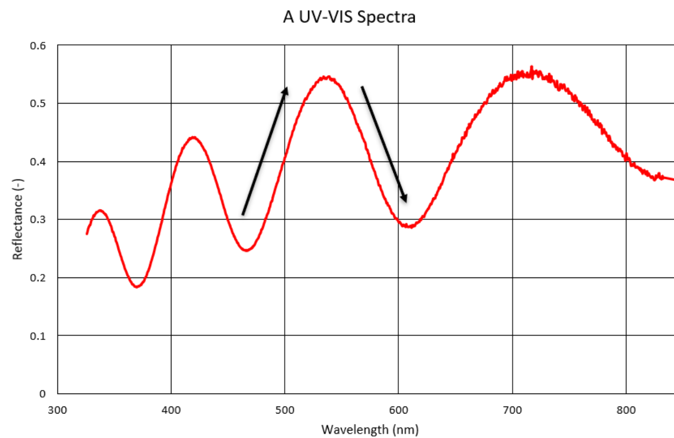

(a) The increasing and decreasing slopes in the spectrum

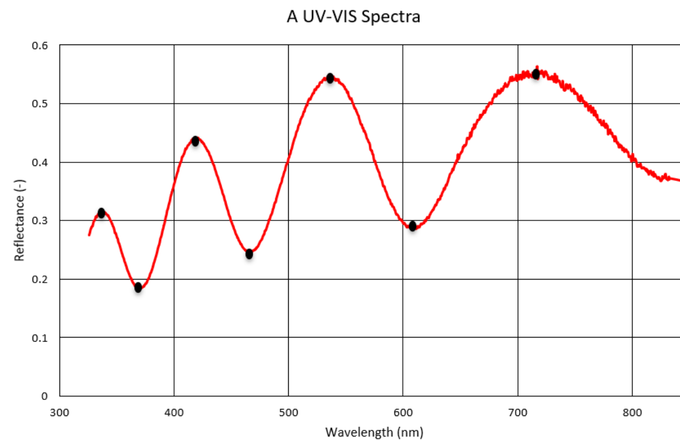

(b) The maxima (peak) and minima (valley) of the interference fringes as seen in the spectrum

Figure 3.5: The measured reflectance spectrum of the deposited FTO in the UV-VIS region

6. The last and final step is fitting of the obtained data points. In this step, a least squares curve fitting, passing through origin, is applied to the data points where the sum of squared errors between the measured and the fitted values is calculated and minimized. After minimization, it produces a linear fit of all the orders taken as input and gives out the values of optical thickness (in nm) and their errors. There are two main parameters that indicate the trustfulness of this fit, namely, the R-square score and the Donkerbroek parameter.

R-squared is often used as goodness of fit measure for different types of regression models. It measures the strength of the relationship between the model and the dependent variable on a scale of 0 to 100% or 0 to 1 in absolute scale [23]. The closer the value of R-square is to 100% (1), the better is the match between the modeled data and the measured data. The Donkerbroek parameter (DBP) is closely related to the R-square value as it assigns a value to the fit depending upon the number of 9's present in the R-squared value, e.g., 0.99 corresponds to a DBP of 2. Mathematically, it is given by,

$$DBP = -\log_{10}(1 - Rsquare) \tag{3.10}$$

The optical thickness obtained from this method is then converted into actual thickness of the deposited FTO layer by dividing the value by the refractive index (n_0) of the FTO. From HyET internal literature, this value of refractive index was found out to be **2.305** [24]. Hence, the expression for thickness of the FTO layer (in nm) is given by,

$$d_{FTO} = \frac{d_{opt}}{n_0} \tag{3.11}$$

The results of thicknesses for the different settings of a experiment done in the APCVD machine at HyET is discussed later in this chapter. The comparison between the obtained thickness from this optical model and that of cross SEM is also provided.

3.2.3. Summary of the methodology

In this section, a flow diagram is illustrated in figure 3.6 to summarize the steps incorporated in the optical thickness (OT) method. There are a total of six important statistical methods that are utilised to process the raw (noisy) measured spectrum into usable data, in terms of the layer thickness. The second and the third steps consist of one sub-step each which prepares the data set for the subsequent process.

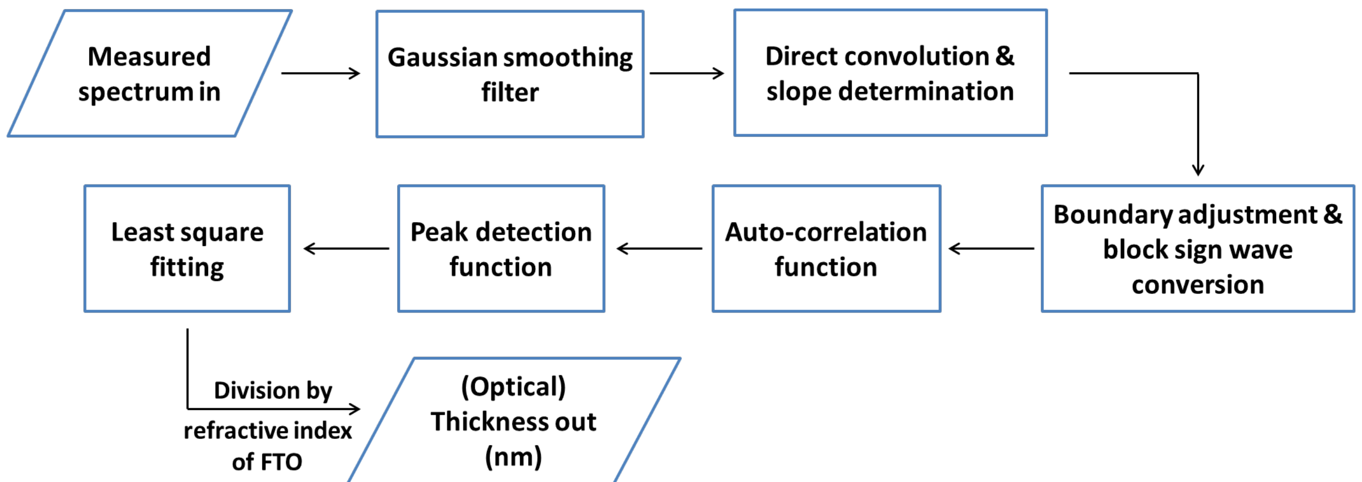

Figure 3.6: The step-by-step process flow diagram of the "Optical Thickness" determination model developed at HyET

3.3. Proposed models for utilizing the NIR spectrum

This section discusses two approaches which were modelled for the extraction of information contained in the full reflectance spectrum of the aluminum with FTO stack. As described in the previous section, the spectrum in the ultraviolet and visible region gives us the thickness of the deposited FTO. Herein, the part of the spectrum in the IR region shall be explored in terms of what can be obtained. From past research, it is evident that indeed there exists some relation between the optical and the electrical parameters of the material [25], which forms the basis of developing such model(s). Electrical determination signifies the parameters "*N*", corresponding to the charge carrier concentration and "μ", signifying the mobility of the electrons in the deposited TCO layer. The first model involves an empirical analysis where the effect of the reflectance spectrum in the UV-VIS region on the NIR part is considered. While in the second approach, a model was developed considering only the Drude model part, explained later in the section, which is independent of the UV-VIS part of the spectrum.

3.3.1. Model A: An Empirical Approach

Literature review

Before describing the methodology adopted and the route followed to develop this model, it is worthwhile to look at the two main governing theories. The first part is known as the Drude model, which is used to describe the permittivity of the material due to the absorption of the free charge carriers in the infrared region. The second part is a Lorentz oscillator, which is a subset of the Tauc-Lorentz model considering the bandgap as zero, to describe the permittivity of the material due to the bandgap absorption at photon energies in the ultraviolet region. The equations involved in these two parts are:

1. **The Drude Model:** The Drude model developed by the German physicist, Paul Drude, can be described in terms of permittivity as [26],

$$\varepsilon_{Drude} = 1 - \frac{E_{pl}^2}{E_{ph}^2 + E_d^2}[1 - j\frac{E_d}{E_{ph}}] \tag{3.12}$$

where E_{ph} is the energy of the incident photons which is related to wavelength (in nm) by,

$$E_{ph} = \frac{1240}{\lambda} eV \tag{3.13}$$

The plasma energy E_{pl} and the damping energy E_d depend on the density and mobility of the free electrons in the material respectively. Because of the complex nature of the permittivity, the factor *j* appears in the equation, where $j = \sqrt{-1}$. There exists a physical relation between these Drude parameters and the density and mobility of the free electrons. The equations relating the plasma energy (E_{pl}) to the concentration of free charge carriers are deduced from the Liberman-Lichtenberg relations as ([25]),

$$E_{pl} = h\omega_{pl} \tag{3.14}$$

$$\omega_{pl} = \sqrt{\frac{e^2 N}{\varepsilon_0 m_{eff}}} \tag{3.15}$$

substituting equation 3.15 in equation 3.14, we get,

$$E_{pl} = h\sqrt{\frac{e^2 N}{\varepsilon_0 m_{eff}}} \tag{3.16}$$

which can further be expressed in terms of eV as,

$$E_{pl}[eV] = \frac{h\omega_{pl}}{e} = \sqrt{\frac{h^2 N}{\varepsilon_0 m_{eff}}} \tag{3.17}$$

This yields an expression for the electron density, in m^{-3}, which can be written as,

$$N = \frac{\varepsilon_0 m_{eff}}{h^2} E_{pl}^2 \tag{3.18}$$

The mobility of these free electrons, in $m^2/V\cdot s$, can be deduced from the damping equation in [25] as,

$$\mu = \frac{eh}{m_{eff}E_d} = \frac{h}{m_{eff}E_d[eV]} \tag{3.19}$$

It can be observed from the above relations that this 'n' and 'μ' depend on a parameter, m_{eff}, known as the effective mass of the carriers inside the material, which depends on the conduction band shape inside the material, that is, this property of the material depends up on the incident photon energy (E_{ph}). According to [27],

$$\frac{1}{m_{eff}} = \frac{1}{h^2}\frac{d^2E}{dk^2} \tag{3.20}$$

which implies that if non-parabolic conduction bands are present, the effective mass of the electrons might change. Here, *E* is the electron energy and *k* is the momentum of the electron. However, the conductivity (σ), in $\Omega^{-1}m^{-1}$, of the material is independent of the effective mass of the electrons, which can be written as,

$$\sigma = Ne\mu = \frac{e\varepsilon_0 E_{pl}^2}{hE_d} \tag{3.21}$$

Therefore, the sheet resistance of the material, in Ω/sq, can be determined as,

$$R_{sh} = \frac{1}{\sigma d} \tag{3.22}$$

where *d* is the thickness of the TCO layer in nanometers.

2. **The Lorentz Model:** To describe the Lorentz oscillator, the following formulas are employed, which are taken from [28],

$$\zeta^4 = (E_{ph}^2 - \gamma^2)^2 + \frac{\alpha^2 C^2}{4} \tag{3.23}$$

where $\alpha = \sqrt{4E_0^2 - C^2}$, and $\gamma = \sqrt{E_0^2 - \frac{C^2}{2}}$.

$$aatan = (E_{ph}^2 - E_0^2)E_0^2 \tag{3.24}$$

$$\varepsilon_{Lorentz} = \varepsilon_{1Lorentz} + \varepsilon_{2Lorentz} = -\frac{A * aatan}{\zeta^4 E_0} + j\frac{AE_0CE_{ph}^2}{(E_{ph}((E_{ph}^2 - E_0^2) + C^2E_{ph}^2))} \tag{3.25}$$

In this model, the parameters A, C and E_0 signify the amplitude, damping and the position of the Lorentz oscillator. All these parameters have the dimension of energy and can therefore be expressed in eV.

The permittivities thus obtained from the two models can then be added to obtain,

$$\varepsilon_1 = Re(\varepsilon_{Drude} + \varepsilon_{Lorentz}) \tag{3.26}$$

$$\varepsilon_2 = Im(\varepsilon_{Drude} + \varepsilon_{Lorentz}) \tag{3.27}$$

The refractive indices of the material, $\tilde{n}$ = n + *j*k can then be expressed in terms of Drude and Lorentz permittivity as,

$$n_{TCO} = \sqrt{\frac{1}{2}[\sqrt{\varepsilon_1^2 + \varepsilon_2^2} + \varepsilon_1]} \tag{3.28}$$

$$k_{TCO} = \sqrt{\frac{1}{2}[\sqrt{\varepsilon_1^2 + \varepsilon_2^2} - \varepsilon_1]} \tag{3.29}$$

From the theories mentioned above, the primary objective was thus targeted to extract the plasma and the damping energies of the deposited FTO from the NIR part of the reflection spectrum. The methodology followed to achieve this is discussed thereof.

It is important to note that the model A is an extension of a pre-existing Drude-Tauc-Lorentz model, done by E. Hamers [24]. In the model developed, Hamers concluded his findings about the Drude and Lorentz parameters that gave the best fit (measured vs simulated data) and results for the thickness of the FTO layer, when tested against 10 settings of experiment. These values that resulted from the conclusion of the model form the basis for continuation of this theory.
The parameters as obtained from the study are summarized in table 3.1, along with their physical meanings. Henceforth, these values of the Drude and Tauc Lorentz parameters are referred to as **"Baseline"** values.

Table 3.1: The parameters of the Drude-Tauc-Lorentz Model as obtained from the model

Parameter	Symbol	Value	Unit
Density	A	21.3	eV
Damping Lorentz	C	0.15	eV
Resonance Energy	E_0	7.3	eV
Plasma Energy	E_{pl}	1.3	eV
Damping Drude	E_d	0.15	eV
Thickness	d_{FTO}	750	nm

Methodology adopted

The steps followed to extract the charge carrier concentration (N) and the mobility (μ) from the plasma and the damping energies respectively, according to the Lieberman-Lichtenberg relations as given in equations 3.18 and 3.19 are described as follows:

1. **Parameters of interest in the NIR spectrum:** To extract the plasma and the damping energies of the FTO, there are two important characteristics of the reflected intensity in the NIR region which need to be considered. The first one is the "black wavelength" (also known as the plasma wavelength), which is defined as the wavelength where the net reflectance of the aluminum with TCO stack can be approximated as zero, implying that the reflectance from the stack of aluminum and FTO cancels out. The position of this wavelength depends therefore on the optical properties of both the substrate (aluminum) and the deposited TCO [24]. The second parameter of interest is the "Slope", which is the increasing part of the reflectance spectrum for wavelengths above the black wavelength. The locations of these parameters are depicted in figure 3.7.

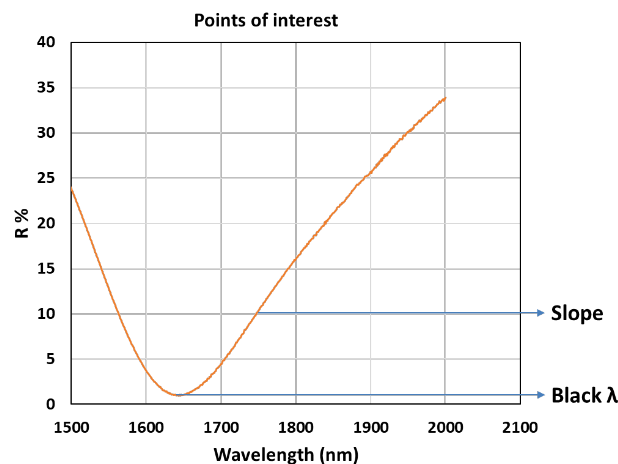

Figure 3.7: The location of the "Black Wavelength" and "Slope" in the NIR reflectance spectrum of an Al + FTO sample

2. **Relation of the parameters of interest and the Drude parameters:** By using the optical model as established earlier by Edward Hamers [24], relations between the different parameters were observed. Before beginning the analysis for developing the model, it was decided to only consider varying the Drude parameters, as the Lorentz energies are more related to the UV-VIS part of the reflectance spectrum. One of the other reasons for this decision was the direct relation of the plasma and damping energies with the electron density and their mobilities. Therefore, we began varying the Drude model parameters (E_{pl} and E_d) as well as the thickness of the TCO layer (d_{FTO}), to factor in also the effect of the layer thickness in the model. Thus a series of experiments were designed, where the three parameters were varied against each other to obtain the "black wavelength (λ_B)" and "slope" at each point.
First, the analysis for the obtained λ_B's for different settings were done. The analysis was done through a series of graphical and empirical analysis, as discussed below:

   (a) The first step was recording the black wavelength at different values of plasma energies, thicknesses of the FTO deposited, and damping energies. The data were gathered in the form of a contour table, as depicted in figure 3.8. In this table, the plasma energy (E_{pl}) was varied from 0.8 eV to 1.5 eV (across the vertical axis of the table) and the thickness of FTO was varied from 690 nm to 810 nm (across the horizontal axis of the table). This set of variations was repeated for different values of damping energy, ranging from 0.08 eV to 0.15 eV. The black wavelength at each setting was determined by matching the index of the minimum reflection in the wavelength range from 1400 nm to 3000 nm, in Excel.

		Lambda_b contour (in nm) with E_d as 0.15 eV				
		d_FTO (nm)				
		690	720	750	780	810
	0.8	2678	2701	2722	2741	2758
	0.9	2422	2439	2455	2469	2482
	1	2208	2222	2233	2244	2254
E_pl (eV)	1.1	2028	2038	2048	2056	2064
	1.2	1874	1883	1890	1897	1903
	1.3	1742	1749	1755	1761	1766
	1.4	1627	1633	1638	1643	1647
	1.5	1527	1532	1536	1540	1543

Figure 3.8: The black wavelength positions as recorded for different variations of plasma energy and thickness at 0.15 eV of damping energy

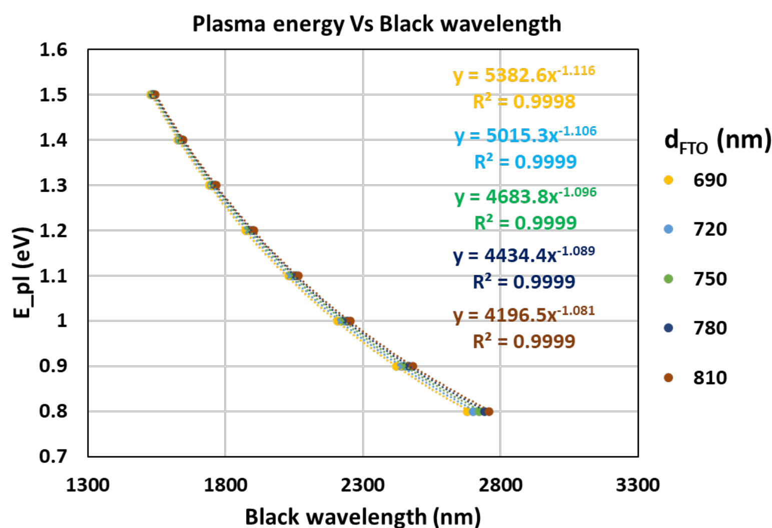

Figure 3.9: The relation between plasma energy and black wavelength for different thicknesses at an E_d of 0.15 eV

(b) The next step was to plot the obtained data points (λ_B) in the x-axis against the plasma energy in the y-axis, for different thicknesses (on the right hand side of the graph as legends), as depicted in figure 3.9. The relations between them were then obtained by fitting a trend-line in Excel. As can be observed from the graph, the relations thus obtained were of power form with excellent fitting where the plasma energy was inversely related to the black wavelength. The empirical equations thus obtained from the fitting along with their R-squared scores, for different thicknesses, are also shown in the graph.

(c) For further observing the dependency of thickness on the plasma energy, the coefficients of these obtained relations were plotted against the different thicknesses, as depicted in figure 3.10a and 3.10b. Here "a" corresponds to coefficient of x in the equation and "b" corresponds to the power of x, considering the equation to be of the form, $y = ax^b$. As can be seen from figure 3.10, the coefficients, a and b, varied logarithmically with the thickness of FTO deposited. It can also be observed from these graphs that while "a" decreases in a logarithmic trend, "b" increases with increasing thickness. This suggests that as the layer becomes thicker, the inverse relation between the plasma energy and black wavelength becomes stronger. The obtained empirical relations were then substituted and combined

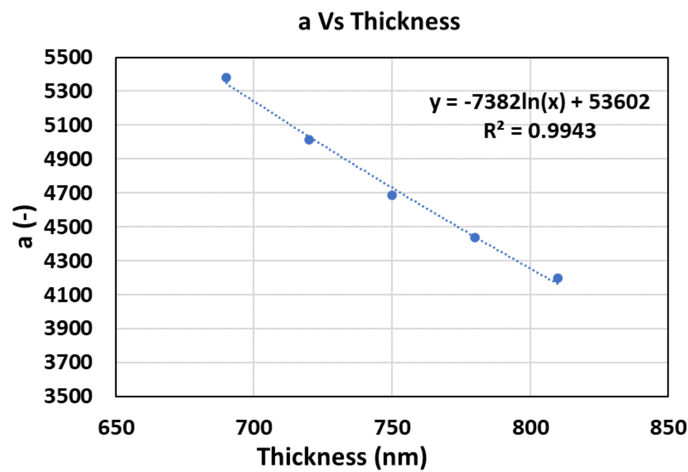

(a) The relation between parameter "a" and thickness of FTO

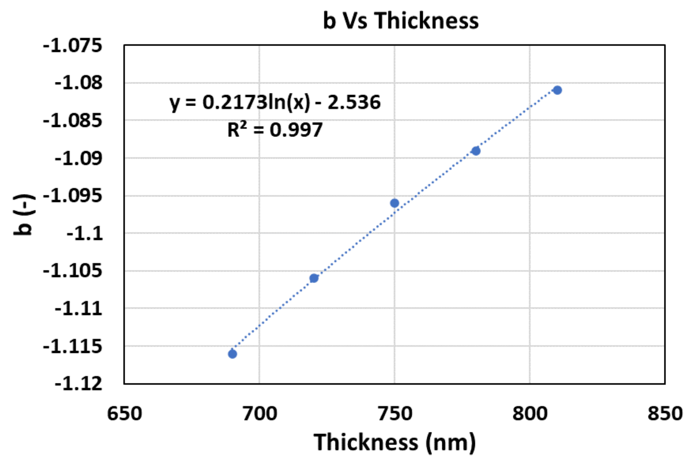

(b) The relation between parameter "b" and thickness of FTO

Figure 3.10: The relationship between the parameters of the obtained power equation and thickness of FTO

to form one relation between plasma energy, black wavelength and the thickness of FTO deposited. This method was repeated for the range of E_d values as specified above. The obtained relation is given by,

$$E_{pl} = (-7370.145\ln(d_{FTO}) + 53567.14) \cdot (\lambda_B)^{0.219\ln(d_{FTO}) - 2.549} \tag{3.30}$$

Note: *The coefficients in the equation 3.30 were generated by factoring in the variations in black wavelength positions with varying damping energies, which showed no significant variation, as evident from figure 3.11. Therefore, an averaging was done for all the coefficients obtained for the range of E_d's. Then the sum of squared errors between measured (E_{pl} values used to obtain the black wavelength) and calculated values (E_{pl} values obtained using equation 3.30) were minimized holding the averaged coefficients as binding parameters of the minimization problem. This minimization was done using the* ***XLAM Solver*** *in Excel. The resulting error margin between the measured and calculated values from the optimization was less than 2 percent.*

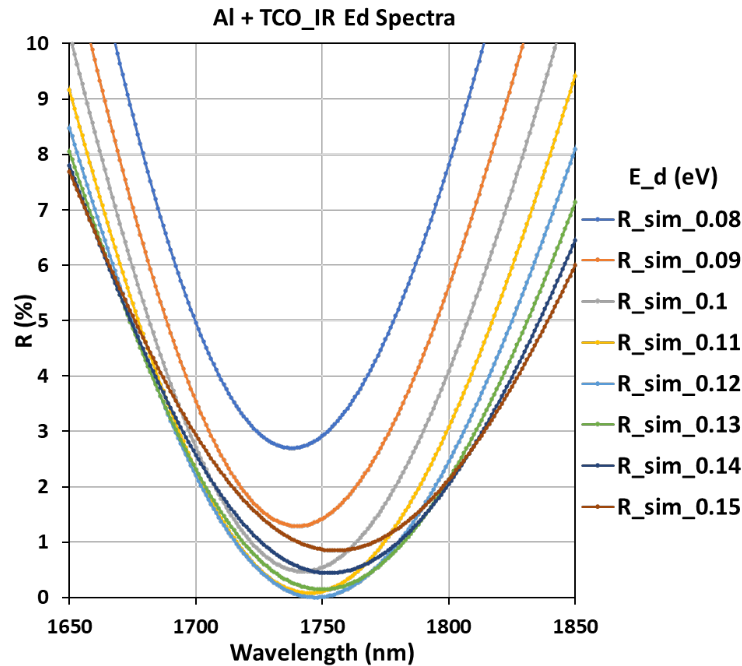

Figure 3.11: Positions of black wavelength with varying damping energies, showing a maximum of 10 nm shift with 50% increase in E_d

After obtaining the relation for plasma energy in terms of black wavelength and thickness of FTO, the next target was to obtain a similar type of empirical relation for the "Slope" of the NIR spectrum between the Drude parameters and thickness. The steps followed for this analysis were similar to that of the black wavelength analysis and are described as follows:

(a) As in the first part of analysis, the first step here also was to determine and record the slope values at different values of damping energies, thickness of FTO deposited, and plasma energies. The data were recorded in a similar way of contour table, as presented in figure 3.12. However, here we varied the damping energy in the vertical axis of the table instead of plasma energy. This was done because the objective of this analysis was to obtain a similar relation as of equation 3.30, for damping energy. The range of variation was kept the same as mentioned previously.

The "slope" of the increasing part of the spectrum after the minima, was determined by mathematically extracting the most linear part of the curve in the region of interest, also referred to as the inflection point method. For this purpose, the wavelength (λ) and its corresponding simulated reflection (R) ranges were considered from when the "black wavelength" occurred till the end of the spectrum (3000 nm). Then the first derivative, $\frac{dR}{d\lambda}$, was calculated, subsequently from which its second derivative, $\frac{d^2R}{d\lambda^2}$, was calculated . Now, as it was observed that the second derivative changed its sign from positive to negative through the zero point, taking the closest value to zero may result in a scenario where Excel finds the minimum

		Slope contour (in nm^-1) with E_pl as 0.8 eV				
		d_TCO (nm)				
		690	720	750	780	810
	0.08	0.0611	0.0634	0.0655	0.0676	0.0695
	0.09	0.0595	0.0614	0.0631	0.0647	0.0661
	0.1	0.0575	0.0590	0.0603	0.0615	0.0626
E_d (eV)	0.11	0.0553	0.0564	0.0573	0.0582	0.0589
	0.12	0.0529	0.0536	0.0543	0.0549	0.0553
	0.13	0.0504	0.0509	0.0513	0.0516	0.0518
	0.14	0.0479	0.0481	0.0483	0.0484	0.0484
	0.15	0.0454	0.0454	0.0454	0.0453	0.0452

Figure 3.12: The slope values as recorded for different variations of damping energy and thickness at 0.8 eV of plasma energy

negative value (which is far away from the zero crossing). Therefore, to prevent this, the squares of the double derivative values were taken. Then the index was matched such that the function gave the value of the wavelength point where the square of second derivative was the minimum. After extracting this data point, five points above and below that corresponding wavelength were considered along with their reflection values, from which the "slope" was then computed. This whole process was then automated for every setting by converting them into a macro in Excel.

(b) The next step was to plot the recorded slopes against the damping energy in the y-axis, for different thicknesses as depicted in figure 3.13. The relations between them were then obtained by fitting a trend-line in Excel. As can be visualized from the graph, the relation thus obtained was of the linear form where the damping energy was linearly related to the slope. This analysis was done for the different values of plasma energies, starting from 0.8 eV to 1.5 eV. The linear equations along with their R-squared score, for different thicknesses, are also presented in the graph.

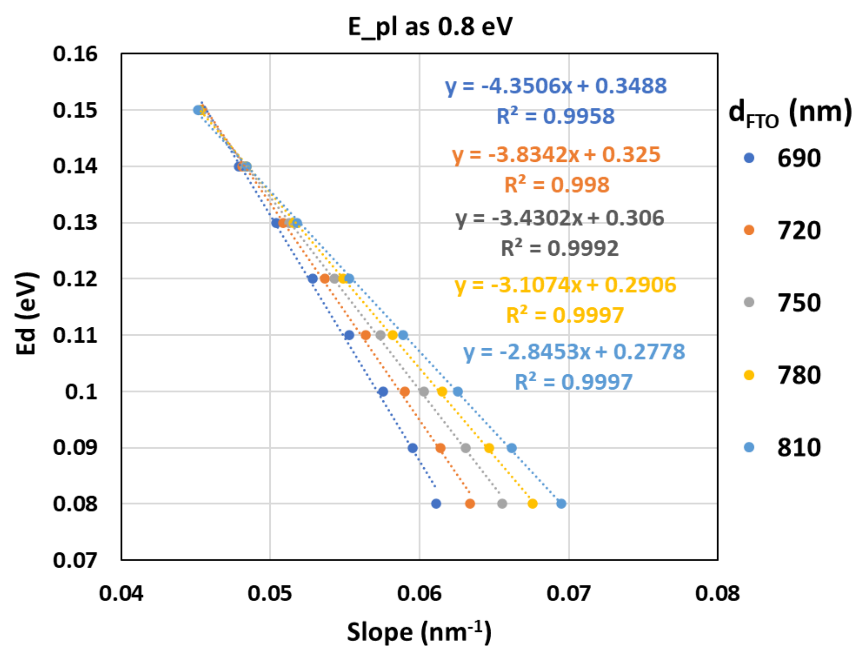

Figure 3.13: The relation between damping energy and slope for different thicknesses at an E_{pl} of 0.8 eV

(c) To further observe the relation between the thickness of FTO deposited and the damping energy, the coefficients of the linear equations, as obtained from the relation of E_d and slope,

were plotted against the thickness. From figure 3.14a it can be seen that the coefficient of slope (*a'*) is logarithmically related to thickness, while in figure 3.14b it can be observed that the intercept of the equation (*b'*) is inversely related with thickness (power form), for different plasma energies.

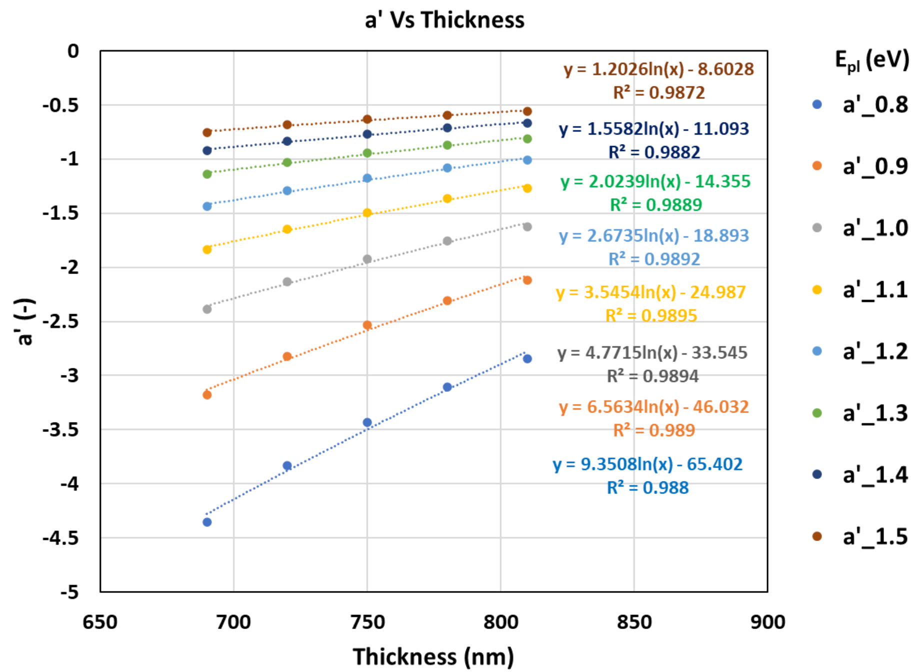

(a) The relation between a' and thickness for different E_{pl}'s

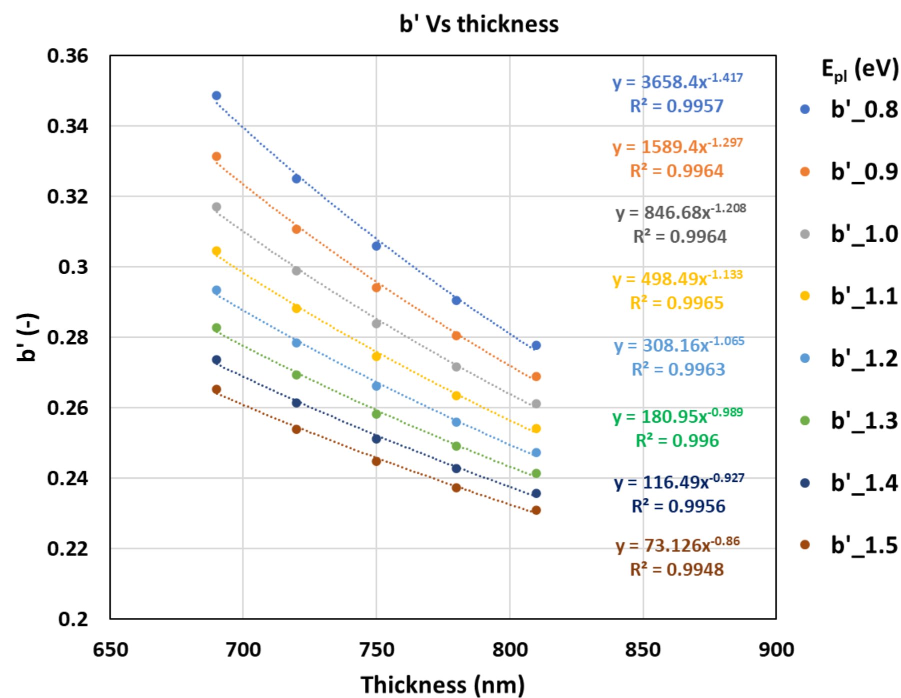

(b) The relation between b' and thickness for different E_{pl}'s

Figure 3.14: The relation between slope, E_d and thickness of FTO deposited

(d) From steps (b) and (c) we were able to obtain a relation between damping energy, slope and thickness of FTO deposited. However, when this analysis was done for the different plasma energies, it was also observed that the coefficients of the relations obtained in figures 3.14a and 3.14b also had some dependency on the plasma energy. Therefore, to further investigate this effect, these coefficients from the relations obtained were tabulated and plotted against the plasma energies. Figure 3.16 presents the relations between the said coefficients (b1 to b4) and plasma energy. Here, b1 and b2 arise from the logarithmic relation of a' with thickness while b3 and b4 are the coefficients of the inverse relation obtained of b' with thickness, from figures 3.14a and 3.14b respectively. From the graphs it can be observed that while the first three coefficients, b_1, b_2, and b_3 vary inversely with plasma energy, the parameter b_4 has a logarithmically increasing variation.

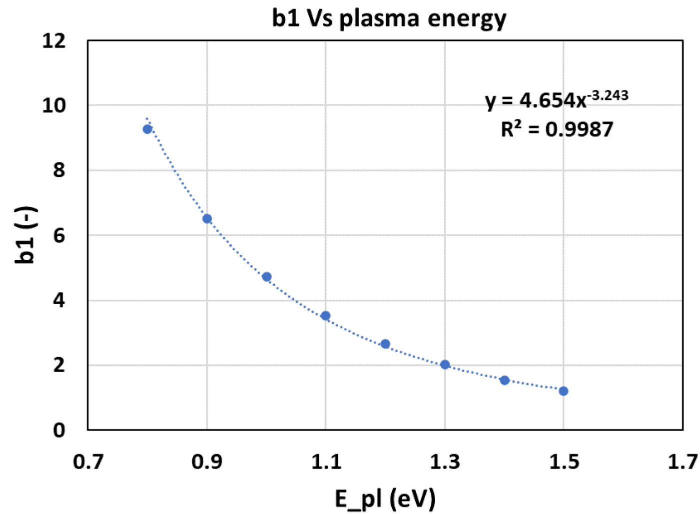

(a) The relation of b_1 with E_{pl}

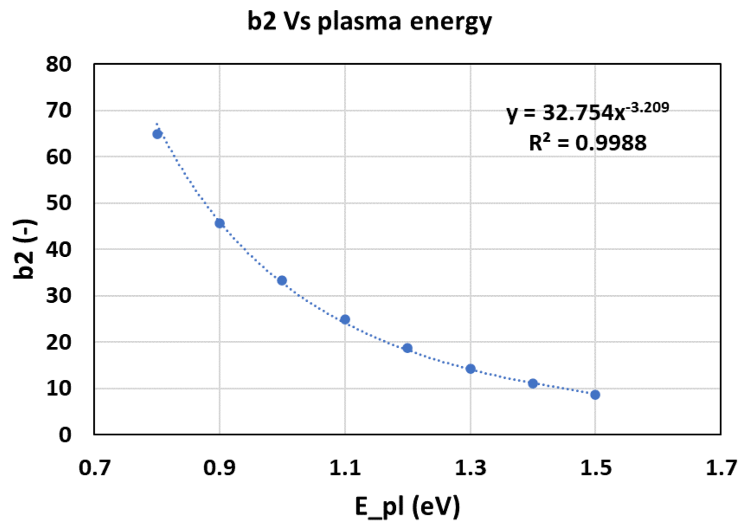

(b) The relation of b_2 with E_{pl}

Figure 3.15: The dependency of first set of coefficients (b_1 & b_2) on the plasma energy

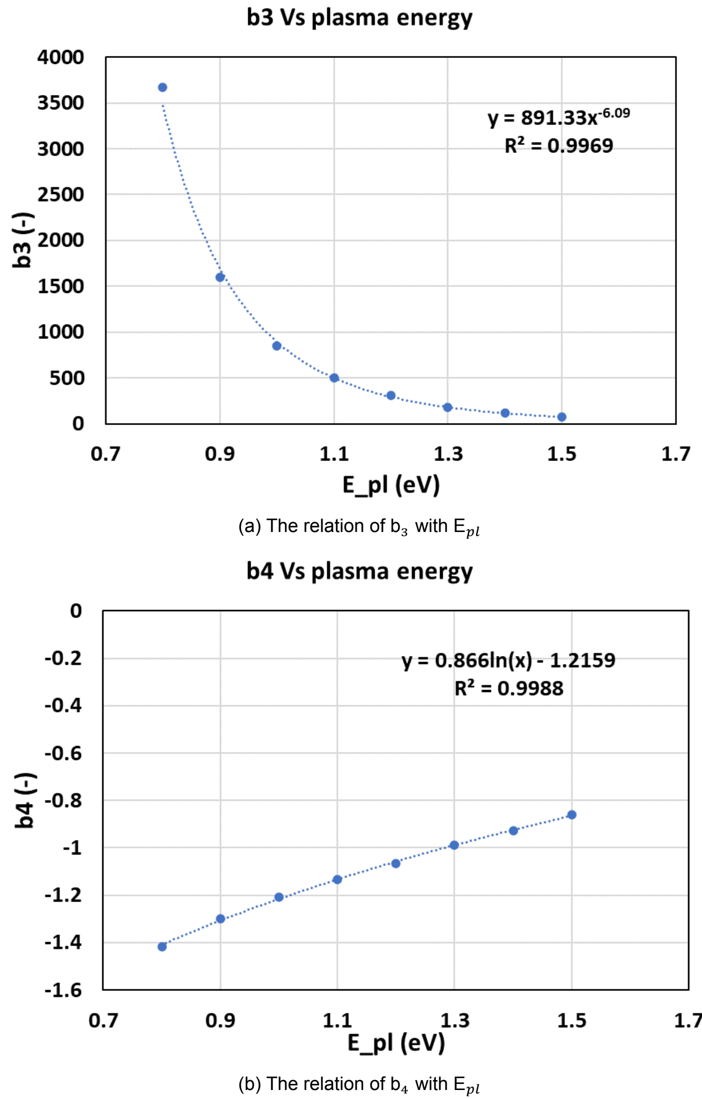

(a) The relation of b_3 with E_{pl}

(b) The relation of b_4 with E_{pl}

Figure 3.16: The dependency of second set of coefficients (b_3 & b_4) on the plasma energy

Using these compounded relations between the different parameters, the relation of damping energy with slope, thickness and plasma energy can be written as,

$$E_d = [(4.654(E_{pl})^{-3.243})\ln(d_{FTO}) - 32.754(E_{pl})^{-3.209}] \cdot Slope + \frac{891.33E_{pl}^{-6.09}}{(d_{FTO})^{-0.866\ln(E_{pl})+1.2159}} \tag{3.31}$$

Note: *The coefficients for this equation are generated by the same methodology as mentioned earlier in the "black wavelength" analysis part. The only difference here being that the variations of coefficients were considered for plasma energy instead of damping energy. The error resulting from the optimization (minimization of squared sum of errors) was within 4.5 percent.*

3. **Conversion into electrical parameters, *N* and μ:** Now that the relations between the Drude parameters and the extracted parameters of interest have been established, these equations of plasma energy (equation 3.30) and damping energy (equation 3.31) can be substituted in equations 3.18 and 3.19, to obtain the charge carrier concentration and mobility respectively.
Note: *The effective mass (m_{eff}) of electron inside the FTO layer is considered to be **28%** of the mass of electron. This value was obtained during a research study at HyET Solar [24].*

Validation of the Model

To validate that the equations which were modelled for predicting the charge carrier concentration (N) and mobility of the electrons (μ) gave sensible results, i.e., in terms of the expected range of values that are normally obtained for the deposited FTO samples at HyET, a sanity check was done. Another purpose of this test was to get an idea of the errors that might occur in the prediction of "N" and "μ" as compared to the simulated values.

For this purpose, two sets (Set A & Set C) of samples of aluminum with FTO were taken. The reflectance spectrum of these sample sets were measured using the UV-VIS-NIR spectrophotometer at HyET. Each of these sets consisted of ten samples, where one particular variant had two sub-samples at two different positions of the module. Their positions are defined by a parameter known as "Center of Module (COM)", which implies the distance of the point from the actual center of the module. For example, a sample at CoM 115 means that the position of that sample is 115 cm away from the center. Out of these 10 samples, 6 were un-treated (there was no sort of treatment done on the aluminum substrate prior to FTO deposition) (S1.3, S1.4 and S1.5) and 4 pre-treated (acid and base treatment were done on the aluminum roll before depositing FTO) (S2.3 and S2.4). Table 3.2 summarizes the results of the tests done on Set A samples and table 3.3 presents the results summary of the validation done on Set C. To explain the columns of the tables, starting from left to right are as follows:

- *Sample:* Indicates the name of the sample of which validation test was carried out.
- *CoM:* Indicates the position of the sample from the center of the module.
- N_M*:* Represents the values of charge carrier concentration as obtained using the equations 3.30 and 3.18 from the measured reflection spectra of the sample.
- N_S*:* Represents the values of charge carrier concentration obtained from the simulated curve. These values are obtained by substituting the obtained plasma (3.30) and damping energies (3.31), for the respective thickness, directly in the Excel model developed by E. Hamers [24].
- μ_M*:* Represents the values of mobility as obtained using the equations 3.31 and 3.19 from the measured reflection spectra of the sample.
- μ_S*:* Represents the values of mobility obtained from the simulated curve similarly as for obtaining n_S, from the Excel model [24].
- *Err(N):* Shows the percentage of error associated with the estimation of measured "n" with respect to the simulated "n".
- *Err(μ):* Shows the percentage of error associated with the estimation of measured "μ" with respect to the simulated "μ".

Table 3.2: The results and comparison for Set A samples with their error percentages

Sample	CoM	N_M (10^{20} cm^{-3})	N_S (10^{20} cm^{-3})	μ_M (cm^2/V· s)	μ_S (cm^2/V· s)	Err(N) (%)	Err(μ) (%)
S1.3	115	3.809	3.733	23.96	25.35	2.00	5.81
S1.4	115	3.813	3.798	27.73	28.35	0.40	2.24
S1.5	115	3.780	3.683	25.64	27.00	1.28	5.26
S1.3	255	3.798	3.728	24.87	26.04	1.86	4.71
S1.4	255	3.808	3.783	26.51	27.43	0.66	3.46
S1.5	255	3.829	3.779	25.10	26.62	1.30	6.06
S2.3	115	3.964	3.872	25.13	26.23	2.32	4.38
S2.4	115	3.926	3.873	24.48	25.84	1.34	5.55
S2.3	255	3.888	3.793	24.73	25.90	2.43	4.70
S2.4	255	3.894	3.867	27.94	28.46	0.67	1.87

The resulting error percentages were then converted into a box and whisker plot to have a clearer picture of the average error in prediction of "N" and "μ". Figure 3.17 depicts such plot for the samples of Set A. It can be observed from this graph that the average error resulting in prediction of the charge carrier concentration is about 1.4%, while the average error in prediction of mobility is about 4.4%. The

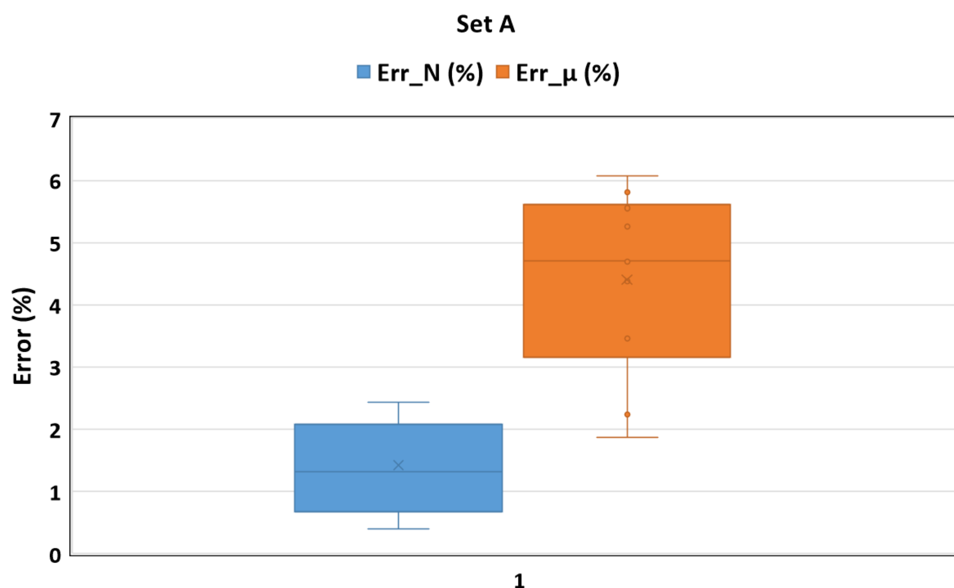

Figure 3.17: The errors (in %) of prediction for "N" (in blue) and "μ" (in orange) in Set A samples

Table 3.3: The results and comparison for Set C samples with their error percentages

Sample	CoM	N_M (10^{20} cm^{-3})	N_S (10^{20} cm^{-3})	μ_M (cm^2/V· s)	μ_S (cm^2/V· s)	Err(N) (%)	Err(μ) (%)
S1.3	115	3.871	3.799	23.97	25.37	1.88	5.84
S1.4	115	3.901	3.864	24.20	25.74	0.93	6.37
S1.5	115	3.884	3.839	25.52	26.92	1.17	5.47
S1.3	255	3.830	3.778	27.00	27.69	1.34	2.58
S1.4	255	3.818	3.788	25.61	26.74	0.79	4.44
S1.5	255	3.799	3.750	25.07	26.60	1.29	6.13
S2.3	115	3.932	3.825	23.78	25.20	2.71	5.98
S2.4	115	3.963	3.920	25.42	26.53	1.08	4.38
S2.3	255	3.872	3.783	25.45	26.45	2.30	3.91
S2.4	255	3.963	3.920	25.55	26.63	1.08	4.24

spread in error percent is also lower for "N" as compared to "μ". Similarly, for the samples of Set C, an error plot of the resulting error percentages was made, as depicted in figure 3.18. Similar to the results of Set A, it can be observed here that the average error percent in prediction of "N" stays about 1.4%, while the error in prediction of mobility is higher hovering at about 4.9%.
In conclusion from the validation tests performed, it can be inferred (from tables 3.2 and 3.3 & figures 3.17 and 3.18) that :

1. Overall, the errors in prediction of charge carrier concentration and mobility stay within a nominal value of 5%.

2. The measured values for charge carrier concentration are slightly over-estimated as compared to simulated values, while the measured values for mobilities are under-estimated in comparison to simulated ones. One of the reasons could be that the empirical coefficients which were determined, were based on thickness (of FTO) values which were different from the thicknesses of these set of samples.

3. The prediction of mobility from this empirical model showed higher errors as opposed to the estimation of charge carrier concentration. This was the case majorly because of presence of noise in the measured data (reflectance spectrum of the samples) which further affected the prediction of slopes of the NIR spectrum (as the measured slope values relate with damping energy which

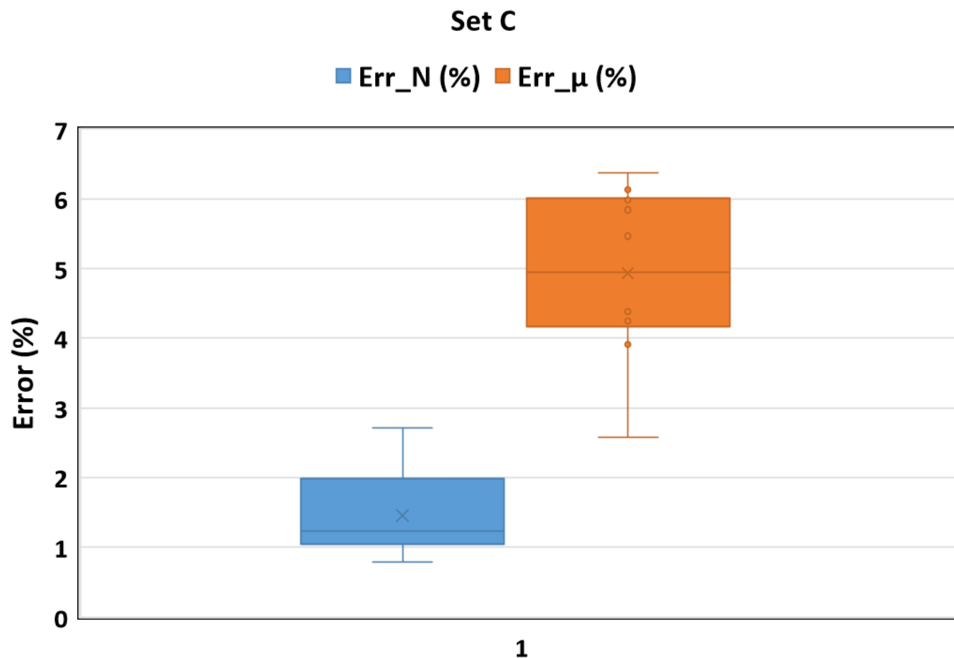

Figure 3.18: The errors (in %) of prediction for "N" (in blue) and "μ" (in orange) for Set C samples

is further associated with calculation of mobility). This was one of the contributing reasons which led towards the rejection of Model A, as will be discussed in the following subsection.

Limitations of the Model

Although the model was able to predict the values of charge carrier concentration and mobility with acceptable margins of error, there were some flaws that were observed when it was tested against some more criteria. The limitations that this model posed, which did not lead to the implementation of the derived equations, are listed as follows:

- There was a substantial inaccuracy in determining the "Slope" from the measured reflection spectrum, as observed in the previous section, due to the presence of some amount of noise in the spectrum, which is not observed while modelling a relation via simulated data.

- Because of the presence of this noise, the inflection point method, which was utilised to generate the "Slope" values for different settings of E_{pl}, E_d and d_{FTO} from the simulated spectrum, did not result in the prediction of the correct wavelength point around which the slope was to be calculated.

- This approach was built on the basis that the position of the "black wavelength" is independent of the thickness of the FTO being deposited and that it can solely be utilised to determine the electrical properties of the material under evaluation, as deduced from the conclusions of the model developed by Edward Hamers [24]. However, here while developing this model, it was observed that indeed the position of black wavelength has some dependency on thickness (equation 3.30) and therefore cannot be used as a direct measure of the electrical properties of the layer. This conclusion rendered the utilisation of the parameter as a quality control criterion redundant. Although this was easy to extract and quantify further in terms of plasma energy, it would not give complete information about the quality of the layer deposited, electrically.

- The constants in the equations that were derived empirically failed to provide a physical meaning that could be used to classify the material properties.

- The analysis that was done considered certain fixed values of the Lorentz oscillator (baseline values), and was developed by only varying the Drude parameters at these values. This implies

that if the parameters from Tauc-Lorentz model were varied, the coefficients as determined in the modelled equations would change heavily and thereby affecting the measurements.

3.3.2. Model B: Drude Model Fitting

Owing to the limitations and flaws found in Model A, as discussed in the previous section, an alternative approach on determining the electrical properties of the FTO from the NIR reflection spectrum was devised. As observed in the previous model, due to the consideration of the Tauc-Lorentz parameters at one particular set of values, reliable results could not be defined for broader ranges of thicknesses of the layer. This was majorly because the refractive indices of FTO were dependent upon the Lorentz dielectric function as well, according to equations 3.26, 3.27, 3.28 and 3.29. As the electrical properties,"N" and "μ, were directly related to only the Drude model parameters, in this approach it was chosen not to consider any effect of the Tauc-Lorentz permittivity [25]. Even though in the development of the first model, there was no variation of the Lorentz energy values, their effect on the entire reflectance spectrum could not be neglected. This was one of the major lessons learnt from the failure of model A. The lesson learnt thus supported the consideration of only the dielectric permittivity of the Drude model, neglecting the Tauc-Lorentz part, for modelling the NIR spectrum. The new model thus developed now involved only the characteristic material properties in the infrared region only. The methodology followed to achieve desired electrical parameters are described as follows:

1. **Obtaining the simulated reflection coefficients:** The primary objective of this approach, as mentioned, was to obtain the dielectric permittivity of the deposited FTO only from the Drude theory, which can then be converted into the refractive indices of the material. For this purpose, first the equation concerning the dielectric permittivity of the Drude model was considered. Rewriting the equation, we have,

$$\varepsilon_{Drude} = 1 - \frac{E_{pl}^2}{E_{ph}^2 + E_d^2}[1 - j\frac{E_d}{E_{ph}}] \tag{3.32}$$

Now, for obtaining the permittivity, three parameters were required, namely the photon energy, plasma energy and the damping energy. The photon energy was obtained using the equation 3.13 for the entire wavelength spectrum, from 200-2500 nm. The plasma and the damping energies were assigned the "Baseline" values of 1.3 eV and 0.15 eV respectively from 3.1. After obtaining the real and imaginary parts of the Drude permittivity, the next step was to calculate the ε_1 and ε_2 from the obtained Drude and permittivity. This is one of the important steps in this model, which differentiates it from the previous model, where ε_1 and ε_2 were obtained using both the Lorentz and Drude permittivities. In this model, these two permittivities are given by,

$$\varepsilon_1 = \varepsilon_\infty + Re(\varepsilon_{Drude}) \tag{3.33}$$

$$\varepsilon_2 = Im(\varepsilon_{Drude}) \tag{3.34}$$

where ε_∞ is the relative permittivity at infinite energies. This is the value of the dielectric permittivity from the Tauc-Lorentz (TL) model in the near-infrared part of the electromagnetic spectrum. This parameter is used in the equation as an additional fitting parameter to prevent ε_1 from converging to zero at energies below the energy bandgap (generally this parameter has a value > 1) and thus to obtain a good fit of the simulated and the measured data [29]. This value is initially set at an arbitrary value of 3. From the obtained permittvities, the refractive indices of the material (*n+ik*) are calculated using the equations 3.28 and 3.29. After the 'n' and 'k' values for the FTO are obtained, the reflection coefficients at full spectrum of the wavelength are then calculated using the Fresnel coefficients for reflection at normal incidence ([30]), which is given by,

$$R = \frac{(n_0 - n)^2 + k^2}{(n_0 + n)^2 + k^2} \tag{3.35}$$

where n_0 is the refractive index of the medium from where the light is incident and *n+jk* is the complex refractive index of the substrate material. Here, as the light is incident from the air, n_0 is equal to 1. Therefore, the Fresnel equation for reflection now becomes,

$$R = \frac{(1 - n)^2 + k^2}{(1 + n)^2 + k^2} \tag{3.36}$$

From which the wavelength dependent simulated reflection coefficients are obtained.

2. **Fitting procedure:** After the simulated reflection coefficients are obtained, this reflection versus the wavelength curve was to be fitted with the measured reflectance spectra of the aluminum with FTO stack. Therefore, a reference sample of aluminum with FTO was taken and its reflectance values were obtained using the spectrophotometer at HyET, from 200-2500 nm. These measured reflectance values were then compared against the obtained simulated reflectance values and the squared errors at each wavelength were tabulated. From this, the sum of all the squared errors was calculated. Using the XLAM solver in Excel, the objective function was set to minimize the sum of squared errors by considering the fitting parameters, E_{pl}, E_d and ε_∞. Figure 3.19 depicts the fitting of the modelled reflection coefficients and the measured values after the minimization step.

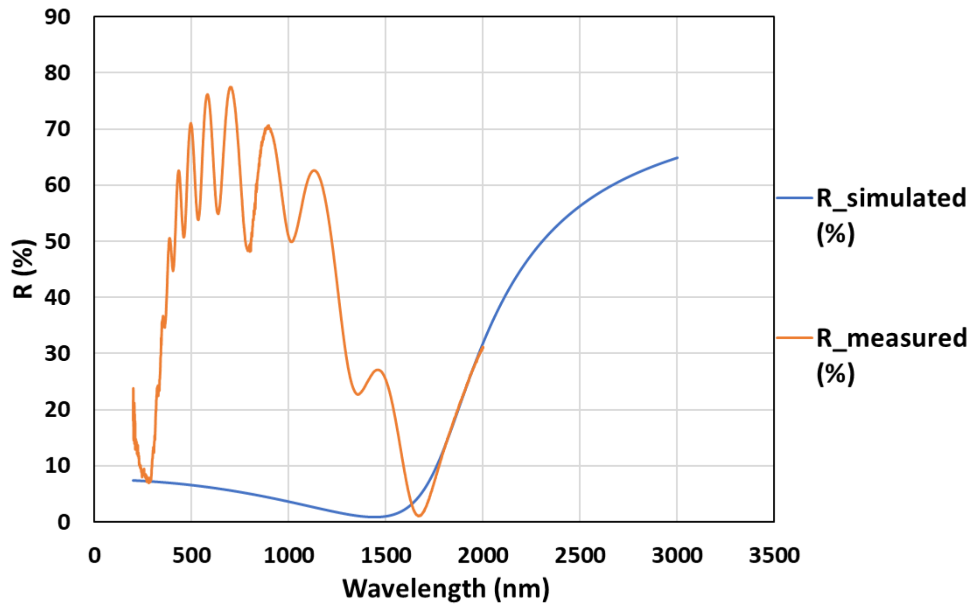

Figure 3.19: Result of the fitting done for the simulated (blue) and the measured (orange) reflectance (R) values

It can be observed that the fitting between the measured and simulated values from about 1700-2000 nm is completely matching. The fit in this range of wavelength was achieved by implementing a certain fitting routine, that is, for the lower limit of the range. This lower bound of the fit was decided after following a certain methodology, which is described in detail in the next point.

3. **Deduction of the lower bound of fitting:** The motivation behind this analysis was the research question: “What is the wavelength of incident light at which the FTO is no more sensitive to the substrate beneath it (aluminum)?” Initially, the fitting was done from the ”black wavelength” position until the end of spectral range of interest (2500 nm). However, it was foreseen that there might be some amount of light which is still reflecting from the aluminum/FTO interface and reaching back to the surface of the FTO layer, even at and some wavelengths beyond the position of black wavelength. This might lead to unreliable measurements of the parameters, as it was desired to obtain purely the properties of the deposited layer. The first step towards the analysis was to determine the absorption coefficient of the FTO layer, which was done by using the complex part of the refractive indices obtained from the equation 3.29. The relation between the absorption coefficient (α) (in cm^{-1}) and k is given by,

$$\alpha = \frac{4\pi k}{\lambda} \tag{3.37}$$

where λ is the wavelength (in nm) of the incoming photon. Then using the obtained α, the percentage of reflected light coming from the aluminum/FTO interface back to the top surface of the FTO was calculated using the Lambert’s law. The exponential of the law was modified according to the equation 3.38, which accounted for the two passes of the light, first pass which occurs at

the air/FTO interface and the second occurring at the FTO/aluminum interface, as illustrated in figure 3.20.

$$I = I_0 e^{-2\alpha d} \implies \frac{I}{I_0} = e^{-2\alpha d} \tag{3.38}$$

where I_0 is the intensity of incoming light and *d* is the thickness of the FTO layer. Using this equation, we were able to obtain information about how much of light is being absorbed by the top surface of the FTO due to the reflected light coming back from the interface. For the purpose

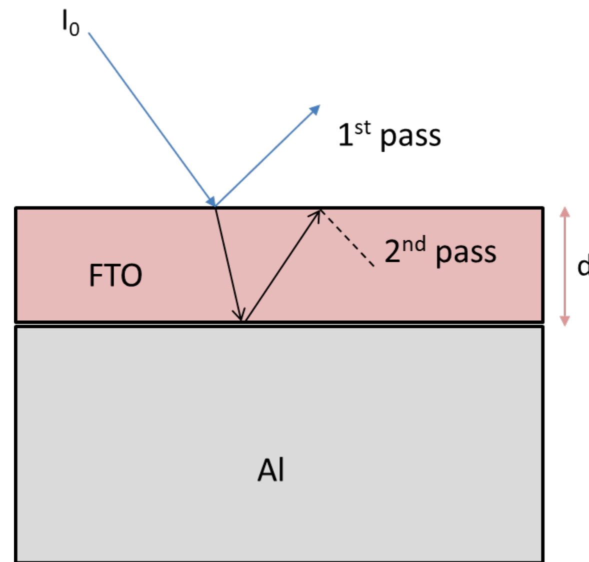

Figure 3.20: Incident light on the FTO and its reflection from the Aluminum/FTO interface

of finding this point in the reflection spectrum, thickness of the measured sample was considered from the previous measurements done. The exponential term in the equation 3.38 thus acts as a correction factor for deducing the initial point of wavelength from where the effect of substrate reflected light is not significant enough. This method was followed for the samples as taken in Set A, in the previous section, and this correction factor was calculated at their ”black wavelength” positions. The results of this analysis are presented in table 3.4.

Table 3.4: The results of analysis for Set A samples

Sample	CoM	d_{FTO} (nm)	λ_B (nm)	$e^{-2\alpha d}$
S1.3	115	704	1641	0.042
S1.4	115	744	1649	0.036
S1.5	115	789	1655	0.028
S1.3	255	704	1649	0.039
S1.4	255	744	1665	0.031
S1.5	255	789	1672	0.022
S2.3	115	687	1621	0.026
S2.4	115	719	1630	0.028
S2.3	255	687	1632	0.029
S2.4	255	719	1630	0.031

From the analysis performed, it can be observed that even at the ”black wavelength (λ_B)” position there is still on an average about 3% light (multiplying the correction factor with 100) coming back to the surface of the FTO layer from the aluminum/FTO interface. This amount of light was substantial enough to affect the reliability of the obtained data, as the electrical properties of the layer might be influenced by the properties of the substrate beneath it. Ideally, this reflected light should be absorbed less than one percent in order to not affect the measurements of the

parameters. Therefore, the analysis was extended to find the wavelength position from which the light being absorbed by the top surface was < 1%. Table 3.5 summarizes the wavelength positions at which the absorbed light from the reflection was just below the required value.

Table 3.5: The results of wavelength positions for Set A samples at which absorption of light was < 1%

Sample	CoM	d_{FTO} (nm)	λ_B (nm)	Req. $e^{-2\alpha d}$	Occurs at λ (nm)	Difference (nm)
S1.3	115	704	1641	0.0098	1775	134
S1.4	115	744	1649	0.0099	1759	110
S1.5	115	789	1655	0.0098	1747	92
S1.3	255	704	1649	0.0099	1770	121
S1.4	255	744	1665	0.0098	1764	99
S1.5	255	789	1672	0.0099	1740	68
S2.3	115	687	1621	0.0098	1707	86
S2.4	115	719	1630	0.0099	1721	91
S2.3	255	687	1632	0.0099	1729	97
S2.4	255	719	1630	0.0099	1726	96

From table 3.5, it was inferred that on an average at about 100 nm away from the location of black wavelength, the reflected light coming back from the interface is less than 1%. So, in the model the lower bound of the fitting range was decided to be kept at (location of black wavelength + 100 nm). In conclusion, the fitting range for this model was **[(”Black wavelength” + 100) nm - 2500 nm]**. Figure 3.21 depicts the fit of the measured and the simulated reflection data points after the implementation of this model and the fitting range in the LabVIEW software.

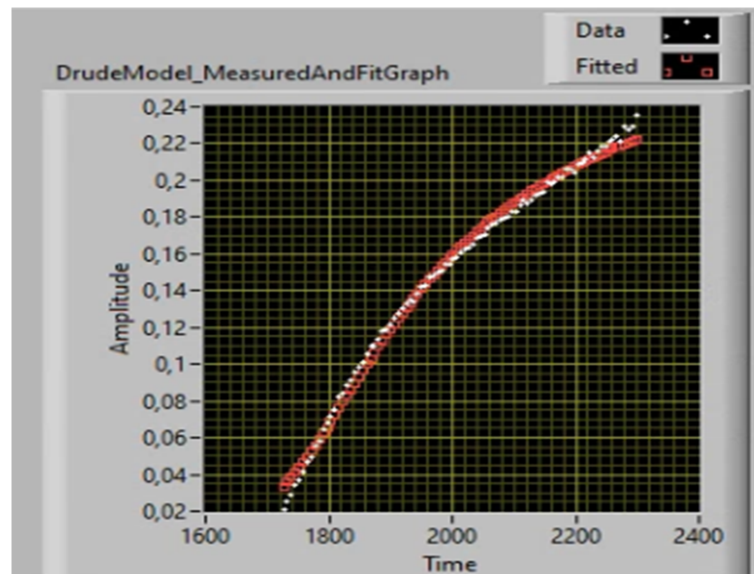

Figure 3.21: Result of the Drude model fitting done for the simulated (red) and the measured (white) reflectance values

In conclusion, the Model B was considered much more suitable than the Model A in terms of:

- Reduced complexity in terms of analysis and the equations used.
- Better accuracy in determination of the plasma and the damping energy as it does not involve ”Slope” calculations, which were very difficult to extract from the measured data, via model A, because of the noise present.
- ”Black wavelength” position was no more a quality criterion directly. It was just used to determine the fitting range of the model.
- Easy integration in the LabVIEW software.

3.4. Results and Discussion

This section presents the results of FTO deposition runs that were done in the APCVD machine at HyET, with the online diagnostics implemented following the models as discussed in the previous section. The models that were integrated in the software were the ”Optical thickness” for the UV-VIS part of the spectrum, and ”Model B: Drude model fitting” for the NIR part of the spectrum. The first sub-section presents the measurement setup employed in-line in the machine to obtain the opto-electrical parameters of the deposited FTO layer on aluminum substrate, briefly. The final sub-section discusses the results from the data obtained from this setup.

3.4.1. Measurement setup

After the FTO is deposited on the aluminum substrate, it passes under the roller beneath which the reflectance probes are mounted on a rail mounting system. The mounting system is designed such that the probe, from which the light is being generated, stays perpendicular to the incoming foil. This is a very crucial parameter, as, if the angle of incidence of light is even slightly more or less than 90°, it would heavily affect the reflectance measurements which further leads to the inaccuracy in obtaining the data. The light source for the reflection probes are the two spectrometers (UV-VIS and NIR) which are connected from end to end via an optical fiber which transports light from the spectrometers end to the probe. The reflectance spectrum is then generated according to the method as mentioned in the previous section. The spectrometers are connected to a PC which records the data and processes them in the software program, to generate thickness, charge carrier concentration and mobility of the FTO layer. Figure 3.22 illustrates the complete measurement setup in 2D view, while figure 3.23 represents a 3D view of the setup.

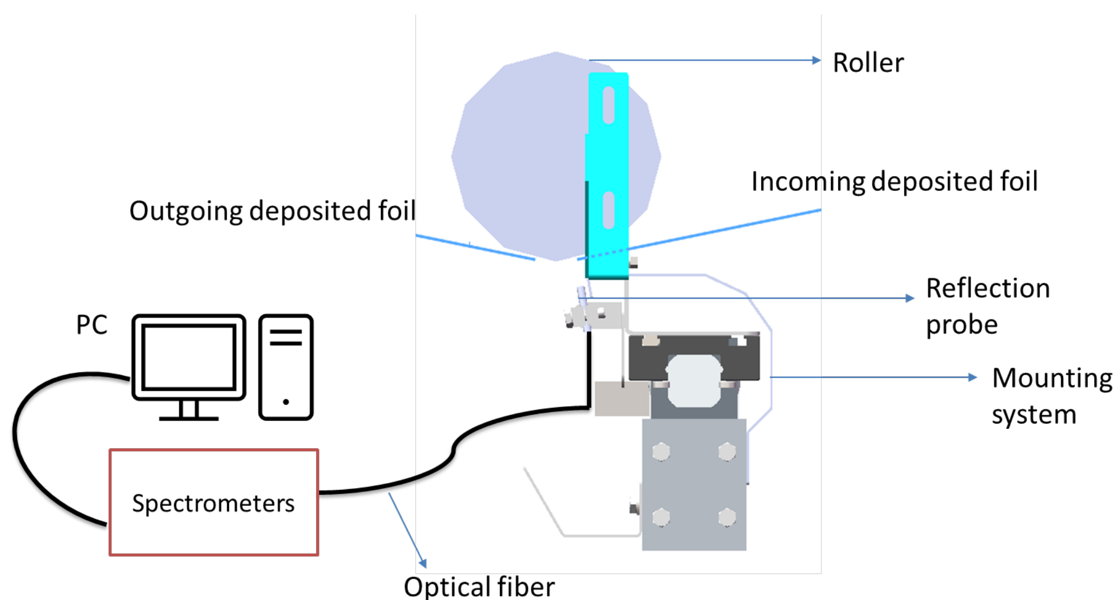

Figure 3.22: The measurement setup in-line at the APCVD machine at HyET

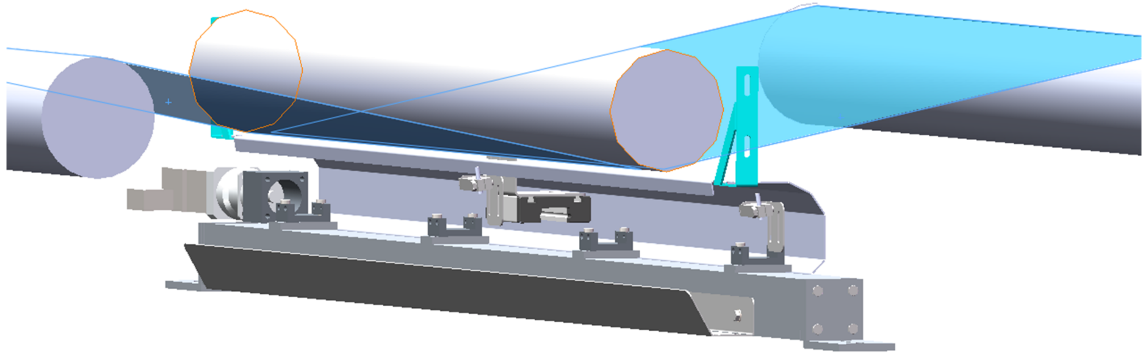

Figure 3.23: A 3D view of the measurement setup

3.4.2. Results from the in-line diagnostics

Before having a glance at the results and understanding them, it is important to define the parameters. As the thickness, charge carrier concentration and mobility values are obtained by probing light of different wavelengths onto the layer, they are henceforth referred to as ”Optical thickness”, ”Optical charge carrier concentration” and ”Optical mobility”. The primary objective of this section is to present these parameters as obtained for a experimental run that was carried out (from the modelled and implemented in-line diagnostics) at HyET. These optically obtained parameters are then compared against the data which are obtained using appropriate measurement setups (Scanning electron microscope for thickness of the FTO layer and Hall effect measurement setup [31] for electrical parameters (N, μ, and R_{sh})), for some of the experimental settings. The results obtained from these measurement setups are henceforth referred to as ”offline” data. To delve deeper into the recipes of all the experimental settings, is beyond the scope of this project. Henceforth, the results presented will only focus on the data obtained in-line and the discussions on their comparison with offline data measured at the Delft University of Technology.

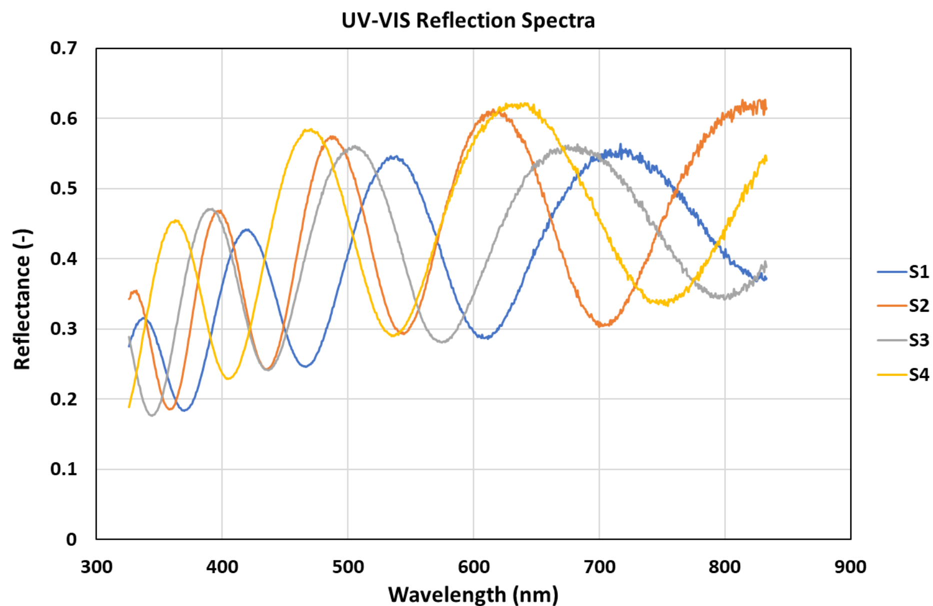

(a) Reflectance spectrum for settings 1 to 4

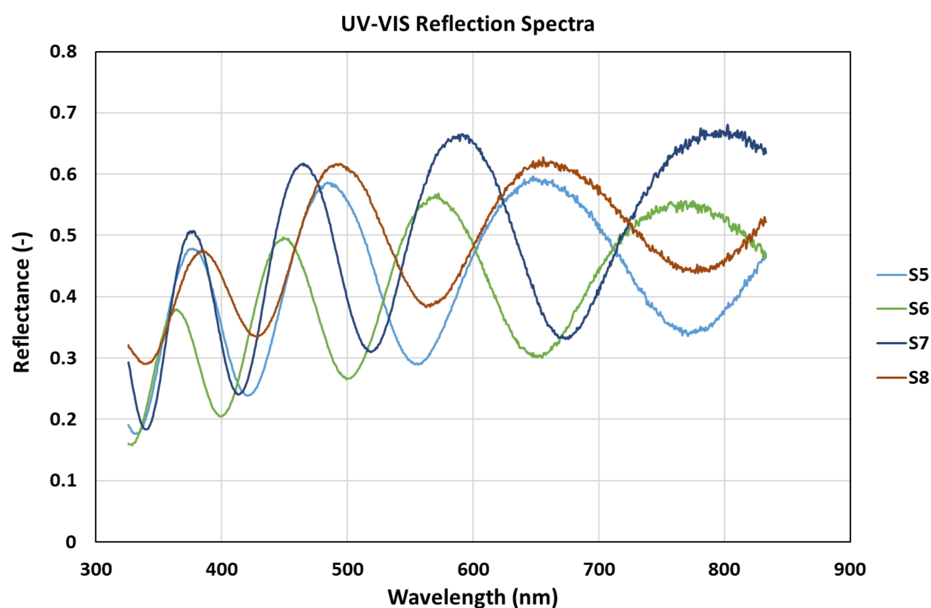

(b) Reflectance spectrum for settings 5 to 8

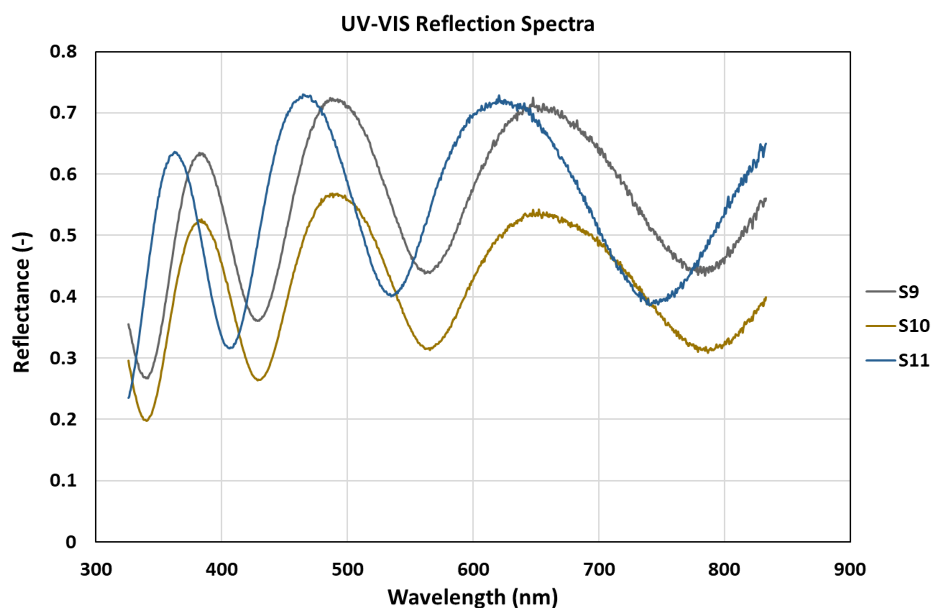

(c) Reflectance spectrum for settings 9 to 11

Figure 3.24: The reflectance spectra of different experimental settings carried out at HyET

To begin with, figure 3.24 presents the reflection spectra as obtained from the UV-VIS spectrometer between the wavelength range of 300-900 nm. Here, 11 different experimental settings were done (S1-S11) in the APCVD machine at HyET with varying deposition conditions. These variations concerned mainly to the gas flows and deposition speeds that was carried out as a part of another Master's thesis project in HyET [32]. For easy visualization of the spectra of these 11 settings, they were segregated into three separate plots where fig 3.24a depicts the spectrum for settings 1-4, fig 3.24b shows the spectrum for settings 5-8 and fig 3.24c presents the spectrum for settings 9-11. These reflectance spectra were then processed according to the "Optical thickness" model in the software program, as described in section 3.2.3, to generate the values of thickness of the FTO layer. The thicknesses of these settings are tabulated in table 3.6. In this table, the mean thickness (d_{FTO}) (in nm) is obtained by taking the average of all the thickness values obtained for the entire duration of the setting at the

Table 3.6: The thicknesses as obtained from the optical thickness model for 11 settings using the reflectance spectra of the aluminum/FTO stack

Sample	Mean d_{FTO} (nm)	Standard deviation (nm)	Error in mean (nm)
S1	694.38	8.04	1.44
S2	825.15	8.03	1.44
S3	713.27	28.42	1.14
S4	612.40	4.52	0.81
S5	630.75	4.41	0.79
S6	776.73	15.73	2.83
S7	778.36	6.71	1.20
S8	659.44	3.14	0.56
S9	635.63	2.71	0.49
S10	613.09	7.41	1.33
S11	565.09	99.26	17.83

center of the module. The error in mean (E) is calculated by the following equation,

$$E = \frac{SD}{\sqrt{N}} \tag{3.39}$$

where, SD is the standard deviation of the mean thickness and *N* is the number of data points in the range.

It can be inferred together from figure 3.24 and table 3.6 that the thickness of the FTO layer depends on the number of maxima and minima resulting in the reflectance spectrum. These maxima and minima occurring in the spectrum can be attributed to the occurrence of interference fringes when the light is incident on the layer. The light is incident perpendicular to the surface of the FTO layer, thus interference occurs if,

$$2n(\lambda_m)d_{FTO} = (m_0 + \frac{m}{2})\lambda_m \tag{3.40}$$

where *m* is the order ($m \epsilon$ N (natural number)), $n(\lambda_m)$ is the wavelength dependent refractive index, λ_m is the wavelength corresponding to the interference condition, and d_{FTO} is the thickness of the layer. If *m* is an even number, there is a constructive interference between the incident light and the material resulting in maximum. While, when *m* is an odd number, there is a destructive interference leading to a minimum in the spectrum. Therefore, by obtaining the number of maxima and minima occurring in the spectrum, a linear relation between the order (m) and $\frac{1}{\lambda_m}$ can be obtained from equation 3.40 as,

$$\frac{m}{2} = \frac{2n(\lambda_m)d_{FTO}}{\lambda_m} - m_0 \tag{3.41}$$

In equation 3.41, if the wavelength dependent refractive index is kept constant or variable with wavelength, the slope of this equation will always depend on the constant refractive index and thickness of the layer whereas the intercept, that is independent of thickness, will vary with $n(\lambda_m)$. Thus, the higher the interference, the higher is the order (m) (number of maxima and minima) and the thicker the layer is [15].

The measurement setup as illustrated in figures 3.22 and 3.23 is also capable of moving across the full width of the roll on which the FTO is deposited. This characteristic of the setup allows to record the thickness measurements across the width of the foil, as the probe traverses from the left-most edge to the right-most edge of the foil. From this measurement, information about the homogeniety in deposition of the FTO layer across the aluminum foil can be inferred. The width of the foil used for this experimental run was 350 mm. Figure 3.25 depicts the thickness of the FTO layer deposited across the width of the foil for the first four settings. The width of the foil is associated with the ”Cart position” on the horizontal axis of the graph. Cart position refers to the location of the cart on which the reflection probe is mounted. It is important to note that the range of movement of the cart is from 850-1250 mm. Here, 850 mm is the left-most position while 1250 mm is the right-most position of the cart. The range of movement is kept 50 mm higher than the width of the foil so as to get an understanding of when the deposition effectively starts. In correspondence with this fact, it can be observed from the graph that

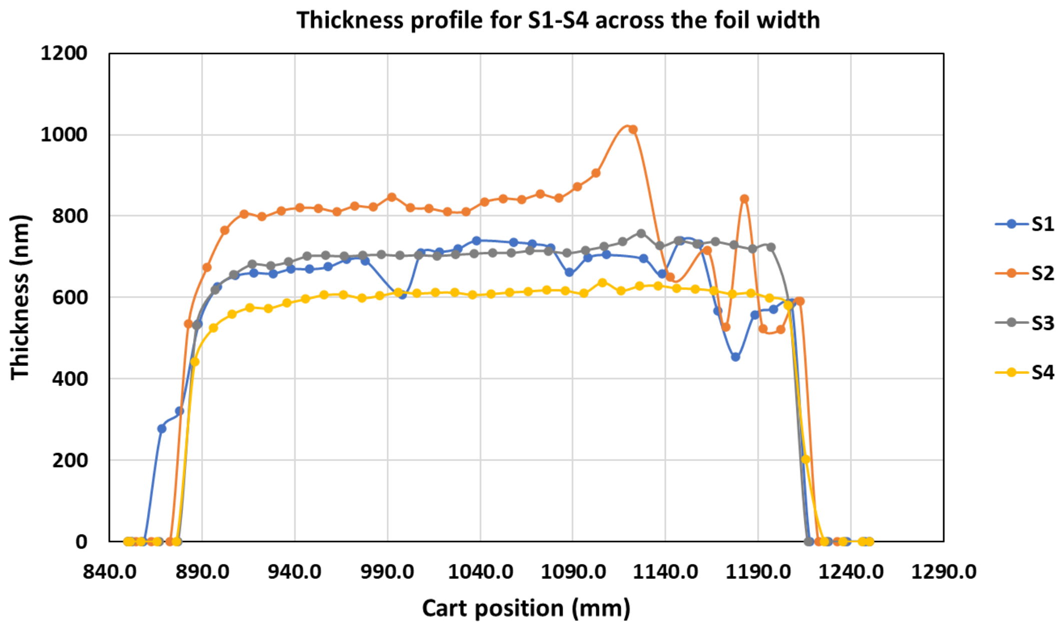

Figure 3.25: The thickness profile across full foil width for settings 1 to 4

the FTO layer begins from around 875 mm till about 1225 mm. It can be inferred from the graph that, while settings 3 & 4 have a fairly homogeneous deposition across the width; settings 1 & 2 on the other hand show non-homogeneous deposition of FTO layer, especially on the right side of the foil.

Similarly, figures 3.26 and 3.27 present the thickness profiles across the width for settings 5 to 8 & 9 to 11, respectively. From figure 3.26 it can be observed that settings 5 & 6 show a homogeneous FTO layer deposition as opposed to the settings 7 & 8 which show small peaks and valleys of deposited thickness across the foil width. Figure 3.27 depicts the non-uniformity in deposition of the FTO layer on the aluminum foil as the thickness profiles show a well-shaped pattern, implying that the thickness first increases from the left edge towards the center and then decreases on the right side of the foil.

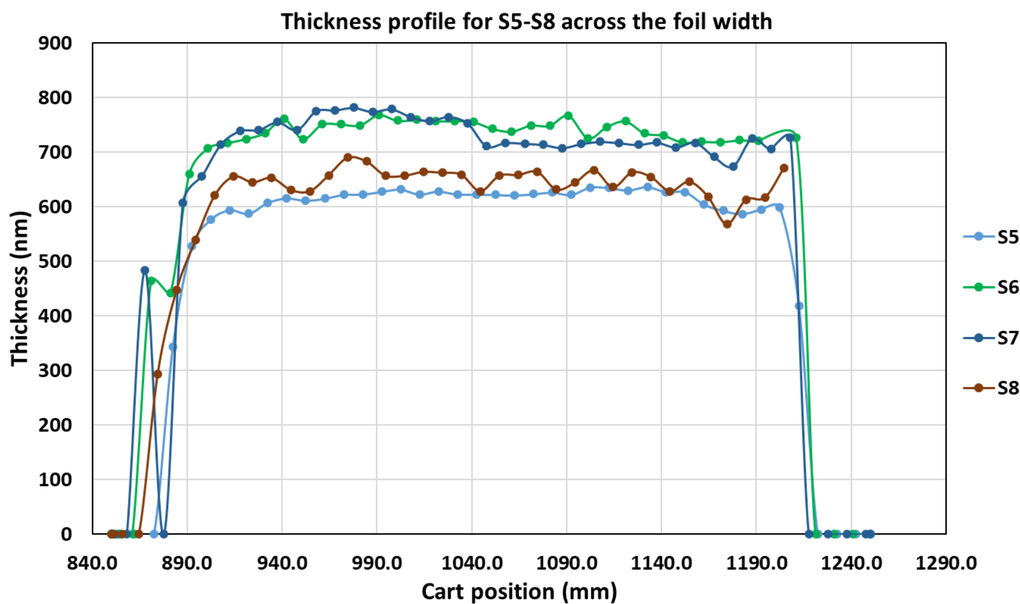

Figure 3.26: The thickness profile across full foil width for settings 5 to 8

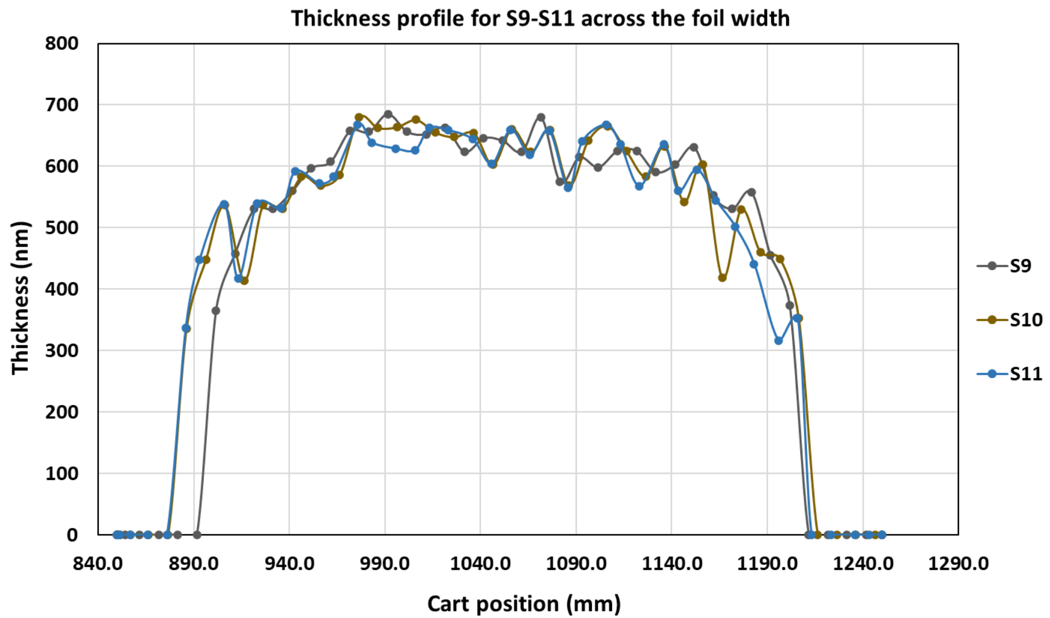

Figure 3.27: The thickness profile across full foil width for settings 9 to 11

In conclusion, using the ”optical thickness” model together with the measurement setup yields vital information relating to the thickness of the FTO layer being deposited and the extent to which the deposition is homogeneous. This insight is beneficial for the production team as they can know when the injectors are not performing as expected and can adjust their position or gas flows accordingly, to ensure optimal thickness of the FTO layer during the R2R production run in the APCVD machine.

Among the 11 settings that were done, 8 of them were sent for cross-SEM (scanning electron microscopy) analysis to Delft University of Technology, which is done with a SEM Hitachi Regulus 8230. The comparison between the thicknesses obtained from in-line ”optical thickness” method and the offline ”cross-SEM” method is illustrated in figure 3.28.

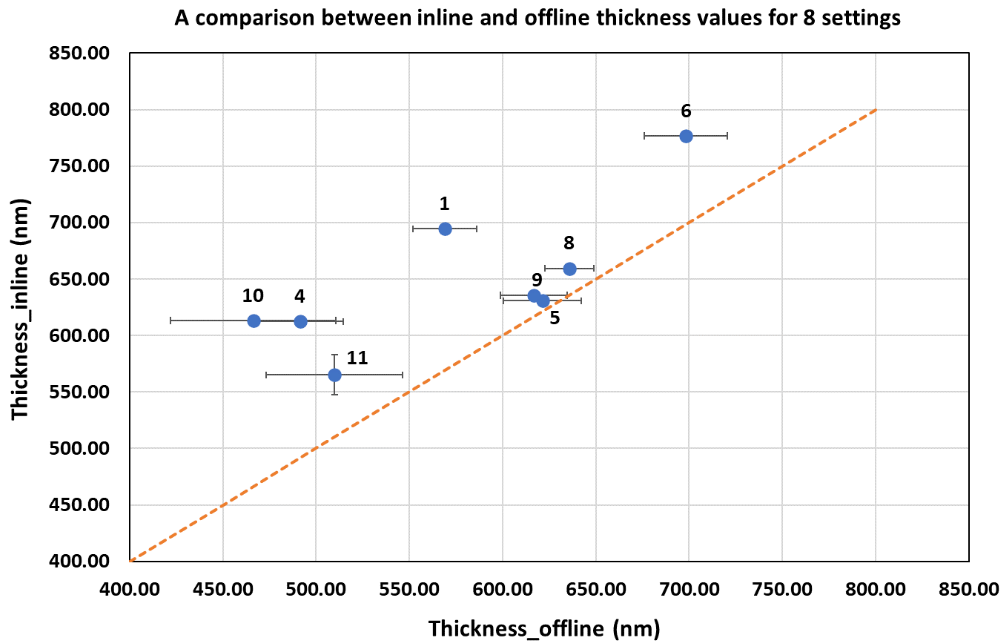

Figure 3.28: Comparison between the thickness obtained in-line and from offline measurements (the vertical error bars are not visible due to very less error spreads)

This graph presents the data for the samples taken from 8 settings of experiments, the numbers of which are indicated close to their corresponding thickness values (blue marker point). In the horizontal axis, the thickness values as obtained from the in-line diagnostics are shown while the vertical axis depicts the measurement values from cross-SEM analysis. The orange dashed line denotes the $y = x$ line. It can be observed that the thickness values tend to lie above this orange line, which signifies that the thickness values from in-line diagnostics are over-estimated as compared to the offline measured values. This can be related to the fact that the two methods use different approaches of estimating the thickness of the FTO layer.

In a SEM analysis, two points are manually fed into the software between which the thickness value is measured. Whereas in the "Optical Thickness" method, the thickness of the FTO layer is calculated by considering a constant refractive index (n_0) of **2.305**, as mentioned in section 3.2.3. Therefore, it is possible that this value of refractive index could be higher (due to the inverse relation of thickness with the refractive index, refer equation 3.40) than the value taken into consideration in the current calculation. A probable reason also could be that during the SEM analysis, the part that was chosen for obtaining the thickness was thinner. Another observation that also relates to this fact is the error spread in the offline measurements (horizontal error bars), which are much higher as compared to the errors in the in-line measurements (vertical error bars). The errors in mean for the offline measurement are calculated by using the formula specified in equation 3.39, for 5 measurements taken at different points for each setting.

From these observations it can be concluded that the results from in-line diagnostics are statistically sound in terms of less spread in errors than the offline measurements. With this being stated, the differences in values from SEM could also be related to the fact that the Al/FTO foils are not completely flat while the measurement is being taken. Another reason for this variation might be that in the optical model for obtaining thickness, the surface roughness of the FTO layer is not considered. But while measuring thickness using SEM, it can be decided whether to measure it from the top of the crystal or from the bottom of the crystal, which can result in a significant difference of about 20-50 nanometers (depending on the roughness of the surface crystal).

(a) A cross-SEM image taken at 1 micron resolution resulting in a total FTO thickness of 617 nm

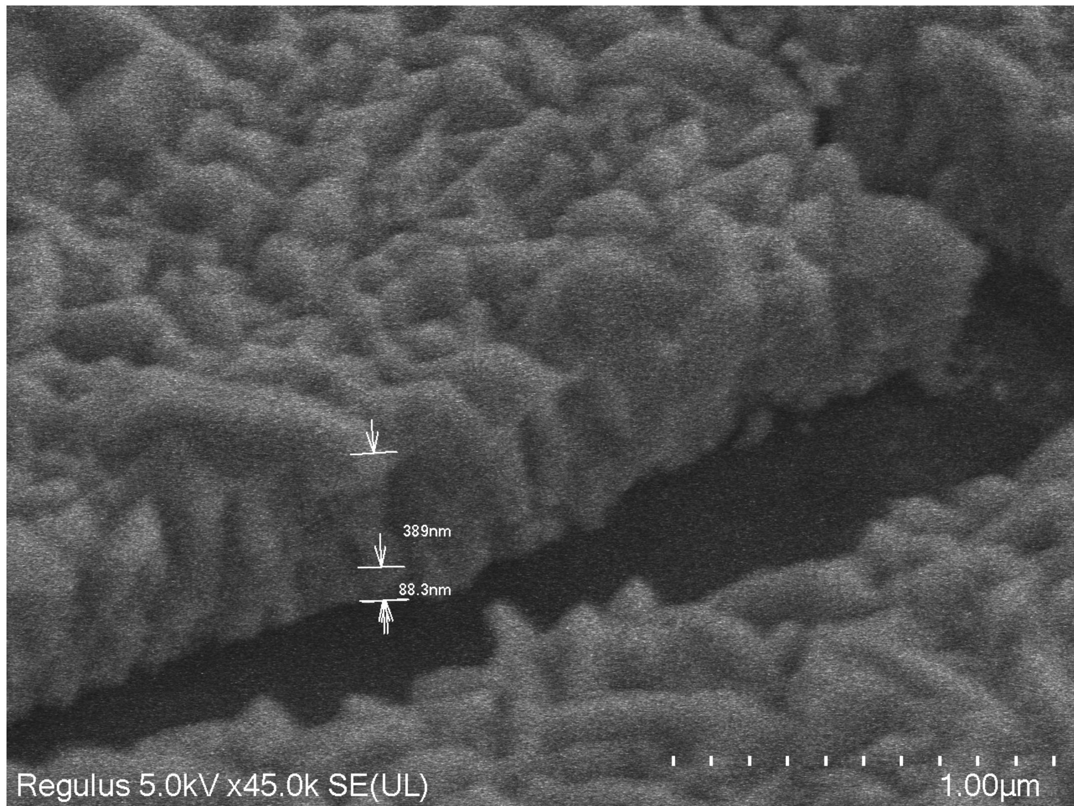

(b) A cross-SEM image taken at 1 micron resolution resulting in a total FTO thickness of 478 nm

Figure 3.29: Two different values of thickness for a sample of setting 4, showing a difference of > 100 nm owing to the roughness and curved nature of the Al/FTO sample

Figure 3.29 depicts the cross SEM images taken at scales of 1 μm resolution, for a sample of fourth setting (S4). The total thickness of the layer, in the SEM image, is segregated into two parts as the deposited FTO layer consists of two parts; the incubation layer (initial growth phase) and the the bulk layer (on top of the incubation layer) [33]. It can be observed from both the figures that while one measurement (figure 3.29a) shows 617 nm of thickness, the other measurement made (figure 3.29b) is of 487 nm. This proves the hypothesis made earlier regarding the spread in the SEM thickness values, resulting from the surface roughness of the layer and/or the curved nature as received.

After understanding the results that can be obtained from the UV-VIS part of the wavelength spectrum, the focus will now shift towards the near infrared part of the spectrum. Figure 3.30 depicts the NIR part of the reflectance spectrum of the same 11 settings for which the UV-VIS analysis was done. The reflectance spectra obtained were then processed according to the Drude model fitting, discussed in section 3.3.2, in the software program. The opto-electrical parameters, charge carrier concentration (N) and mobility (μ), thus obtained for the deposited FTO for settings 1 to 11 are summarized in table 3.7. In this table the mean charge carrier concentration (in cm^{-3}) and mean mobility (in cm^2/V·s) are calculated over the entire duration of the setting at the center of the module and the error in mean values are also obtained using the equation 3.39.

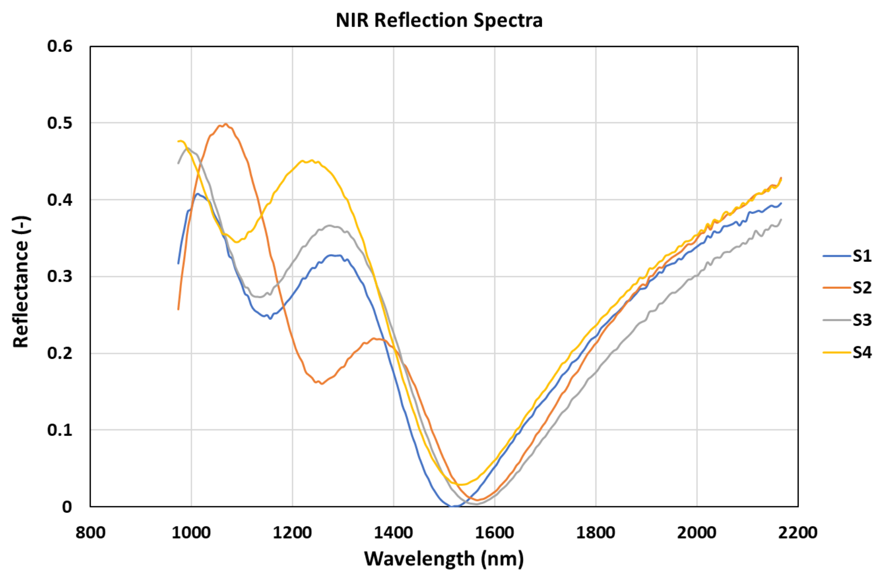

(a) Reflectance spectrum in the near infrared region for settings 1 to 4

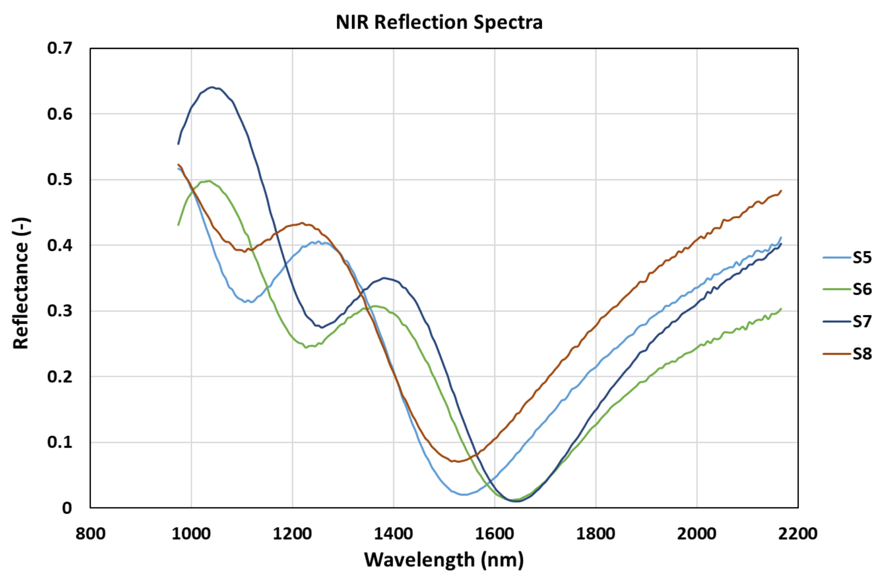

(b) Reflectance spectrum in the near infrared region for settings 5 to 8

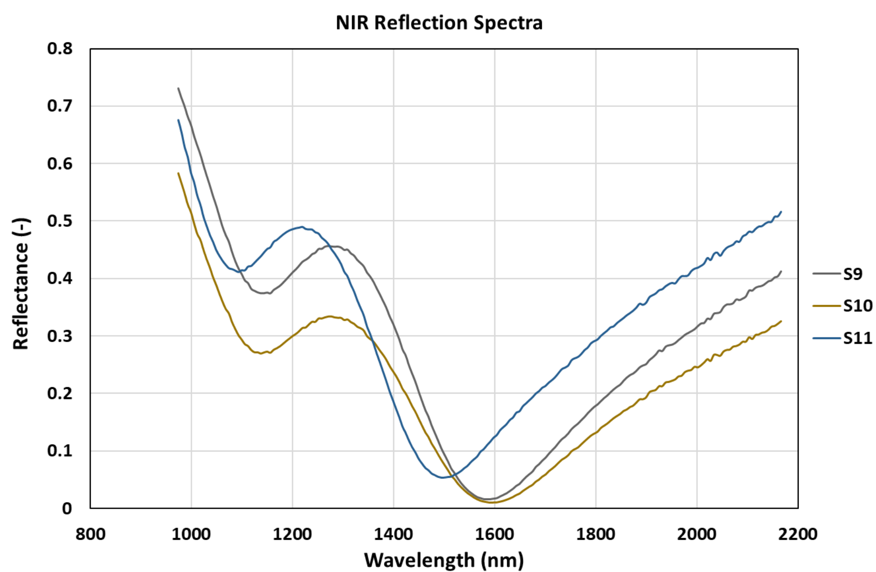

(c) Reflectance spectrum in the near infrared region for settings 9 to 11

Figure 3.30: The NIR reflectance spectra of different experimental settings carried out at HyET

Table 3.7: The opto-electrical parameters as obtained from the Drude model fitting for 11 settings using the NIR reflectance spectra of the aluminum/FTO stack

Sample	Mean N (10^{20}cm^{-3})	SD	E	Mean μ (cm^2/V·s)	SD	E
S1	2.407	0.50	0.10	14.44	1.48	0.29
S2	2.323	0.41	0.07	14.66	1.07	0.19
S3	2.238	0.19	0.03	16.98	1.68	0.29
S4	2.448	0.48	0.08	12.33	0.79	0.14
S5	2.503	0.43	0.08	12.66	0.76	0.14
S6	2.122	0.11	0.02	17.68	1.42	0.26
S7	2.296	0.74	0.13	16.33	2.73	0.46
S8	3.751	1.14	0.20	23.48	4.94	0.86
S9	3.275	1.11	0.19	18.51	6.26	1.07
S10	3.064	1.14	0.20	15.06	4.77	0.83
S11	4.609	1.95	0.33	14.43	8.08	1.36

From figure 3.30 and table 3.7, it can be observed that the concentration of free carriers is sensitive to the change in the position of the ”black wavelength”. As the position of the black wavelength reduces, the free carrier density increases and vice-versa, which is in agreement with the relations obtained while developing ”Model A”. Regarding the location of the wavelength where the deposited FTO reflects off the minimum incident light, it can be inferred from figure 3.30 that this wavelength range lies between 1500 to 1700 nm. On the other hand, the mobility of these free electrons cannot be directly correlated with the position of black wavelength or slope alone. This suggests that the mobility of free electrons inside the FTO layer is a more intrinsic property which depends largely on the recipe used to deposit the layer.

As illustrated in the thickness analysis part, the measurement setup is also capable of producing variation of these opto-electrical parameters across the width of the foil similar to the thickness profiles. However, from the production point of view, the thickness uniformity/non-uniformity is a more crucial parameter than the level of homogeneity in the charge carrier concentration and mobility, as the team handling the recipe steer their inputs majorly according to the optimal thickness of the FTO layer. Therefore, a full width variation in N and μ is not presented in this section. Instead, the analysis that adds value to both the technology team as well as the production team is how well do the obtained values correlate with the actual measurement values done via standard procedures (Hall effect measurements [31]). With the help of this analysis it can be known to what extent can these values be trusted and that they are actual representation of the material being produced out of the production line. Hence, the results following will depict the comparison between the electrical parameters obtained in-line optically and the values that were obtained during the Hall effect measurements done at the Delft University of Technology. Figures 3.31 and 3.32 present the comparison plots of charge carrier concentration and mobility respectively.

From figure 3.31, it can be observed that the values obtained from the in-line diagnostics at HyET correspond quite well with the values measured with the Hall effect setup. The reason for stating this is because the measured values from both the diagnostic systems for all the settings shown remain close to the $y = x$ line (orange dashed line). Among all the settings, S11 lies exactly on the dashed line and except settings S4, S9 and S10, the remaining settings tend to be closer to the line. From this observation, it can be inferred that the values obtained for charge carrier concentration from the optical measurement system in-line can be trusted. Another observation which is evident from the graph is that the values of charge carrier concentration obtained in-line are slightly under-estimated as opposed to the offline measured values, with one exception being setting 9. Considering now the figure 3.32, the trend is the exact opposite of the correlation between the in-line and offline charge carrier concentration values. In other words, the optical mobilities obtained are over-estimated as compared to the mobilities obtained from the Hall effect measurements. This can be attributed to the fact that the optical method mainly probes the bulk (crystal) of the FTO layer at the top surface, while the Hall-mobility is also sensitive to the grain boundaries which limit the mobility of free electrons [34]. Another fact that could explain the difference in values of electrical parameters obtained optically and electrically is that

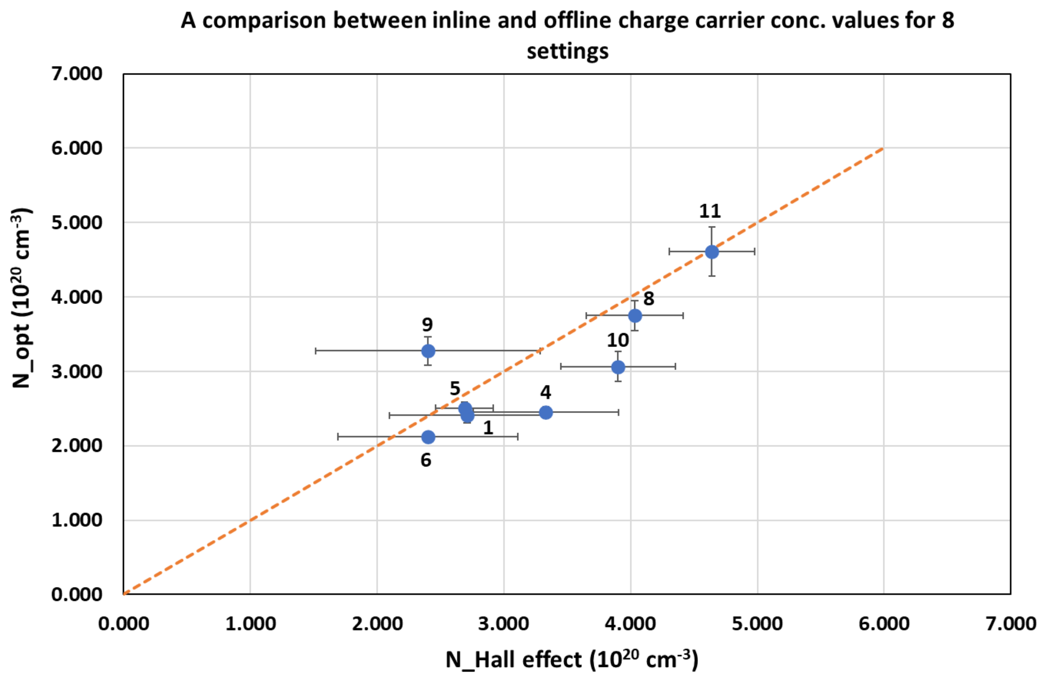

Figure 3.31: Comparison between the charge carrier concentrations obtained in-line (optically) and from offline measurements (electrically) (some of the vertical and horizontal error bars are not visible due to very less error spreads)

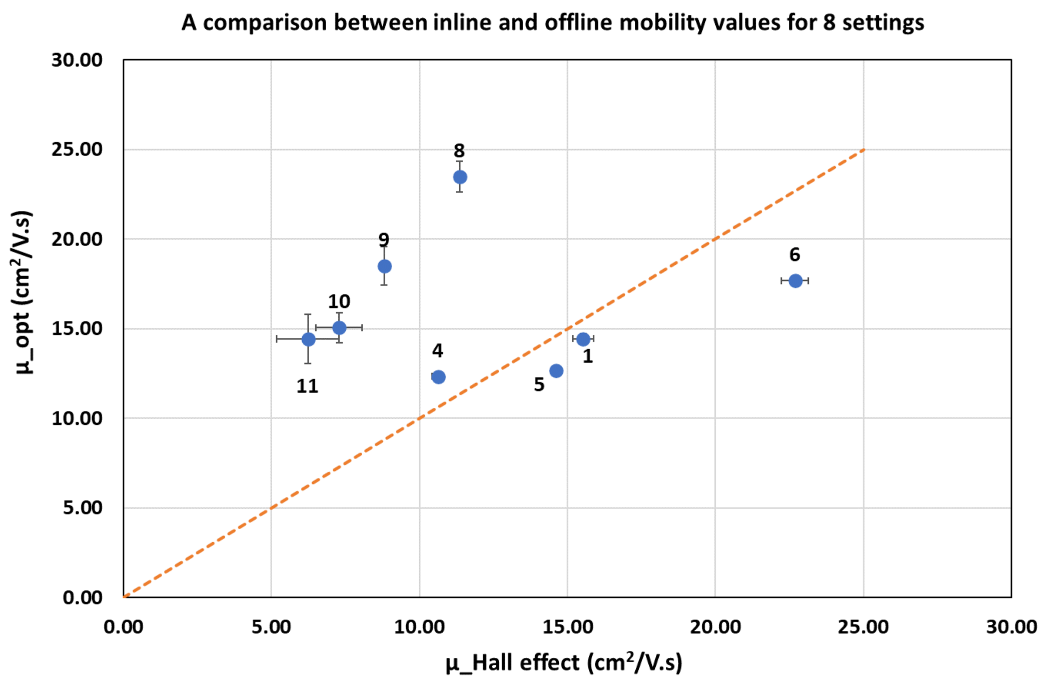

Figure 3.32: Comparison between the mobilities obtained in-line (optically) and from offline measurements (electrically) (some of the vertical and horizontal error bars are not visible due to very less error spreads)

the effective mass of electrons is assumed to be **28%** less than the mass of electron in the optical method, which can be different for the two measurement methods.

From the obtained (optical) free carrier density (N) and (optical) mobility (μ), the conductivity of the FTO layer can be calculated using equation 3.21. The obtained conductivity can then be utilised in

equation 3.22 to get the sheet resistance of the layer deposited, as the thickness of the FTO layer is also known. This is one of the important parameters as it plays a key role in deciding the effectiveness of lateral charge carrier (electrons) transport. Therefore, lesser the sheet resistance, more effective is the lateral transport of electrons. Figure 3.33 depicts the comparison between the optical sheet resistance values obtained in-line and measured sheet resistance values from the Hall effect.
Note: The Hall effect measurements do not directly yield the values of sheet resistance. Therefore, the sheet resistance values were calculated by using the N, μ and the conductivity obtained from the measurement. Also, the thicknesses taken into account here were from the SEM measurements done offline.

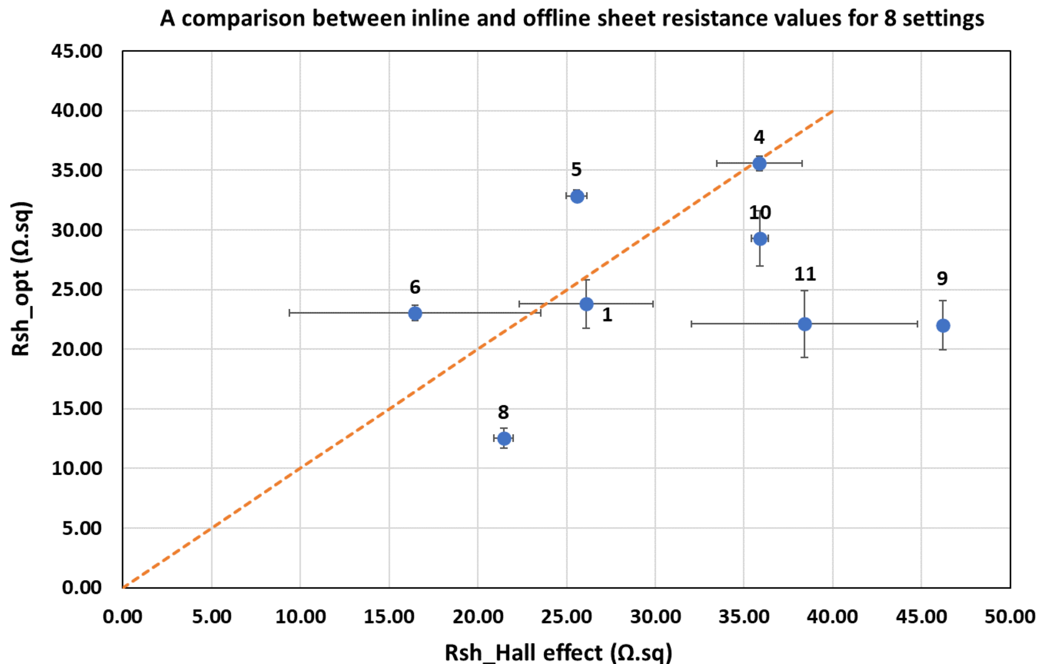

Figure 3.33: Comparison between the sheet resistances obtained in-line (optically) and from offline measurements (electrically) (some of the vertical and horizontal error bars are not visible due to very small error spreads)

From figure 3.33 it can be observed that the sheet resistances obtained from Hall effect measurements are, in most of the settings, higher than the sheet resistances obtained from the optical method. This can be correlated to two parameters that affect the sheet resistance value, i.e., conductivity of the layer and its thickness. As observed in figure 3.28, the thickness values from offline SEM measurements were less than the obtained thickness from in-line diagnostics and as the sheet resistance is inversely proportional to the layer thickness, it might explain the higher values of sheet resistance from Hall effect measurements. For the settings which had almost the same thickness, both from SEM measurement and optical method, the difference in their sheet resistances can be attributed to the difference in the layer conductivities. Again, the error spreads from Hall effect measurements are higher because of high spreads in the thickness values from SEM measurements, while the optical method yields smaller errors consistently, for all the parameters compared in this section.

In conclusion, the measurements from the optical method show good correlation with the results obtained from offline measurements, in terms of not being largely off from the Hall effect values. The sheet resistances discussed in this section were one way of characterizing the FTO layer optically, but this parameter is also measured electrically at HyET using another tool online, which will be discussed in detail in the next chapter. The values obtained from this tool will also be compared with the optical and the Hall effect sheet resistances to get a clear picture of how well the different measurement techniques agree with each other.

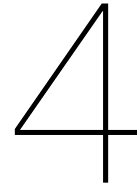

Upgradation of the electrical sheet resistance measurement device

This chapter deals with the improvements and adaptations made to the existing online sheet resistance measuring device, in order to make it robust and accurate enough to generate reliable data. The first section discusses the background and motivation behind going for the upgrade. Section 2 introduces the concept of the measurement, while in section 3, a comparison is made between the past measurement setup and the present setup with adaptations. The final section presents the results from the improved sheet resistance measurement tool and their correlation between the optical and Hall effect sheet resistances.

4.1. Background and motivation

In the HyET Solar R2R production process the FTO is deposited and grown on an aluminum substrate. Therefore, determining the sheet resistance was only possible via offline measurements, which were time consuming and extensive transfer processes. Thus, the WONDER measurement tool was developed in-house which would reduce the delay in getting information about the quality of the FTO deposited. The acronym WONDER stands for ”Wonderful Online Non Destructive Electrical Resistance measurement”. The measurement principle of the tool is summarized in the next section, as developed by Robin Quax during his master’s thesis [35]. However, in the recent times the device online at the APCVD machine, did not generate accurate sheet resistance results consistently, of the aluminum/FTO stack for last few production runs. Therefore, it was decided to rectify the measurement tool and make it more robust, in terms of easy troubleshooting in the future, if and when necessary. This involved adaptations and/or changes both in the hardware as well as the software aspect.

4.2. The concept of Wonder measurement

The electrical sheet resistance of the Transparent conductive oxide (here, FTO) layer is a crucial parameter to judge the quality of the layer deposited. A high resistance from the FTO layer will lead to loss of power in the form of heat dissipation. Conventionally, it is measured via four point measurement [36] and the Van Der Pauw method [31]. In these methods two probes are connected to the sample and a current is driven through them, while the two other probes measure the potential drop across the current probes. This measured potential drop is then converted into sheet resistance by using the appropriate correction factor, according to the geometry of the sample and considering the fact that the current is applied via a point source and collected via a point drain. As a prerequisite for these methods, the conducting layer, of which the sheet resistance is to be measured, needs to be placed on a dielectric carrier. If the carrier conducts well, the current shall only pass through the carrier which will result in not obtaining the resistance of the layer of interest. Since the HyET process employs a metal (aluminium) as a carrier, the measurement becomes labor intensive as the aluminum has to be etched away and then transferred to a dielectric material before measurement. This transferring process was very disadvantageous in terms of labor costs, longer learning cycles & feedback times and risks of

sample cutting from the foil. These issues formed the essence of creating the concept of an on-line non-destructive electrical sheet resistance measurement device.

To measure the sheet resistance of the TCO layer on the aluminum carrier, it was necessary that the current applied should pass through the layer of interest rather than the metallic carrier. This issue was resolved by making use of a "necessary evil" that always forms when aluminium is exposed to the surroundings, aluminum oxide (Al_2O_3). This is a very thin oxide layer (of about 1-2 nm) that forms during the process. The resistance of this layer plays a key role in determining the sheet resistance of the FTO layer, as depending upon its resistance compared to the sheet resistance, a current will flow through the TCO. This scenario is depicted in figures 4.1a and 4.1b for two different ratios of the TCO sheet resistance and the oxide layer resistance, where the bold red arrows imply that a significant amount of current flows through the layer.

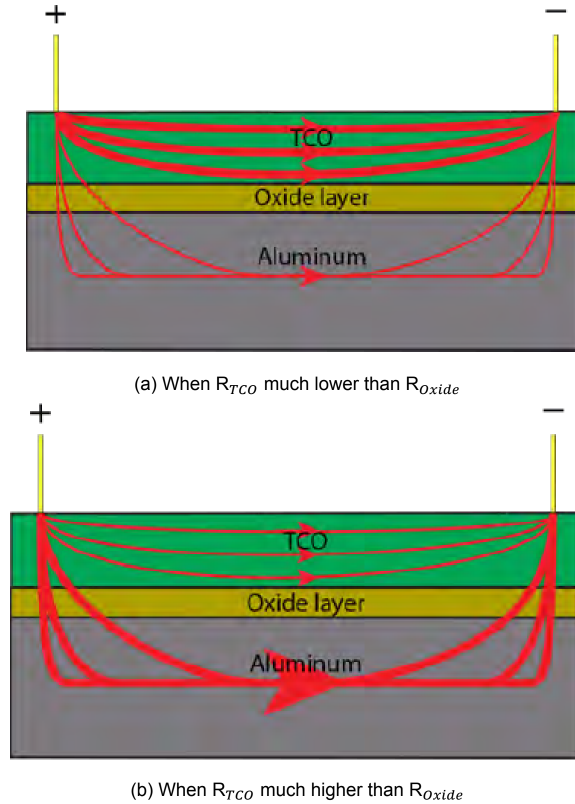

(a) When R_{TCO} much lower than R_{Oxide}

(b) When R_{TCO} much higher than R_{Oxide}

Figure 4.1: The flow of current through the Aluminum/TCO stack with a resistive inter (oxide) layer for different ratios of sheet resistance and resistance of the oxide layer [35]

The potential drop across the two point (current) contacts (+ & - in the figure 4.1) will then be the function of the resistance of the TCO and the oxide layer. Thus, by measuring this potential drop as a function of position would result in estimating the resistances of these layers. Before developing expressions for the potential drop as a function of position, the shape of the electrode was considered and it was realised that among bus bar shaped and point probe electrodes, the latter is more suitable [35]. Point probes were chosen mainly because, the usage of long electrodes over the entire length of the TCO layer might damage the thin layer when pressed against it for measurement. Additionally, the point probe configuration was easier to establish. The expression for the potential (V) as a function of position (x) for point probe contact, as derived by Robin Quax [35], is given by,

$$V(x) = \frac{IR_{sq}}{2\pi}(K_0(\frac{|\frac{-q}{2} + x|}{\lambda}) - K_0(\frac{|\frac{q}{2} + x|}{\lambda})) \tag{4.1}$$

where, I is the applied current, R_{sq} is the sheet resistance of the layer, K_0 is a parameter that appears in the solution of the modified Bessel differential equation of second kind [37] with $n = 0$, (-$q/2$,$q/2$) are

the positions of the current source and drain respectively and λ is given as,

$$\lambda = \sqrt{\frac{\rho_i t_i}{R_{sq}^{TCO}}} \quad (4.2)$$

where, ρ_i is the resistivity of the oxide layer and t_i is its thickness. Here, λ is expressed in units of distance (mm). The equation 4.1 is used to find the sheet resistance of the TCO layer as well as the resistance of oxide layer. This expression generates values of resistances if sufficient data points are taken between the two current pins. From the study done by Quax [35], it was advised to have a spacing of voltage measurement pins smaller than 2.2 mm (considering a lower boundary for λ of about 2.2 mm). The measurement setup which was designed following the development of the expression is explained in the next section.

4.3. Measurement Setup–Past vs Present

This section discusses the measurement setup which was designed initially and its working, in the first subsection. The second subsection presents the changes that were incorporated to the existing design and the calibration test that was performed to check the correctness of this upgraded version.

4.3.1. Measurement setup–V1

For the setup, spring point contact probes with round heads were considered as the most suitable solution. The head diameter of the used probes were 0.5 mm, with a contact diameter (on the TCO) estimated around 10-20 microns, depending upon the depth of indentation. The probes were clamped between two gratings with grooves that were spaced 1.54 mm apart. To achieve sufficient resolution, 17 voltage pins were placed in between the current pins, which thus constituted a total of 19 pins in the tool. Figure 4.2 illustrates an offline (a prototype) version of the measurement setup which was then implemented online, at the APCVD machine, after verification of the theory. The principle of the offline setup is exactly the same when transferred to online, except the probe holder was adjusted in design such as to record measurements on a curved surface (on a roller).

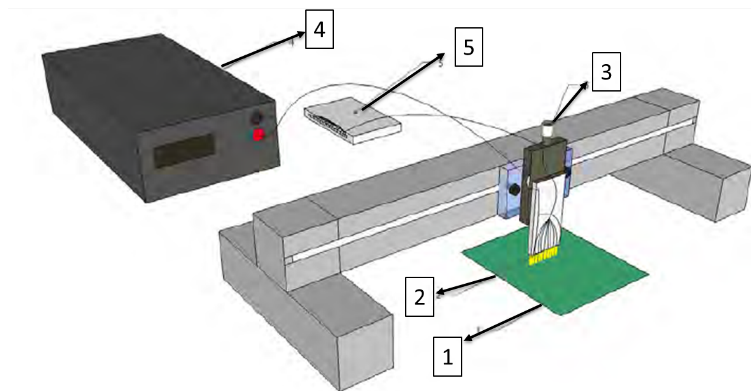

Figure 4.2: Schematic diagram of WONDER measurement setup V1 ([35])

The sample is placed below the pins on a flat surface (1). The probe head with spring probes (2) are contacted on the sample precisely by an adjustable arm which freely moves in the vertical direction (3). After the contact is made, a current of 100 mA is supplied to the sample through the two outermost pins by a Keithley current source meter (4). This amount of current was chosen as it was found out to be non-destructive to the sample and at the same time gives enough resolution in the measured potential drops. The measured potentials are then recorded by the National Instruments Data Acquisition (DAQ) device (5) in a Single Ended Non Referenced configuration and sent to the PC. When the pins were brought in contact with the surface of the sample without application of current, a noise level of 0.3 mV was determined. The middle pin was chosen to be at zero potential (grounded) and the potential drops were measured with respect to the spacing from this pin to the nth pin (where n ranges from 1-16). A pictorial representation of the probe head contact with the sample is depicted in figure 4.3. Here, for

demonstration purposes fewer pins (7) are shown, where the fourth pin is at zero potential. A LabVIEW program then plots the measured potential drops and fitted the function according to equation 4.1. An example of the fit of the measured data is presented in figure 4.4. In this graph, potential recorded from the pins are denoted in the vertical axis while the distance of the remaining pins from the zeroth (ground) pin is presented in the horizontal axis. It can be observed from the plot that there are 17 blue dots which indicate the potential drops at each pin with respect to the ground pin. The potential varies the most with distance close to the two points where the current is applied (1st (-0.6 V) and 17th (+0.6 V) dot in figure 4.4).

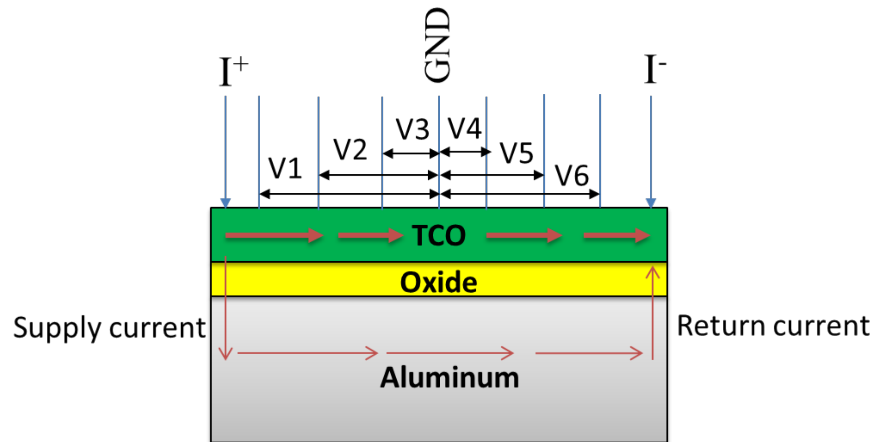

Figure 4.3: The principle of recording the potential differences across the measurement pins with respect to the ground (GND) pin

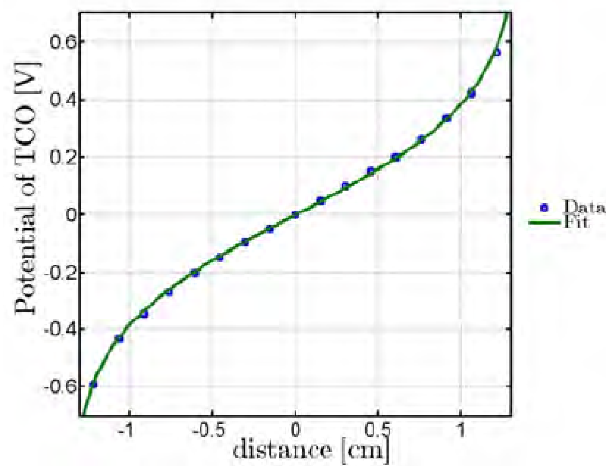

Figure 4.4: Fit result of an aluminum with FTO sample placed under the probes [35]

4.3.2. Measurement setup–V2

In this upgraded version of the measurement setup, although the principle of measurement remains essentially the same, some adaptations in making it more compact and robust have been made. The major changes that were incorporated into the existing system are as follows:

1. **Removal of external current source:** The Keithley current source meter has been removed from the setup. Now in the current measurement scheme, instead of supplying the current directly from the source meter, it is supplied from the existing data acquisition card (NI DAQ) from the voltage supply point. The voltage supply pin of the DAQ can supply a maximum of +5V DC at 50 mA current. Therefore, now the measurement was voltage driven instead of current driven, at the source. In order to engross this change, the existing mode of the configuration needed also to be changed. For this purpose, the Single Ended Non-Referenced configuration in the DAQ was changed to a new differential mode of measurement. This mode of measurement was the most suitable because:
   - The current that would be now supplied through the +5V DC from the DAQ has reduced from the 100 mA which was being supplied. This reduction in current was foreseen to increase the signal-to-noise ratio of the DAQ from the existing noise level of 0.3 mV. The differential mode of measurement is known to reduce the noise pick-up which improves the signal-to-noise ratio [38].
   - The input signal to the pin heads of the WONDER tool from the DAQ was desired to be a low-level signal (less than 1V) (to ensure that a high voltage does not damage the layer or the pins) and that it should also have a separate ground reference point, to where the returning current can pass. These two conditions were also satisfied by the differential mode [38].
2. **Reduction of measurement pins:** Now, as a result of the change in the mode of measurement, adaptations were also needed to be made in the connection from the DAQ to the pin heads of WONDER. Previously, in the version 1, there were a total of 19 pins including the current supply and return pins (two outermost pins). All the 17 pins in between generated a data point for the potentials at that point, which were then fitted using the equation in the software. But when using the differential mode, it was possible only to form 8 channels at the maximum owing to the configuration of this mode. Therefore, 4 pins were not required anymore. Additionally, as the current return pin would be connected to the ground reference point, there was no necessity of a ground pin in the middle. Owing to these two reasons, it was decided to remove 5 out of the 17 pins from the center, as depicted in figure 4.5.

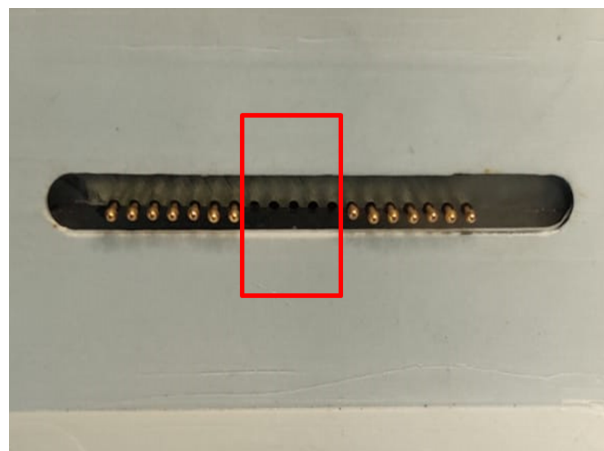

Figure 4.5: Removal of five pins from the existing 19-pin WONDER tool where the removed pins are highlighted inside the red rectangle

3. **Implementation of channel configuration:** Among the 14 pins in total, the outermost pins had the same functionality as before, where one pin supplied the current while the current returned

through the other pin. These two pins, therefore, formed two separate measurement points (channels). The remaining 12 pins now were paired with each other to form one channel. For example, the second pin from the left was paired with the second pin from the right, where one formed the negative terminal of the channel and the other formed the positive terminal. These paired pins were then connected to the pin-outs of the data acquisition card. This led to the formation of a total of 8 channels, in which, 6 were the paired pins channels from the WONDER to NI DAQ and 2 from the current supply and return pins to NI DAQ.

The amalgamation of all the mentioned changes and adaptations were incorporated onto a prototyping board (PB) of dimensions 14 cm by 14 cm. The connections on the PB and its electrical replacement scheme is illustrated in figure 4.6.

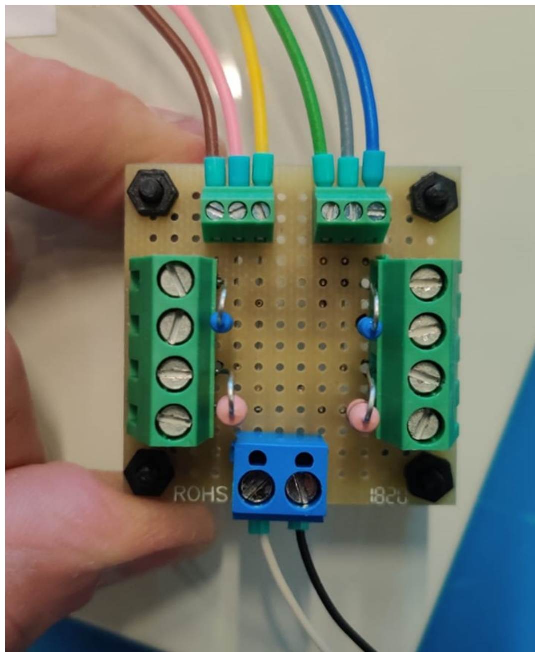

(a) The printed circuit board (PCB) which connects the DAQ and the pins of WONDER, current limiting resistors on the left and right side. The top of the PCB is connected to the DAQ while the bottom part is connected to the positive and negative current pins of WONDER

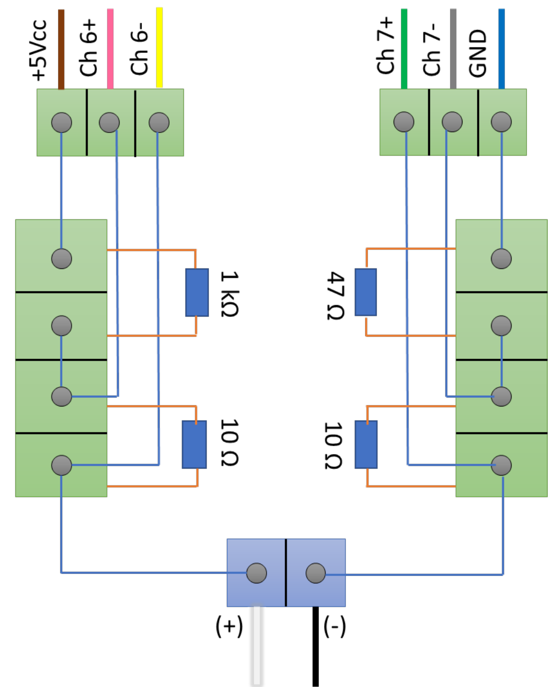

(b) Electrical replacement scheme of the actual PCB with 1 kΩ and 10 Ω resistors on the left side and 47 Ω and 10 Ω resistors on the right side

Figure 4.6: The implementation of differential mode of measurement in the measurement setup

Referring to the figures 4.6a and 4.6b, the brown wire carries the voltage supply from the DAQ to the positive current supply pin of the WONDER tool (white wire in the bottom). The channels 6+ and 6- form the positive current channel, while channels 7+ and 7- form the negative current channel. To ensure that the voltage supplied from the DAQ does not over-power the measurement tool, current-limiting resistors are placed on both the sides of the PCB. The supply side has a much higher resistance than the return side as the current flowing to the ground can easily travel without much resistance, but we need low current from the supply side so as not to damage the FTO layer while measurement. Here, the blue wire on the right hand top side in figure 4.6b signifies the grounding wire that connects the negative current pin (black wire in the bottom) on one side and the ground of DAQ on the other side. This feature also makes the upgraded setup different than the version 1, as in this scheme, the returning current flows to the ground which was not the case in previous scheme of measurement. A diagrammatic representation of the flow of currents in version 2 of the measurement scheme is depicted in figure 4.7. In this figure, the resistances R^+ and R^- are symbolic of the current limiting resistors on the supply (110 kΩ) and return (57 Ω) side respectively (chosen according to the specifications of the DAQ). Here, 3 channels are depicted for easy visualization of the scheme; the pins are connected in a similar manner to form 3 more channels (CH 0 to CH 5).

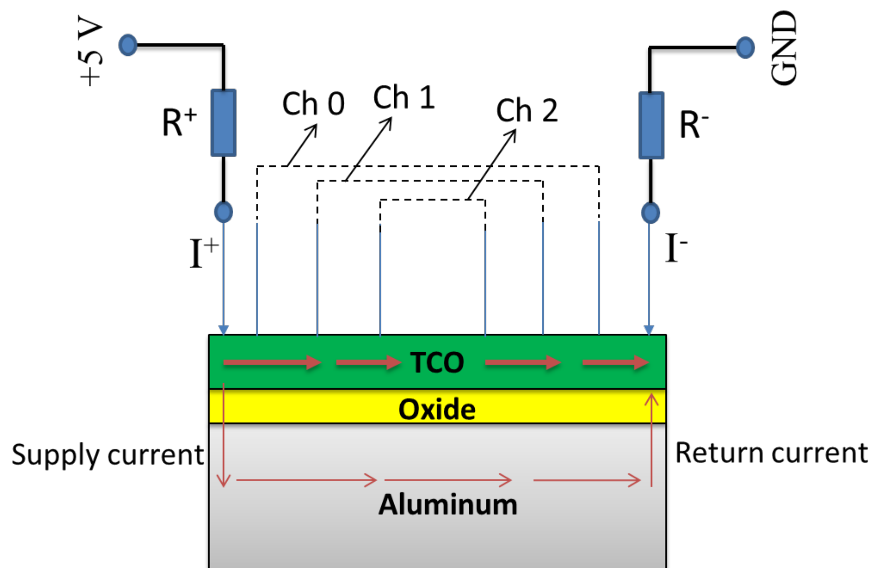

Figure 4.7: The measurement scheme of the second version of WONDER with paired pins forming channels (black dashed lines) and power supply from the DAQ on one side while being connected to ground of the DAQ on the other side

Testing and calibration of the new version

To ensure that the implemented circuit and wiring design for the hardware is functioning properly, a calibration test was performed. Calibration is typically done to check for the system's output and validation that all the measurement channels (in terms of current and voltage) are working properly and generating expected results. The primary objective of this test, therefore, was to check whether all the channels (CH 0 to CH 5, excluding the current supply and return channels) formed were generating the same amount of voltage drop across them. For this purpose, it was decided to perform a most basic test which involved measuring the voltages across these channels when the pins made contact with a metallic surface. Therefore, a calibration sample for detecting the channel voltage measurement health was created which is presented in figure 4.8.

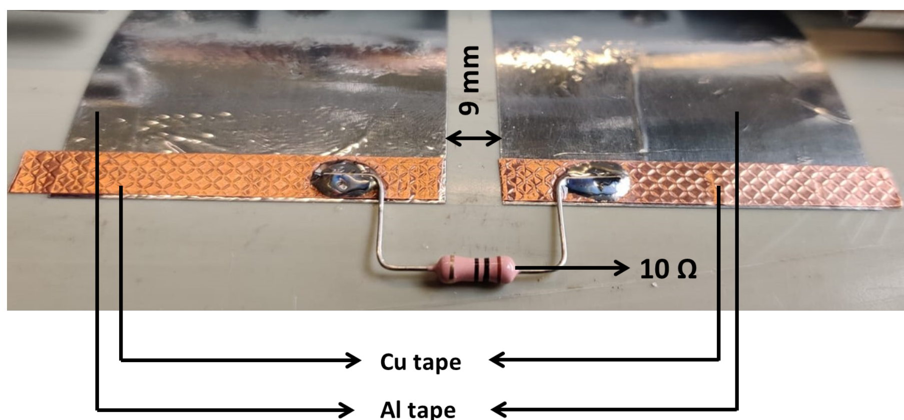

Figure 4.8: The channel health calibration sample as prepared for checking the measurement health of channels 0-5

The calibration sample depicted in figure 4.8 consists of two aluminum tapes placed 9 mm apart on a PVC (poly-vinyl chloride) substrate, which was kept equal to the distance between the two halves of the pins, such that all the pins rest on the aluminum. It can be observed on the bottom half of the sample, that a resistor of 10 Ω was soldered onto the copper tape, which is stuck onto the surface of aluminum tape. This resistor was placed so as to measure the voltage across the pins due to the current flowing across them, thereby acting as a calibration resistor. The WONDER tool was then pressed gently against the calibration sample, as depicted in figure 4.9.

Figure 4.9: The WONDER device pressed against the channel health calibration sample to measure the voltage drops across each channel

Results from the test

When the probe was pressed against the sample, the voltage drops across each channel including the two current channels (CH 6 (supply) & CH 7 (return)) were recorded in a LabVIEW program. The resulting voltages measured across each of the channels from 0 to 7 as displayed in the program is presented in figure 4.10. Figure 4.10a depicts the potential drops across the channels while figure 4.10b indicates the amount of current supplied and returned. From figure 4.10a, it can be observed that the channels from 0 to 5 result in the same voltage drop across them of about 98 mV, which satisfies the primary expectation from the test. However, channels 6 & 7 result in a voltage drop of about 47 mV which is almost half of the voltage drop occurring across the remaining channels. This result was not as per the expectations because theoretically, according to Ohm's law, if the amount of current being supplied to the one pin is the same as the current returning from the other pin (see figure 4.10b) then this 4.54 mA should account for a voltage drop 45.4 mV across all the channels. This voltage drop (+/- 2 mV) was however only seen at the two current channels. One of the probable reasons for higher voltage drops across channels 0 to 5 could be that the pins forming these channels are contacting the metallic surface more than the two outermost current pins. This could be possible if all the pins are not exactly on the same level.

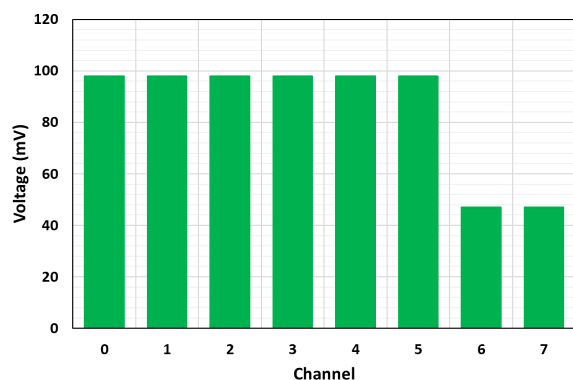

(a) Measured channel voltages when the pins were pressed against the calibration sample

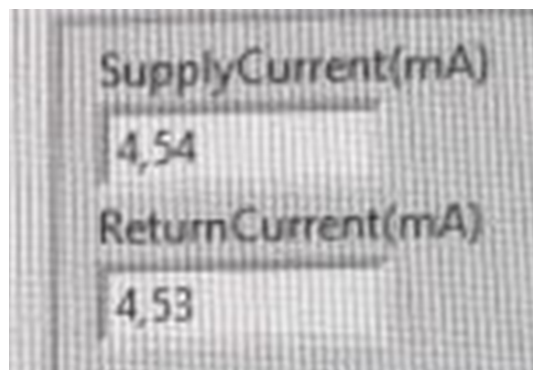

(b) The supplied (top) and the returned (bottom) currents, to and from the supply and return pins respectively

Figure 4.10: The results from the test performed on the channel health calibration sample

In conclusion, the test for measuring the health of the channels was successful, in terms of obtaining the same potential differences over the measurement channels. The discrepancy between the measured channel voltages over current supply & return pins and the remaining channels (about 50 mV) was rectified and brought down to a difference of around 25 mV, by adjusting the height of all the pins and making them on the same level as much as possible. Following the success of the test, this calibration sample was implemented as a standard operating procedure on-line at the APCVD machine, to ensure that the measurement channels are healthy before measuring potentials on the surface of deposited FTO. The next section discusses the data obtained following the implementation of this upgrade along with comparisons made to the sheet resistance values obtained optically and from the Hall effect method.

4.4. Results and Discussions

In this section, the electrical sheet resistances obtained from the version 2 of the WONDER measurement device are presented and discussed in connection to the 11 settings as presented in the results section of Chapter 3. Firstly, the sheet resistance values, as generated from the software program of the WONDER tool, for these settings are discussed. The obtained values are then compared and correlated with the obtained optical sheet resistances from the NIR characterization in-line and the sheet resistance values calculated from the Hall effect measurement setup at Delft University of Technology.

Before visualizing and understanding the sheet resistance results obtained, it is necessary to observe how the values are generated via the measurement procedure and the program. Figure 4.11 illustrates the ”Fit Result Cluster” of the WONDER LabVIEW program when a successful measurement was made on a sample of aluminum with FTO (not from one of the 11 settings). In this cluster, the measured Vs fit graph (labelled ”A”) shows the fit of the measured potential drops when the pins make contact with the surface of the FTO (green rectangles) and expected channel voltages (red rectangles). Here, due to a very good overlap of the expected and the measured voltages, the red rectangles are not clearly visible. The channel voltages from 0 to 5 decrease, as the pins paired to form the zeroth channel are closest to the current supply and return pins, while the fifth channel is farthest from them. The data points resulting from this graph are then plotted in another graph (labelled ”B”), where a linear fit of measured channel voltages (in the x-axis) and simulated (expected) channel voltages (in the y-axis) is implemented. The quality of the fit is decided based on the Donkerbroek parameter, as per the equation 3.10. When the value of this parameter is greater than 2 (here, 2.67), the ”measurement to be trusted” indicator turns green (labelled ”C”), thereby generating a trustworthy value of electrical sheet resistance.

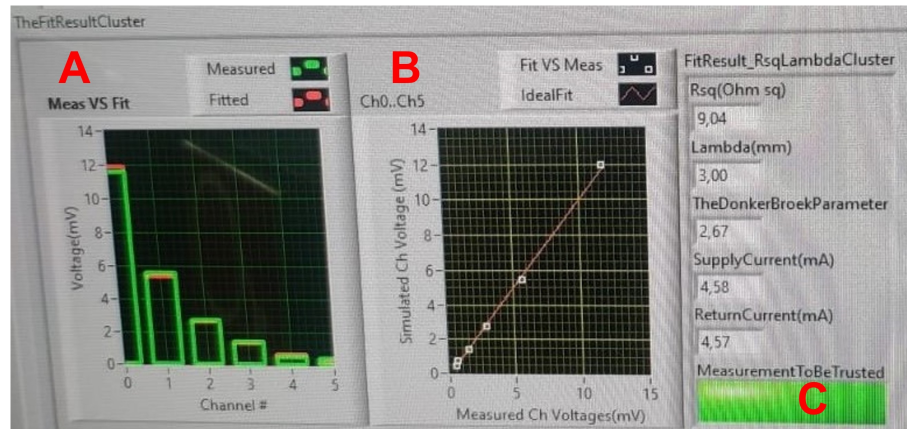

Figure 4.11: The Fit and Results cluster of the software program when a good measurement is made on the deposited FTO layer

The values of mean sheet resistances as obtained for the eleven experimental settings (for the entire duration of each setting) with their standard deviations and errors in mean are summarized in table 4.1. From the table, it can be inferred that the values of sheet resistances obtained have very small errors in their mean values, that lie within +/- 2 Ω/sq from their average values. It can be observed that only four settings out of the eleven show spreads more than 1, confirming that the results obtained from the measurement are trustworthy.

Table 4.1: The sheet resistances as obtained from the electrical sheet resistance measurement device for 11 settings of the aluminum/FTO stack

Sample	Mean R_{sh} (Ω/sq)	Standard deviation (Ω/sq)	Error in mean (Ω/sq)
S1	13.15	1.99	0.28
S2	12.93	2.30	0.54
S3	21.26	3.06	0.69
S4	25.96	3.58	0.78
S5	21.68	4.34	0.78
S6	14.71	5.27	0.74
S7	15.29	8.02	1.17
S8	21.40	8.64	0.97
S9	31.02	7.72	1.51
S10	34.21	8.60	1.92
S11	32.67	7.36	1.45

Now, the data obtained from the electrical sheet resistance measurement tool was compared against the optical and Hall effect sheet resistances for 8 of the 11 settings, as done in the results section of the previous chapter. Figure 4.12 presents the comparison of the sheet resistances obtained optically and electrically from the WONDER device, while figure 4.13 depicts the correlation of sheet resistances obtained from Hall effect and that of WONDER.

From figures 4.12 and 4.13, it can be observed that the sheet resistance values obtained from the WONDER measurement tool tend to have a better correlation with the sheet resistance values obtained from Hall effect measurements as compared to the optical sheet resistances. With exceptions of settings 1, 4 and 9 in figure 4.13, the remaining settings either lie on or very close to the $y = x$ line (orange dashed line), which supports this observation. It could be related to the fact that both the Hall effect measurements and the WONDER measurement make use of a similar measurement technique, where current is forced through two metallic contacts and the potential drop across the pins in between helps in generating a value of sheet resistance. Also, along with this it can be observed that the Hall effect sheet resistances are over-estimated with respect to Wonder measurements, which could be

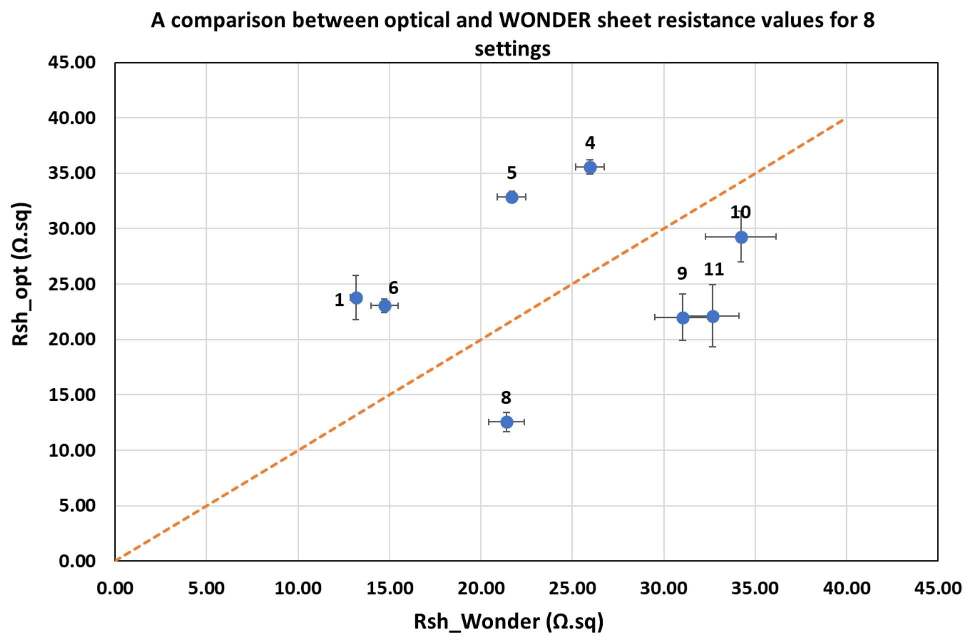

Figure 4.12: A comparison between the sheet resistances obtained optically from the NIR characterization of FTO and the electrical sheet resistances obtained from the in house measurement device for 8 different settings of FTO

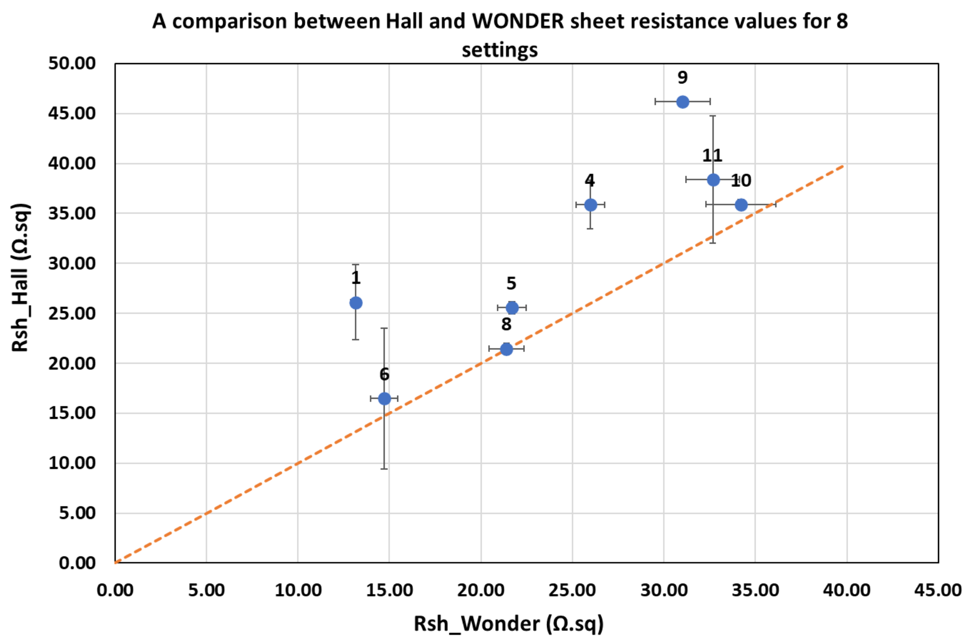

Figure 4.13: A comparison between the sheet resistances obtained from the Hall effect measurements and the electrical sheet resistances obtained from the in house measurement device for 8 different settings of FTO

possibly due to the utilisation of more pins to measure potential drops in Wonder and fewer pins in Hall measurements. The van der Pauw method forces current through two electrical metal contacts, while reading the Hall voltage across the other two metal contacts with the sample, making it essentially a 4-point method [31]. From the comparison of two point and four point method, it is known that the former gives higher values of sheet resistances as compared to the latter due to higher contact resistances of the probes playing a role in the two-point approach [39]. Similarly, as the Wonder measurement makes use of 12 pins in between the two current pins, a lower value of sheet resistance can be expected.

While from figure 4.12 it can be observed that the sheet resistance values for the settings partially lie above the orange dashed line and partially below it. There is an average absolute difference of about 50% in the sheet resistances obtained optically and from WONDER. This difference can be attributed to the two very different measurement methods used for sheet resistance determination. The optical method generates electrical parameters, as a result of which the sheet resistance is calculated; while the Wonder scheme applies current and measures the potential drop, as a characteristic of the resistance to the flow of supplied current through the FTO layer. Also, the procedure of taking measurements with the Wonder tool is manual, as opposed to the optical sheet resistance which is obtained in-line at the APCVD machine by an automated cart flashing light on the surface of the layer. This manual operation may introduce personal errors in the measured data. On this note, it can be observed from the two graphs that the spreads in average values in increasing order are seen in optical sheet resistances (average error of 1.4 Ω/sq), Wonder electrical sheet resistances (average error of 2.0 Ω/sq) and Hall effect sheet resistances (average error of 2.7 Ω/sq).

To conclude, the electrical sheet resistance measurement tool in house at HyET has been retrieved back to produce reliable results again with minimal errors in consecutive measurements. Along with that the robustness of the device has been enhanced, in terms of making the measurement system compact, reduction in current supplied with decreased noise level added and easy to troubleshoot if and when required in the future.

5

Calibration of the PECVD diagnostic device

This chapter focuses on the methods of calibration that were developed for the non-contacting capacitive probe, used to characterize the Si layers deposited in the PECVD process. The first section discusses the background and motivation behind the calibration of the device. In section 2, a brief explanation about the probe circuit is described. Section 3 describes the first approach towards calibration along with the results from the experiment. In the fourth section, a second method for the calibrating the probe is discussed along with its results. Finally, the summary and conclusions of the two approaches are mentioned.

5.1. Background and motivation

Upscaling of HyET Solar to higher production capacity, requires on-line diagnostic devices to be implemented in the PECVD machine in which larger widths of substrate material would be processed. Prior to installing the non-contacting capacitive device in the machine, it is necessary to ensure that reliable data are obtained from it. Therefore, the need for calibration of the device arises. According to the functionality of this tool, as described in the second chapter, the measured output signal of the probe depends on the time dependent voltage developed on the n-layer of the stack. The n-layer faces upfront towards the receiving element as, at HyET, the Si layers are deposited in a superstrate configuration [15]. This time dependent voltage, in turn depends on the distance between the n-layer and the surface of the probe, as it affects the capacitance between the photovoltaic material and the probe. This capacitor affects the "Gain", provided by the operational amplifier in the circuit, of the device. Therefore, the motivation was to develop an online calibration method which can have a direct link between the measured output voltage and the gain of the circuit, by estimating this capacitance between the n-layer and the receiving element of the probe. Once this capacitance was known, the open circuit voltage on the n-layer would be measured reliably, acting as a correction factor for the measured output voltages.

5.2. Understanding the probe circuit

Before describing the two approaches that were proposed to observe the effect of the capacitance, between the n-layer and the receiving element, on the gain of the circuit, it is important to learn about the circuit design. Therefore, in this section, the probe circuit along with an explanation of its components will be discussed. Figure 5.1 depicts the actual circuit design of the probe.

In the circuit diagram as illustrated in figure 5.1, A and B indicate the two operational amplifier circuits, through which the input voltage (V_{in}) from the receiving element gets amplified and an output voltage (V_{out}) is measured. Focusing first on circuit A, it consists of one operational amplifier operating in a differential mode, that receives the input voltage at its inverting (-) input terminal. The non-inverting terminal (+), on the other hand, is grounded. Further, the amplifier consists of one resistor (5 GΩ) and

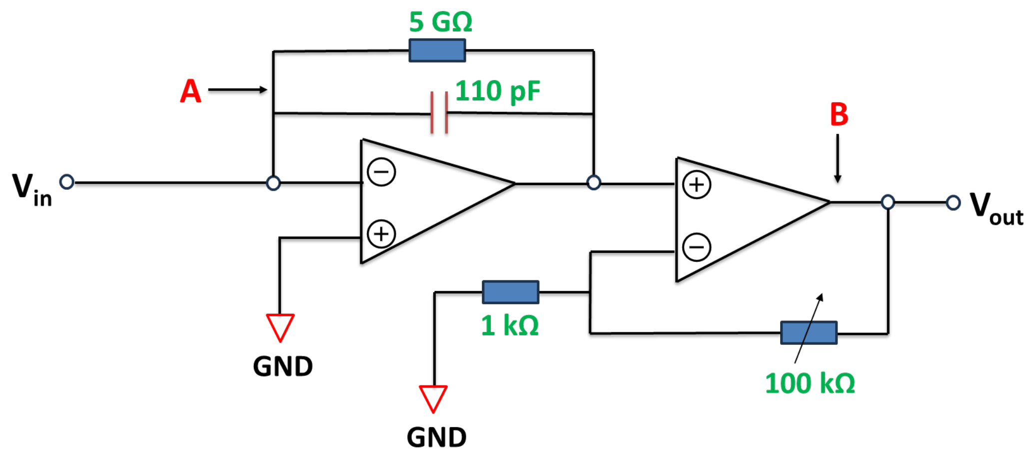

Figure 5.1: The interim circuit design of the probe consisting of two operational amplifiers and four feedback components

one fixed capacitor (110 pF), which form a feedback impedance (Z_f). The gain of this circuit depends thus upon the input impedance (Z_i) of the voltage coming in to the circuit, as the gain of the circuit is given by [40],

$$(\frac{V_o}{V_i})_A = -\frac{Z_f}{Z_i} \tag{5.1}$$

The circuit B is a non-inverting operational amplifier that receives the output voltage from circuit A at the non-inverting (+) terminal and amplifies the signal by its gain factor. At its inverting terminal, it consists of two resistors among which one is variable (100 kΩ) and another is fixed (1 kΩ). In this case, the gain is purely dependent on the resistances (for an ideal operational amplifier) connected to the inverting terminal of the amplifier and can be expressed as (considering the variable resistor to be at its maximum of 100 kΩ) [40],

$$(\frac{V_o}{V_i})_B = 1 + \frac{100}{1} = 101 \tag{5.2}$$

From equations 5.1 and 5.2 it can be observed that, while the gain of circuit A is dependent on the frequency at which the input voltage is being received (because of the presence of the capacitor) by the receiving element, circuit B has a definite resistive gain of 101 that is independent of frequency. This aspect of circuit A is investigated thoroughly in the methods adopted to calibrate the device and in understanding the relation between the capacitance (between the probe and n-layer) and the gain of the circuit.

5.3. Method A: Top Capacitor Approach

This method is the continuation of a design proposal which was made during my internship period at HyET for estimating the capacitance between the photovoltaic material and the sensor area of the probe [41]. The proposal made was the following:

- To add an extra conducting glass plate, in the form of an ASAHI U-type glass which comes with a pre-deposited FTO layer, on the top of the existing receiving element inside the probe.This glass plate had its dimensions equal to the area of the rectangular hole inside the probe, which is 19 mm by 23 mm.
- Prior to placing this glass plate inside the hole, the edges along the length of the plate were insulated by sandblasting the FTO (about 2 mm on both the long edges), as depicted in figure 5.2. This was done to remove any effects of parasitic capacitance or resistance that might act due to the edge to edge interaction between glass plate and the hole.
- To apply an external AC voltage on this glass plate, simultaneously placing a metal plate below the probe area (for introducing the capacitance between probe area and the ground (metal being

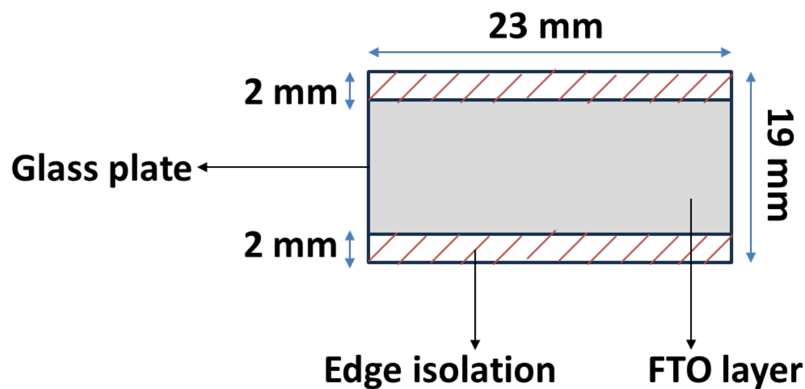

Figure 5.2: The proposed ASAHI glass plate design, to be placed inside the probe

regarded as zero potential)). The reason for applying an AC voltage signal was due to the presence of capacitance (between the metal plate and receiving element), which does not allow a DC signal to pass through.

- Now knowing the applied voltage (V_s), capacitance due to the added glass plate (C_s), and the output voltage on the probe (V_p), the capacitance between the probe area and the metal plate (C_p) can be estimated. This was possible due to the formation of a voltage divider circuit, illustrated later in the experimental methodology section.

The proposal was first decided to be tested offline, i.e., with an experimental setup, prior to its implementation in-line on the PECVD machine. The methodology followed in accordance with this proposal made, is discussed in the following sub-section.

5.3.1. Experimental methodology

The first step of the experiment was preparing the designed glass plate, as depicted in figure 5.2, for an external application of voltage to it. For this purpose, a copper tape was stuck on to the FTO layer to which a wire could be soldered, that could carry the voltage from the source supply. Figure 5.3 depicts the modified glass plate for applying a voltage to it, from the analog output (AO) of National Instruments Data Acquisition Card (NI DAQ). The wire soldered to the Copper tape was chosen to be a thin coaxial cable (such that one branch can be used to supply voltage and the other can be connected to a common ground, to avoid extra noise into the applied signal) with high impedance for two main reasons; first, a thicker cable would cause higher bending moment, thereby creating a risk of lifting off the glass plate from its desired position, second, a lower impedance of the cable could add stray capacitance in the form of noise to the signal.

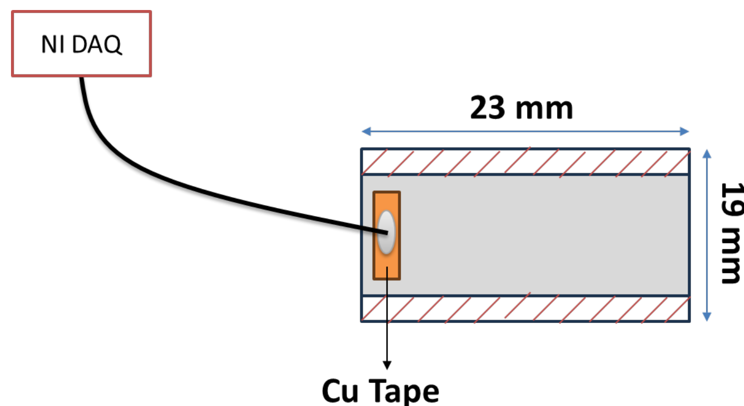

Figure 5.3: Modified glass plate for application of external AC voltage from the DAQ

After the glass plate was prepared for applying a voltage, it was placed carefully inside the probe on the top of the existing receiving element. Figure 5.4a presents a cross sectional view of the situation after introduction of this glass plate inside the probe, and a metal plate beneath the probe area. The dashed lines between the glass plate and the receiving element indicate the distance between the conducting FTO layer on the top surface of the glass and the conducting area of the receiving element. This distance is mainly due to the thickness of the ASAHI glass plate (t), being about 1.5 mm. On the top of this glass plate a voltage, V_s, is applied. The metal plate is kept at a distance *d* (in mm) from the receiving element, to introduce a capacitance between them.

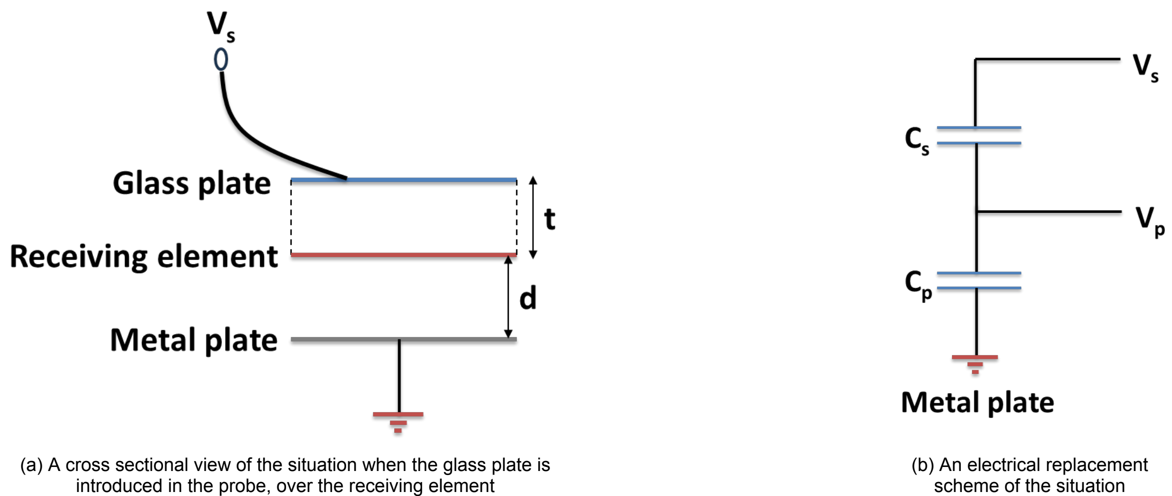

(a) A cross sectional view of the situation when the glass plate is introduced in the probe, over the receiving element

(b) An electrical replacement scheme of the situation

Figure 5.4: The scenario after the glass plate was introduced inside the probe

Figure 5.4b represents an electrical replacement scheme of the components depicted in figure 5.4a. In this figure, the capacitance, C_s, is introduced as result of the thickness of the ASAHI glass plate on top of the receiving element. The capacitance, C_p, is introduced due to the distance of separation between the metal plate and the probe area. Together, these passive components form a voltage divider circuit, where the output voltage of this circuit is the voltage developed on the probe, V_p.

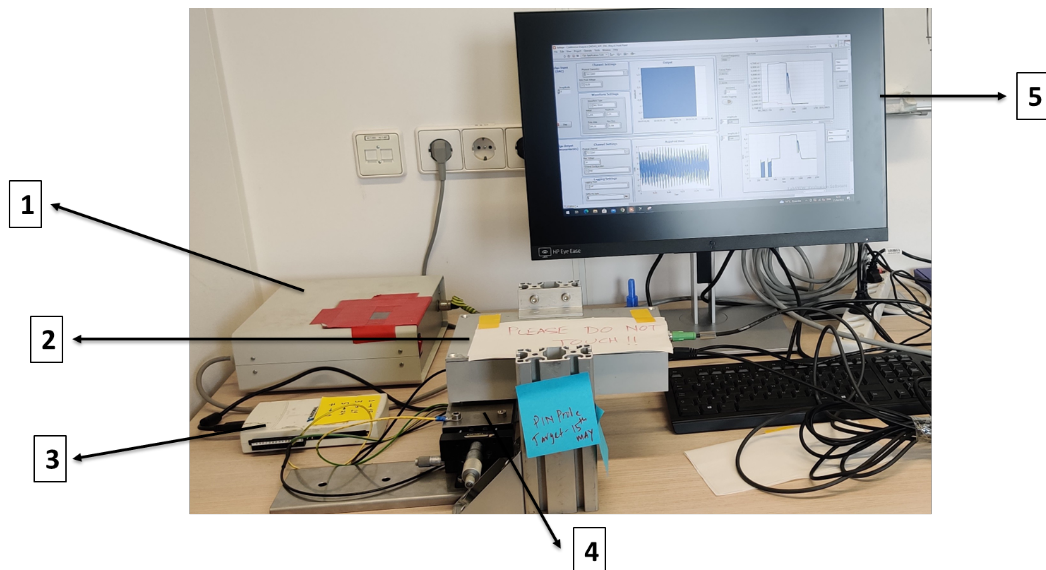

Figure 5.5: The experimental setup designed for the offline testing of Method A

After introduction of the glass plate on top of the receiving element, an experimental setup was designed to test the proposed theory offline, as depicted in figure 5.5. A dual power supply of +15V & -15V (1) is supplied to the non-contacting capacitive probe (2), placed upon a mounting stand. The glass plate placed inside the probe is supplied with an AC voltage (sine wave) from the NI DAQ (3). The probe is kept at a certain distance (in mm) above the metal plate, which is fixed to an adjustable *Z* table (4). With the help of this setup, it was possible to move the metal plate closer and farther to and from the device. The results of this variation of distance between the metal plate and the probe were visualized by a LabVIEW program, in the PC (5). It was ensured that, the metal plate and the housing of the probe were connected to a mutual ground, in one of the ground pins of the DAQ, to cancel out the effects of parasitic impedances and noise to the results.

5.3.2. Results and discussions

This section discusses the results obtained from the experiment conducted for observing the effect of C_p on the gain of the probe circuit, that affects the measured voltage output from it. For this purpose, it was decided to perform a frequency sweep, of the supplied AC voltage, from low (100 Hz) to high frequency (10 kHz) for each distance between the metal plate and the receiving element. Figure 5.6 presents the results for the relation between frequency and the gain of the probe circuit, with varying distances.

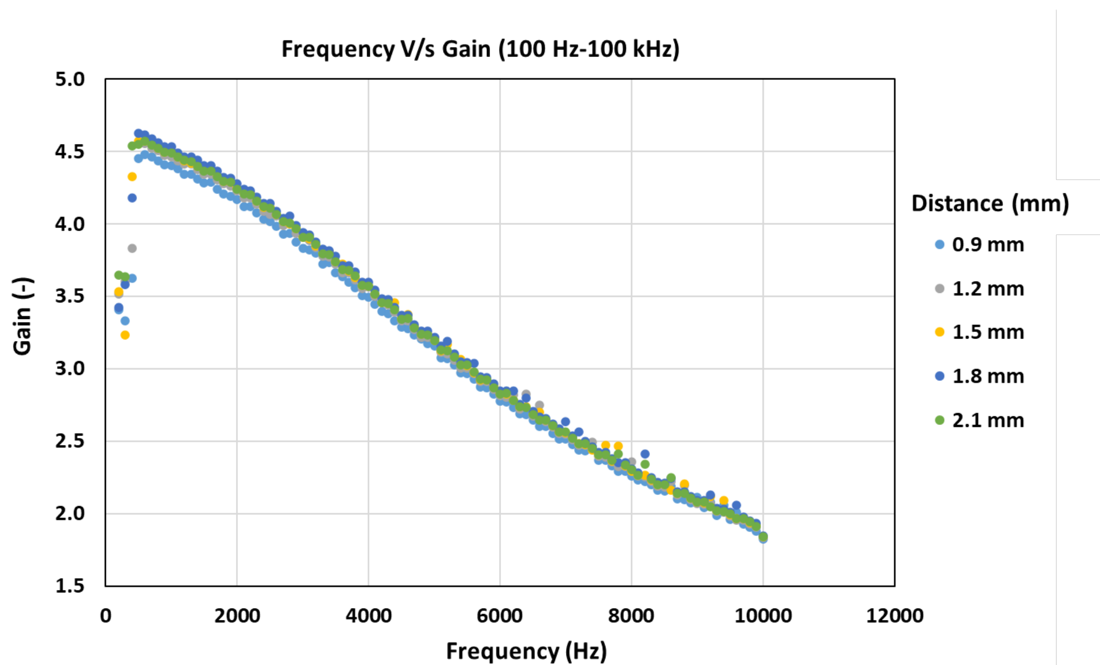

Figure 5.6: The behaviour of gain of the system as a function of frequency, for five distance variations of the metal plate from the probe area

From the graph in figure 5.6, it can be observed that the ratio of measured output voltage to the supplied voltage of 1V, decreases almost linearly with the increase in frequency. This can be evident from the the three-fold decrease in gain with three decades increase in frequency, implying the influence of a capacitor on the circuit. However, it can also be observed that the change in gain with distance is negligible. This behaviour of the circuit, at first was unexpected because, capacitance is inversely proportional to the distance between two conducting parallel plates, according to the expression,

$$C = \frac{\varepsilon_0 A}{d} \tag{5.3}$$

where ε_0 is the permittivity of free space, *A* is the smallest of area among the two plates, and *d* is the distance between them. Therefore, it was foreseen that with increase in distance between the metal plate

and the probe, the gain ratio would show a response, according to the figure 5.4b. This observation led to an inferential assumption that the capacitance, C_p, is not affecting the gain of the probe circuit. Figure 5.7 illustrates the culmination of figure 5.1 and 5.4b, by which this assumption was proved.

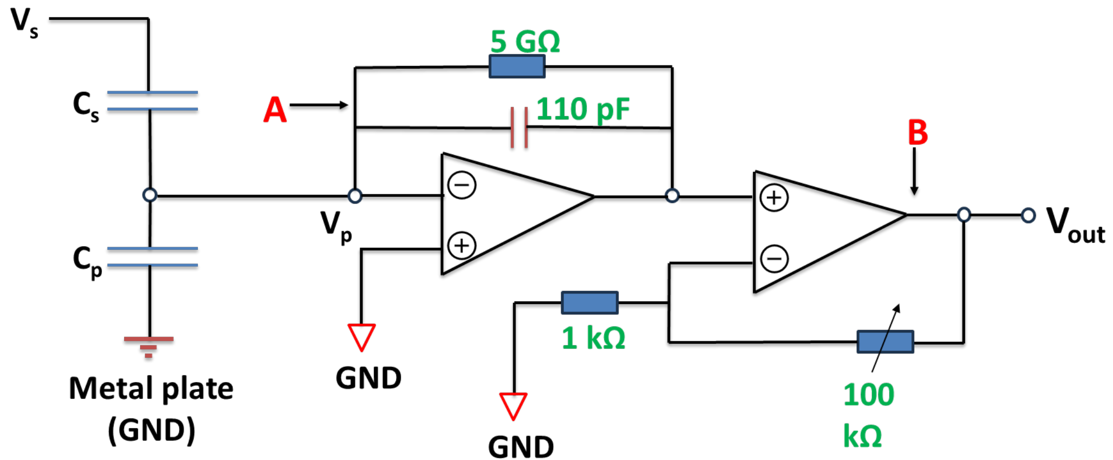

Figure 5.7: The probe circuit after the inclusion of two capacitances forming a voltage divider circuit

According to the circuit diagram schematic in figure 5.7, the potential at the point V_p is zero. This is because according to the theory of operational amplifiers (for an ideal amplifier), the potential at the non-inverting terminal should be equal to the potential at the inverting terminal, also known as the virtual short assumption [42]. In this case, as the non-inverting terminal is grounded, the potential at the inverting terminal is zero. Therefore, there is virtually no current flowing towards the C_p side, as there exists no potential difference between the metal plate and the point V_p. If there is no current through this branch, irrespective of the high feedback impedance of circuit A, there will no output voltage contribution from the capacitance, C_p. Thus, the behaviour of the gain ratio against the frequency, as depicted in figure 5.6, is actually the output voltage of the system with respect to the capacitance, C_s. This is due to the applied voltage from that side causing a potential difference with respect to point V_p (of $-V_s$ V). This proves the initial hypothesis of the capacitance, between metal plate and probe area, not affecting the gain of the system.

Therefore, this method of estimating the capacitance between the material under consideration and the receiving element was discarded. However, the failure of this method paved the way for devising another method, which is described in the next section.

5.4. Method B: n-layer voltage application method

The name of this method is symbolic to the fact that, a virtual n-layer representative of the solar cell stack is utilised to calibrate the probe. This idea arose as a result of the failure of the top capacitor method to estimate the capacitance. The background and motivation behind this method was the influence of only the top capacitor, C_s, on the gain of the probe circuit. The idea therefore, was to apply a voltage on the metal plate beneath the probe, such that the capacitance between them would affect the gain. So, in essence, this method was an exact opposite of method A in terms of having a capacitor at the bottom instead of at the top. The experimental approach followed to design and test the theory is described in the following sub-section.

5.4.1. Experimental methodology

The experimental setup used to test this theory remained the same. There were some adaptations and changes made to it, which are described as follows:

1. The top capacitor, due to the thickness of the glass plate, was removed from the inside of the probe. This was done so as to remove the effect of unnecessary capacitance, which could influence the behaviour of the circuit and/or add noise to the sent & received voltage signal.
2. On the metal plate that was placed beneath the probe, another metal plate was placed on top of it with paper filled in between their gap. The purpose of this adaptation was to replicate a cell stack, where the placed metal plate acted as a n-layer, the paper (dielectric) as an i-layer, and the bottom metal plate as a p-layer. As in the actual scenario, the p-layer is on top of Al/FTO that acts as a virtual ground, this metal plate was grounded. Figure 5.8 depicts the cross sectional view of the made adaptation along with its electrical replacement scheme.

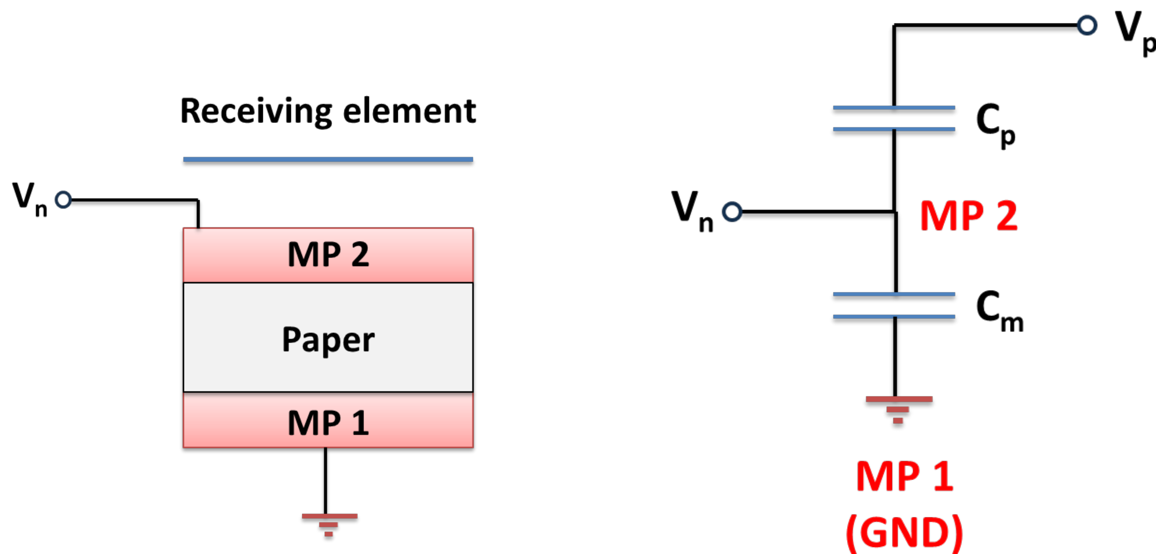

(a) A cross sectional view of the situation when a second metal plate (MP 2) was introduced over the existing metal plate (MP 1) with a dielectric (paper) between them

(b) An electrical replacement scheme of the situation

Figure 5.8: The scenario after the glass plate was introduced inside the probe

From figures 5.8a and 5.8b, it can be observed that the situation formed as a result of this idea was analogous to method A. The only main difference was that the capacitance that formed at the top of the receiving element (C_s) had been replaced by a capacitor (C_m) at the bottom of the added metal plate (MP 2). Apart from this, a voltage (V_n) was now applied at the metal plate directly under the probe, while the existing metal plate (MP 1) was grounded. With this setup, it was now possible to develop a potential difference between the applied voltage and the input point of the operational amplifier (V_p).

The next step was to ensure that the formed capacitance between the two metal plates, C_m, does not influence C_p. For this purpose, it was sufficient to prove that the voltage drop majorly occurs across the capacitor C_p. This was proved by a voltage divider circuit analysis with the two capacitors being in series connection. The capacitance, C_m, can be calculated by the equation,

$$C_m = \frac{\varepsilon_0 \varepsilon_r A}{d} \tag{5.4}$$

where ε_r is the relative permittivity of the dielectric medium. Here, as paper is the dielectric between the two parallel metal plates, the relative permittivity is taken to be **3** [43]. The area of the smaller metal plate was measured to be 150 cm^2 and the distance between them (equal to

the dielectric thickness) was approximately 0.5 mm. Substituting these values in equation 5.4, we obtain C_m as **796.86 pF**. Similarly, C_p was calculated from the equation 5.3, where area of the smaller plate was measured to be 225 mm^2 and the distance (between MP 2 and the receiving element) was varied between 0.4 mm to 4 mm. Therefore, C_p ranged from **0.5 pF to 5 pF**. Now, for capacitors in series, the total capacitance (C_T) is given by,

$$C_T = \frac{C_m \cdot C_p}{C_m + C_p} \tag{5.5}$$

which results in a range of values from 0.499 pF to 4.97 pF. Therefore, the ratio of division of voltage drop across the two capacitors become,

$$V_{C_m} = \frac{C_T}{C_m} V_n \tag{5.6}$$

$$V_{C_p} = \frac{C_T}{C_p} V_n \tag{5.7}$$

where, V_n is the applied AC voltage. From these equations, it can be observed that the voltage drop is negligible across the capacitance C_m (0.06 to 0.6 %). Thus, it will not have any significant influence on the voltage application across C_p.

After validating the adaptations made to the setup, the calibration test was performed in a similar approach as done for method A, using the same software program. The results of which are discussed subsequently in the next sub-section.

5.4.2. Results and discussions

The results from the calibration test through method B are presented and discussed in this section. Similar to the test performed in method A, a frequency sweep was done from lower (110 Hz) to higher frequency (110 kHz). The results of this test is illustrated in figure 5.9.

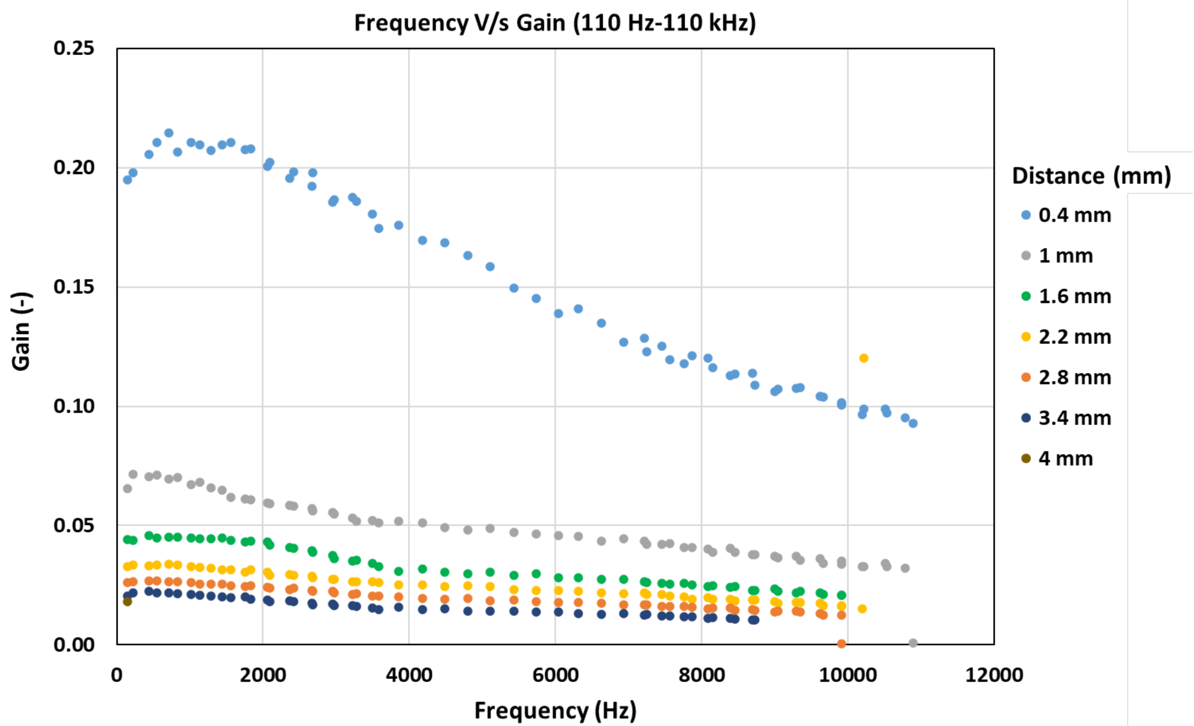

Figure 5.9: The behaviour of gain of the system as a function of frequency, for distance variations between 0.4 and 4 mm

From the graph in figure 5.9, it can be observed that with this method the capacitance, C_p, indeed affects the gain of the probe circuit. When the distance was varied from 0.4 mm to 4 mm, the ratio of the measured output voltage to the supplied voltage decreased with increase in distance between the metal plate and the probe area. This behaviour can be explained from the theory of capacitors and capacitances. We know that,

$$Q = CV \tag{5.8}$$

where, Q is the charge of the capacitor and V is the voltage applied. Together from this relation and equation 5.3, it can be inferred that as the distance of separation between the conducting surfaces decreases, the capacitance and the charge stored in the capacitor increases. When this capacitor is connected to an external circuit, the charge stored across the capacitor flows into that circuit. Therefore, the smaller the distance of separation, the larger the charge stored and hence the larger the charge flow into the external circuit. This increase in the charge flow into the external circuit, here the probe circuit, increases the measured voltage at the output. It can also be observed here that, the gain of the circuit reaches approximately zero when the distance between the metal plate and the probe area approaches 4 mm. Besides this, the decrease in gain begins to saturate after about 2 mm separation distance. From these two observations, it can be inferred that the sensitivity (of gain) of the circuit reduces as the distance is increased. This variation of gain with distance was quantified, by obtaining the mean of the gains over the entire frequency sweep for all distances. Figure 5.10 depicts the relation obtained between the gain with varying distances from 0.4 to 4 mm, in intervals of 0.3 mm.

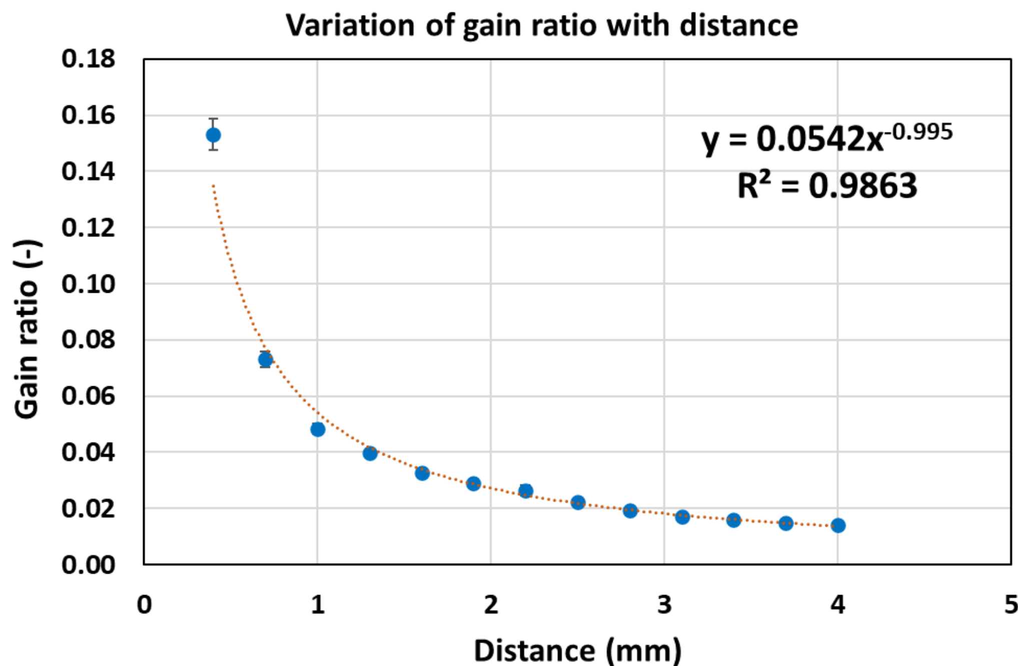

Figure 5.10: The relationship between the gain of the circuit and distance between the metal plate & receiving element of the probe

It can be observed from figure 5.10 that the gain of the circuit follows an inverse (power) relation with the distance of separation. The decrease in gain is stronger at lower distances as compared to the reduction at higher distances. The gain reduces approximately by 50% for the first 0.3 mm increase in distance, which reduces to about 33% for the next 0.3 mm increment in distance. This decrease percentage reduces to around 5% for an increment of distance from 3.7 mm to 4 mm.

The next objective was to validate and observe how well the frequency response of the system, obtained experimentally, correlates with the theoretical behaviour. For this purpose, the first step was to calculate the theoretical transfer function (gain) of the probe circuit after introduction of capacitance C_p. Figure 5.11 depicts the circuit of the probe when the capacitance between the metal plate and the

probe was introduced.

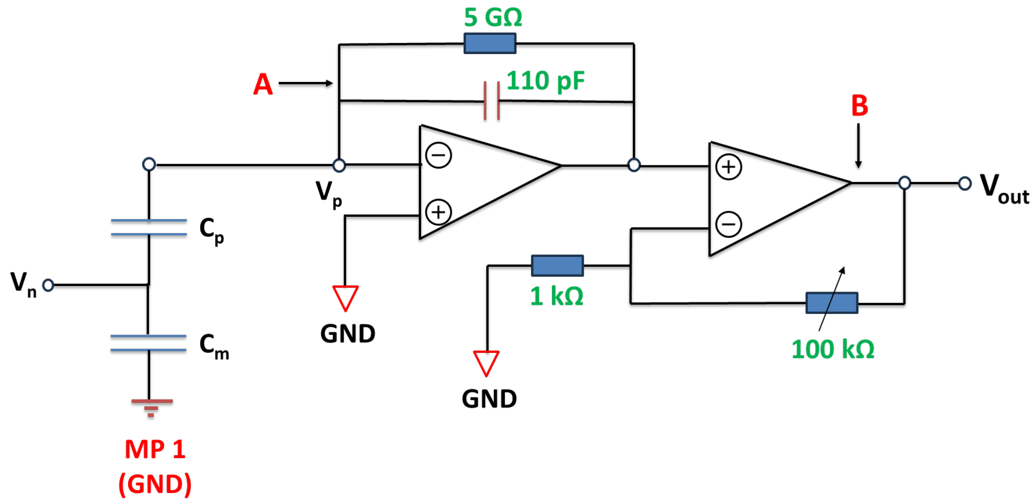

Figure 5.11: The probe circuit formed in the testing of method B

The transfer function of a circuit is defined as the ratio of the output voltage to the input voltage of the system. It is dependent on the passive elements of a circuit (resistors, capacitors) and the active components (operational amplifiers). The (theoretical) transfer function of the entire circuit can be expressed as the product of transfer function of circuit A and B, as they are in series with each other. Focusing first on the transfer function of circuit A ($H(s)_A$), we have,

$$H(s)_A = \frac{I.Z_f}{I.Z_i} \tag{5.9}$$

where, *I* is the current flowing from the applied voltage, V_n, to the circuit A, Z_f and Z_i are the feedback and input impedance respectively. The input impedance to circuit A is due to the capacitance C_p, and can be expressed as,

$$Z_i = \frac{1}{sC_p} \tag{5.10}$$

and the feedback impedance (considering the parallel RC circuit over the operational amplifier) can be written as,

$$Z_f = \frac{5 \times 10^9}{1 + 0.55s} \tag{5.11}$$

where *s* is the complex function of angular frequency (ω) and/or frequency (f), given by,

$$s = i\omega = i2\pi f \tag{5.12}$$

Now, substituting the impedances from equations 5.10 and 5.11 in the equation 5.9, we get,

$$H(s)_A = \frac{5 \times 10^9 sC_p}{1 + 0.55s} \tag{5.13}$$

Now the second transfer function, $H(s)_B$, should ideally be equal to the pure resistive gain as deduced in equation 5.2. Due to the experiment being performed also at higher frequencies, the operational amplifier's behaviour changes. For an ideal case, it can be assumed that there are no frequency dependent elements in an operational amplifier (op-amp), that is, the op-amp has an infinite bandwidth. This assumption is only valid for low-gain, low frequency systems. However, the bandwidth of real op-amps is certainly not infinite; in fact, most op-amps have a frequency response similar to that of a low-pass filter (a circuit that allows only lower frequencies to pass through) with a low cutoff frequency. Cutoff frequency is defined as the frequency at which the gain of the op-amp starts to reduce linearly

with increasing frequency. This behaviour occurs due to the internal compensation (of frequency) of the operational amplifiers, to protect them from unnecessary oscillations [44]. Therefore, the transfer function of a real operational amplifier, can be written in terms of its closed loop Gain Bandwith product (GBW) and closed loop gain (A_{CL}). The GBW can be expressed as,

$$GBW = Gain \times Bandwidth \tag{5.14}$$

The transfer function of circuit B ($H(s)_B$) is thus given by,

$$H(s)_B = \frac{A_{VO}}{s + \frac{2\pi(GBW)}{A_{CL}}} \tag{5.15}$$

where, A_{VO} is the large signal voltage gain of OP07. From the datasheet of the operational amplifier [45], the closed loop bandwidth is taken to be 0.6 MHz and the large signal voltage gain is 150 V/mV. Substituting these values in equation 5.15, we have,

$$H(s)_B = \frac{1.5 \times 10^5}{s + 37325.85} \tag{5.16}$$

The total transfer function, now, can be expressed as the product of $H(s)_A$ and $H(s)_B$,

$$H(s)_{tot} = \frac{7.5 \times 10^{14} sC_p}{(1 + 0.55s)(s + 37325.85)} \tag{5.17}$$

The total transfer as obtained in equation 5.17, was then modelled in MATLAB to generate a Bode plot. A Bode plot is important in understanding the frequency response of a closed loop system [46]. The plot consists of magnitude (in decibels (dB)) and frequency (in Hz) on the y and x axes respectively. Figure 5.12 presents the Bode plot of the modelled theoretical transfer function and the experimental data obtained.

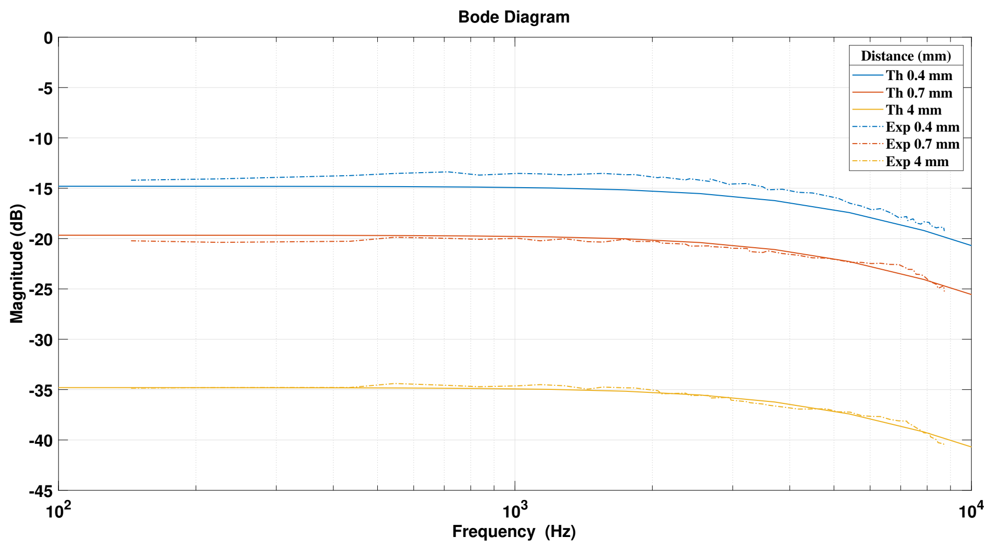

Figure 5.12: The Bode diagram showing the correlation between the theoretical (solid line) and experimental frequency response (dash-dot line) of the system

The bode diagram in figure 5.12, was obtained for a set of three distances (0.4 mm, 0.7 mm and 1 mm) among all the varied distances between the metal plate and the probe area. Three distances correspond to three different values of C_p, which act as the input to the theoretical transfer function modelled. The plot was restricted within the limits of 100 Hz to 10 kHz as the experiment was performed in this region. It can be observed from the graph that the experimental behaviour of the system complies well with its expected theoretical response, in terms of:

- **Frequency response:** The response of the probe circuit, both experimentally and theoretically, as a function of frequency is the same. The magnitude (gain) remains constant until about 4.5 kHz, after which it starts to decrease logarithmically. This nature of response proves the low-pass behaviour of the circuit at high frequencies, that permits the system to have a consistent gain until one frequency. To further investigate the actual response of the circuit, a Bode plot from very low frequencies ($<$ 1 Hz) to very high frequencies ($>$ 100 kHz) was also done.

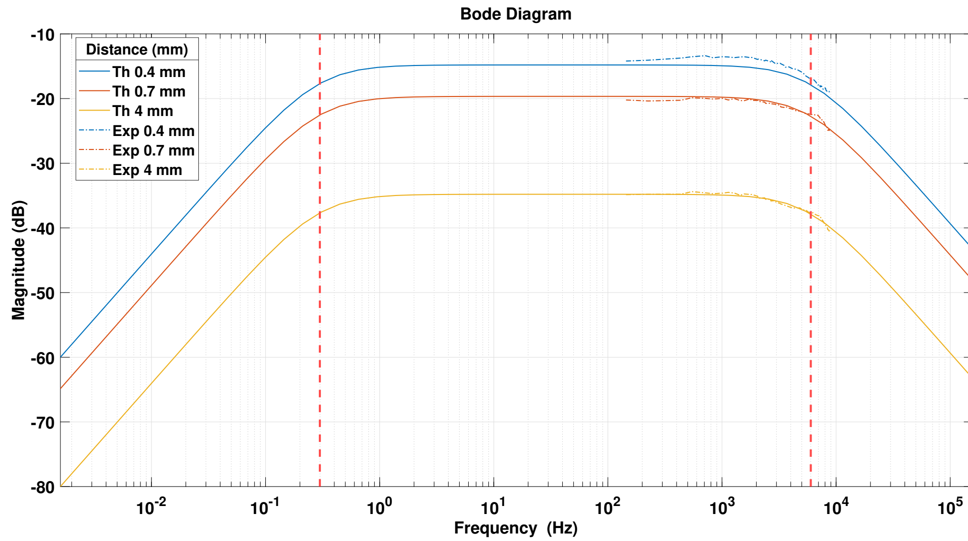

Figure 5.13: The Bode diagram of the probe circuit from low frequency to high frequency region, with two vertical dashed lines (in red) depicting the low and high cut-off frequencies of the system

Figure 5.13 presents the Bode diagram for a broader range of frequency. It can be observed from the plot that the response of probe circuit corresponds to that of a band-pass filter. A band-pass filter is defined as a type of filter that allows to pass a certain range of frequency, unattenuated. This range of frequency is known as pass bandwidth of the filter, indicated by the dashed lines in red in the plot. The lower and upper limits of the frequencies are obtained by searching for the point where the magnitude drops by 3 dB of its constant value. The presence of two cutoff frequencies, one at lower frequency and other at higher frequency, makes it a combination of low and high pass filters [47]. From the Bode diagram, the lower cutoff frequency (f_L) is approximately 0.3 Hz, while the higher cutoff frequency (f_H) is around 6000 Hz. Therefore, the pass band (f_B) of this circuit can be expressed as,

$$f_B = f_H - f_L \tag{5.18}$$

This implies that the bandwidth of the probe circuit at which it provides a constant linear gain is 5999.7 Hz. The frequencies below 0.3 Hz and above 6000 Hz will not pass through the circuit. The peak gain of a band pass filter occurs at its resonant frequency (f_R), which can be expressed as [47],

$$f_R = \sqrt{f_L f_H} \tag{5.19}$$

which results in resonant frequency of 42.43 Hz. This implies that an AC voltage applied at this frequency would result in maximum possible gain of the circuit.

- **Magnitude response:** From the Bode plot in figure 5.12, it can be observed that the gain provided by the circuit, at three distances, is consistent as expected from the theory. A small exception is the experimental gain of the circuit due to a distance of 0.4 mm, which is overestimated by around 7% from the theoretical gain.

In conclusion, the method B proves that the gain of the circuit is indeed dependent on the capacitance between the receiving element of the probe and the material under evaluation (here, a metal plate). With this method, it was also possible to analyze the response of the complete circuit at different frequencies. This helped in understanding the range of frequency in which a voltage can be applied to estimate the capacitance C_p. Therefore, with the culmination of both these findings, it is now possible to calibrate the device by finding the capacitance between the probe and the material under evaluation. The device can therefore be installed now in the PECVD machine at HyET to measure the opto-electrical properties (short-circuit current density, open-circuit voltage (subsequently the fill factor) and decay time of charge carriers) of the silicon layers, accurately, by incorporating this measured capacitance as a correction factor.

6 Conclusions and Recommendations

This final chapter presents the conclusive answers to the proposed research questions in the first section. In section 2, some recommendations are suggested on the directions and scope for future work in this field of study.

6.1. Conclusion

The primary goal of the project was to highlight and prove the necessity of having in-line diagnostics in production industry. The road to proving this involved modelling the procedure and implementing it in and on the production machines. The scope of this thesis was limited to two production processes, first, the APCVD process (for FTO) and second, the PECVD process (for Si layers) at HyET. For this purpose, three research questions were formulated. The first two dealt with assessing the front TCO layer properties, while the final question involved calibrating the tool for characterizing the deposited Si layers. This section discusses the answers to these research questions in the order they appear in the chapters as follows:

1. ***Using the reflection spectrum of the deposited FTO, how can the information regarding the layer thickness and its electrical properties be extracted?***

   The spectrum of light reflecting off of the front TCO (FTO) layer contains vital information in it. This vital information can be found in two halves of the electromagnetic spectrum, one in the ultra-violet region and the other in the near-infrared part. While the former is utilised to obtain the thickness (optical) of the layer deposited, the latter part contains information about electrical parameters. Electrical parameters include the concentration of free charge carriers (electrons) per unit volume of the layer and their mobility inside the bulk of the layer. The thickness, from the UV-VIS part of the reflection spectrum, can be obtained by the "Optical Thickness (OT)" method. The theory of this method is based on utilising the slope and order (maxima and minima) of the interference fringes, as observed in the spectrum (refer figures 3.5a and 3.5b). This is possible due to the relation between the refractive index and the thickness of the layer [15], as explained by equations 3.40 and 3.41. Besides this, a series of statistical data filtration steps are employed (refer section 3.2.3) to obtain a final value of thickness (in nm) of the deposited FTO layer.

   On the other hand, the electrical parameters can be obtained from the "Drude Model Fitting" method. The underlying theory of this method is the relation between Drude model [26] parameters (plasma and damping energy) and electrical properties (N and μ) [25], as given by the equations 3.18 and 3.19. The aforementioned method is the second model that was proposed among two proposals. This model was selected over the first, owing to its accuracy in prediction of the said parameters, ease of integration into software and reduced complexity. One of the key learnings from the rejection of the empirical method, was the redundancy of Tauc-Lorentz parameters in determining the electrical properties from the NIR part of the spectrum. This is symbolic to the name of this method, as it only takes into consideration the Drude model parameters. This method has a reduced number of statistical steps, as it involves finding the minimum in reflection

(Black Wavelength) and then implementing a least square fit method in a certain range, to obtain the values of N and μ.

The two models were then incorporated into the LabVIEW software and the measurement setup (see figures 3.22 and 3.23) was prepared for recording the data from the deposited material. In this setup, light of appropriate wavelength(s) was guided perpendicularly on to the surface of the FTO layer from the UV-VIS and NIR spectrometers. The reflectance spectrum obtained, as a result, was stored in the software and with some post-processing steps, relevant information (thickness, N & μ) regarding the layer were generated. The designed setup was capable of recording measurements across the width of the foil as well, to check for the homogeneity of the deposited material. The thickness values thus obtained for the different experiments, were compared against the conventional cross-SEM thickness values. The values obtained from the optical method were in most cases higher than the SEM values, owing to the difference in measurement techniques and the assumptions considered in the former method (refer figure 3.28). As far as electrical properties are concerned, the values of optically obtained charge carrier densities (refer figure 3.31) showed a much better correlation than the mobilities (refer figure 3.32), measured from Hall effect setup. This is because the method developed at HyET considers only the bulk of the layer, at the top surface of the FTO, rather than grain boundaries inside the layer, that limit the mobility of electrons. The (optical) sheet resistances also were, in most cases, higher than the values obtained from Hall effect measurements (refer figure 3.33).

2. ***How to enhance the robustness of the current offline sheet resistance tool?***

   Along with obtaining the optical sheet resistance of the deposited FTO layer, an electrical determination of this parameter gives a clearer understanding of the layer. Therefore, a tool was developed at HyET, which exploited the natural formation of a highly resistive oxide layer (Al_2O_3) between the substrate and the deposited TCO (refer figure 4.1), to calculate the sheet resistance electrically. This designed tool was an on-line (on the machine) non-destructive electrical sheet resistance measuring device (see figure 2.4). The measurement principle was based on Ohm's law, where a potential difference was induced via an applied current to measure the resistance of the layer. The induced potential drop was measured between 17 pins with the middlemost pin acting as the ground pin, in the first version of the measurement setup. In this version of the setup, the current was supplied from an external current source and the measured potentials were recorded by a data acquisition card (DAQ), in a Non-referenced Single Ended mode. The resulting potentials were then fitted to a modified Bessel function of the second kind (equation 4.1) in the software program.

   However, the device could not generate reliable data for recently produced materials due to the malfunctioning of the current source. Therefore, it became necessary to modify the existing setup such that it becomes robust and easy to troubleshoot in the future, if and when required. For this purpose, it was decided to remove the external current source meter and instead supply the current from the DAQ's voltage supply. This decision led to the implementation of a current limiting resistance board (to keep the current flow from the DAQ low) and a differential mode of configuration between WONDER and DAQ. As a result, the number of pins were reduced because of the formation of paired voltage measurement channels. The principle of measurement remained the same, with only one difference, which was that the returning current passed directly to the ground (of the NI DAQ) (see figure 4.7). Additionally, a calibration sample was also designed to check the health of the formed channels (refer figure 4.8). Thus, the second version of the measurement setup was made compact, easy to troubleshoot and more robust. The device was retrieved to generate values for electrical sheet resistances of the FTO layer. The obtained results were compared against the optically obtained sheet resistances and the values resulting from the Hall effect measurement. From the graphs, it was inferred that the electrical sheet resistances showed better correlation with Hall effect data as opposed to the optical results. The errors in consecutive measurements were within $\pm$ 2 Ω/sq.

3. ***How to calibrate the PECVD diagnostic tool such as to obtain reliable data from the device?***

   As an in-line diagnostic to characterize the deposited silicon layers, a device was fabricated at HyET. This device has the capability to estimate the opto-electrical parameters of a solar cell stack, capacitively, without making any physical contact with the material. Before placing the device in the machine, it was necessary to ensure that it generates reliable data. For this purpose, calibration of the fabricated device was required. The primary objective was to obtain the capacitance between the PV material and the probe's sensor area, which could be used as a correction factor for the obtained parameter. To achieve this, two methods were experimented.

   The first experiment was using a conductive glass plate as a top capacitor. The idea of this method was to utilise the formed voltage divider circuit (refer figure 5.7), to estimate the capacitance in between the probe area and material under evaluation (metal plate). But via this method, no effect of this capacitance (C_p) was observed on the circuit's output, due to the absence of a current flow from C_p side. As a result of this failure, a second method was devised that was, in essence, the reversal of the first method. In this method, a voltage was applied on a virtual n-layer, which affected the output of the circuit. This method was helpful in understanding the dependency of the distance (capacitance) between the concerned material and the probe surface (refer figure 5.10). The response of the probe circuit, experimentally, as a function of frequency resembled the theoretically expected response (see figures 5.12 and 5.13). These findings prove that calibration of the device is possible via this method.

6.2. Recommendations for future work

Overall, the research objectives formulated for the scope of this thesis project have been achieved. However, there are possibilities through which the research study can be optimised, improved or, in regards to the last research question, applied in-line. For this purpose, some recommendations in the direction of future study/application are provided in this section.

Firstly, the ”Optical Thickness” model can be further optimized by considering the surface roughness of the front TCO layer. This could increase the correlation of thickness values with the SEM measurements. On the ”Drude Model Fitting”, the charge carrier density and the mobility values are currently obtained by taking the effective mass of electron to be 28% of the mass of electron. This parameter can be further investigated, so as to obtain more accurate values. Furthermore, the two models are now validated only for the one kind of TCO (FTO deposited at HyET), which can be extended (validated) to various different types of TCO, like Aluminum doped Zinc Oxide (AZO) or Indium doped Tin Oxide (ITO).

Secondly, the electrical sheet resistance measurement tool currently operates in a manual mode, where the operators place the tool on the FTO layer to take measurements. This might introduce personal and/or measurement errors, as taking a successful measurement needs proper training. Therefore, this procedure has the possibility of being automated where the tool can be mounted on a linear guide and be traversed across the roller. After it reaches the desired position a switch can be enabled, that presses the pins gently against the layer.

Finally, to implement the calibration method in-line at the PECVD machine, it is recommended to perform the procedure each time before a deposition run. This can be done by preparing a sample such that it mimics the n-layer. It can be prepared by sputtering aluminum on a plastic foil, ensuring that they are both of the equivalent thickness as the substrate. Then a stimulus voltage can be applied to the sample while it is placed inside the machine (at the same place where the substrate roll is going to be located), under the probe.

Bibliography

[1] H. Ritchie, M. Roser, and P. Rosado, "Energy," *Our World in Data*, 2022. [Online]. Available: https://ourworldindata.org/energy.

[2] M. B. Hayat, D. Ali, K. C. Monyake, L. Alagha, and N. Ahmed, *International Journal of Energy Research*, vol. 43, pp. 1049–1067, 3 2019, ISSN: 1099114X. DOI: 10.1002/er.4252.

[3] V. Benda and L. Černá, "Pv cells and modules – state of the art, limits and trends," *Heliyon*, vol. 6, no. 12, e05666, 2020, ISSN: 2405-8440. DOI: https://doi.org/10.1016/j.heliyon.2020.e05666. [Online]. Available: https://www.sciencedirect.com/science/article/pii/S2405844020325093.

[4] Reglobal. "Technology roadmap: Anticipated trends in the c-si pv industry." (2022), [Online]. Available: https://reglobal.co/technology-roadmap-anticipated-trends-in-the-c-si-pv-industry/.

[5] HyET. (2018), [Online]. Available: https://www.hyetsolar.com/technology/Thin-Film-Solar/.

[6] K. Jäger, H.-Z. Berlin, E. Hamers, J. Lenssen, and P. Veltman, "Large-area production of highly efficient flexible light-weight thin-film silicon pv modules," 2014. DOI: 10.4229/28thEUPVSEC2013-3BO.5.5. [Online]. Available: https://www.researchgate.net/publication/262724897.

[7] T. Ellison, "Non-contacting capacitive diagnostic device," US006917209B2, Jul. 12, 2005.

[8] T. Ellison, D. Dodge, J. Karn, *et al.*, "Inline diagnostic systems for the characterization of multijunction solar cells," *IEEE*, 2006.

[9] M. Izu and T. Ellison, "Roll-to-roll manufacturing of amorphous silicon alloy solar cells with in situ cell performance diagnostics," *Solar Energy Materials and Solar Cells*, vol. 78, pp. 613–626, 1-4 2003, ISSN: 09270248. DOI: 10.1016/S0927-0248(02)00454-3.

[10] A. H. R. Al-Sarraf, Z. T. Khodair, M. I. Manssor, R. A. A. K. Abbas, and A. H. Shaban, "Preparation and characterization of zno nanotripods and nanoflowers by atmospheric pressure chemical vapor deposition (apcvd) technique," *AIP Conference Proceedings*, vol. 1968, 2018, ISSN: 15517616. DOI: 10.1063/1.5039192.

[11] Avantes. (2022), [Online]. Available: https://www.avantes.com/products/spectrometers/.

[12] L. R. P. Butler and K. Laqua, "Nomenclature, symbols, units and their usage in spectrochemical analysis-ix. instrumentation for the spectral dispersion and isolation of optical radiation (iupac recommendations 1995)," *Pure and Applied Chemistry*, vol. 67, no. 10, pp. 1725–1744, 1995. DOI: doi:10.1351/pac199567101725. [Online]. Available: https://doi.org/10.1351/pac199567101725.

[13] N. C. Xuan, "What is a spectrometer? uv, vis and ir spectrometer explained," 2023. [Online]. Available: https://wavelength-oe.com/blog/what-is-a-spectrometer/.

[14] P. Babal, "Doped nanocrystalline silicon oxide for use as (intermediate) reflecting layers in thin-film silicon solar cells," Ph.D. dissertation, Delft University of Technology, 2014.

[15] A. Smets, K. Jäger, O. Isabella, R. van Swaaij, and M. Zeman, *Solar Energy: The Physics and Engineering of Photovoltaic Conversion, Technologies and Systems*. UIT Cambridge, 2016, ISBN: 9781906860325. [Online]. Available: https://books.google.nl/books?id=vTkdjgEACAAJ.

[16] T. Ellison, "Non-contacting pv capacitive diagnostic (pvcd) system for real-time in-situ analysis, qa/qc, and optimization," *Conference Record of the IEEE Photovoltaic Specialists Conference*, vol. 2000-January, pp. 732–735, 2000, ISSN: 01608371. DOI: 10.1109/PVSC.2000.915978.

[17] R. Fisher, S. Perkins, A. Walker, and E. Wolfart. “Spatial smoothing filters–gaussian smoothing.” (2003), [Online]. Available: https://homepages.inf.ed.ac.uk/rbf/HIPR2/gsmooth.htm.

[18] WolframAlpha. “Full width at half maximum.” (2022), [Online]. Available: https://mathworld.wolfram.com/FullWidthatHalfMaximum.html.

[19] D. Locci-Lopez, R. Zhang, A. Oyem, and J. Castagna, “The multi-scale fourier transform,” Sep. 2018. DOI: 10.1190/segam2018-2994723.1.

[20] R. van de Boomgaard. “Gaussian smoothing and gaussian derivatives.” (2017), [Online]. Available: https://staff.fnwi.uva.nl/r.vandenboomgaard/IPCV20172018/LectureNotes/IP/LocalStructure/GaussianDerivatives.html.

[21] P. Sahoo, “Surface topography,” J. P. Davim, Ed., pp. 1–32, 2011. DOI: https://doi.org/10.1533/9780857091444.1. [Online]. Available: https://www.sciencedirect.com/science/article/pii/B9780857091147500013.

[22] LabVIEW. “Autocorrelation function.” (2023), [Online]. Available: https://www.ni.com/docs/en-US/bundle/labview/page/lvanls/autocorrelation.html.

[23] J. Frost. “How to interpret r-squared in regression analysis.” (2023), [Online]. Available: https://statisticsbyjim.com/regression/interpret-r-squared-regression/.

[24] E. Hamers, “Hyet internal literature,” no. M05019, 2005.

[25] M. A. Lieberman and A. J. Lichtenberg, “Principles of plasma discharges and materials processing,” 1994.

[26] P. Drude, “Zur elektronentheorie der metalle,” *Annalen der Physik*, vol. 306, no. 3, pp. 566–613, 1900. DOI: https://doi.org/10.1002/andp.19003060312. [Online]. Available: https://onlinelibrary.wiley.com/doi/abs/10.1002/andp.19003060312.

[27] C. Kittel, “Introduction to solid state physics 6th edition,” 1986.

[28] M. van den Donker, “Dust formation in silane plasmas, and its effect on layer deposition,” Ph.D. dissertation, Eindhoven University of Technology, 2003.

[29] Horiba, “Tauc-lorentz dispersion formula,” 2006. [Online]. Available: https://www.horiba.com/fileadmin/uploads/Scientific/Downloads/OpticalSchool_CN/TN/ellipsometer/Tauc-Lorentz_Dispersion_Formula.pdf.

[30] A. D. Rakić, A. B. Djurišić, J. M. Elazar, and M. L. Majewski, “Optical properties of metallic films for vertical-cavity optoelectronic devices,” *Appl. Opt.*, vol. 37, no. 22, pp. 5271–5283, 1998. DOI: 10.1364/AO.37.005271. [Online]. Available: https://opg.optica.org/ao/abstract.cfm?URI=ao-37-22-5271.

[31] L. van der Pauw, “A method of measuring specific resistivity and hall effect of discs of arbitrary shape,” *Philips Res. Rep*, vol. 13, no. 1, pp. 1–9, 1958.

[32] S. Venkataraman, “Investigation of opto-electrical and structural properties of atmospheric pressure chemical vapor deposition of fluorine-doped tin oxide,” Delft University of Technology, Master’s Thesis, 2023.

[33] N. Noor, C. K. T. Chew, D. S. Bhachu, M. R. Waugh, C. J. Carmalt, and I. P. Parkin, “Influencing fto thin film growth with thin seeding layers: A route to microstructural modification,” *J. Mater. Chem. C*, vol. 3, pp. 9359–9368, 36 2015. DOI: 10.1039/C5TC02144H. [Online]. Available: http://dx.doi.org/10.1039/C5TC02144H.

[34] N. Mathew, D. Perez, W. Suk, B. P. Uberuaga, and E. Martinez, “Interstitial hydrogen enhances the mobility of some grain boundaries in tungsten,” *Nuclear Fusion*, vol. 62, no. 8, p. 086 016, 2022. DOI: 10.1088/1741-4326/ac70e9. [Online]. Available: https://dx.doi.org/10.1088/1741-4326/ac70e9.

[35] R. Quax, “Fast and smart diagnostics for the monitoring and improvement of the production of a-si:h modules on an industrial scale,” Delft University of Technology, Master’s Thesis, 2013.

[36] F. M. Smits, “Measurement of sheet resistivities with the four-point probe,” *The Bell System Technical Journal*, vol. 37, no. 3, pp. 711–718, 1958. DOI: 10.1002/j.1538-7305.1958.tb03883.x.

[37] E. W. Weisstein. "Modified bessel differential equation." (2023), [Online]. Available: https://mathworld.wolfram.com/ModifiedBesselDifferentialEquation.html.

[38] N. Instruments. "Ni usb-621x user manual." (2023), [Online]. Available: https://www.ni.com/docs/en-US/bundle/usb-621x-features/resource/371931f.pdf.

[39] S. P. Kikken, "Measuring film resistivity: Understanding and refining the four-point probe set-up," Eindhoven University of Technology, Bachelor's Thesis, 2018.

[40] J. Bishop. "Op-amp inverting and non-inverting circuits." (2022), [Online]. Available: https://www.circuitbread.com/tutorials/op-amp-inverting-and-non-inverting-circuits.

[41] S. Mishra, "Pin probe: Online calibration and measurement signal analysis," HyET Solar & Delft University of Technology, Master's internship report, 2022.

[42] T. Kuphaldt, *Lessons in electric circuits, volume iii–semiconductors*, 2009. [Online]. Available: http://hdl.handle.net/20.500.12091/425.

[43] S. Simula, S. Ikäläinen, K. Niskanen, T. Varpula, H. Seppä, and A. Paukku, "Measurement of the dielectric properties of paper," *Journal of Imaging Science and Technology*, vol. 43, pp. 472–477, 1999. DOI: 10.2352/ISSN.2169-4451.1998.14.1.art00039_1.

[44] K. H. Lundberg, "Internal and external op-amp compensation: A control-centric tutorial," in *Proceedings of the 2004 American Control Conference*, IEEE, vol. 6, 2004, pp. 5197–5211.

[45] *Op07x precision operational amplifiers*, SLOS099H, Texas Instruments, Mar. 2023.

[46] J. Hahn, T. Edison, and T. Edgar, "A note on stability analysis using bode plots," *Chemical Engineering Education*, vol. 2001, pp. 208–211, Jun. 2001.

[47] W. Menke and J. Menke, "9 - detecting correlations among data," in *Environmental Data Analysis with MatLab*, Boston: Elsevier, 2012, pp. 167–201, ISBN: 978-0-12-391886-4. DOI: https://doi.org/10.1016/B978-0-12-391886-4.00009-X. [Online]. Available: https://www.sciencedirect.com/science/article/pii/B978012391886400009X.